Czech Technical University in Prague
Faculty of Nuclear Sciences and Physical Engineering
Department of Physical Electronics

Vybrané aspekty numerických metod pro hydrodynamické simulace laserového plazmatu

Some aspects of numerical methods for laser plasma hydrodynamics

Diploma thesis

Author: **Bc. Jan Nikl**
Supervisor: **Ing. Milan Kuchařík, Ph.D.**
Consultant: **Dr. Stefan Andreas Weber, Ing. Milan Holec**
Academic year: **2016/2017**

Před svázáním místo této stránky **vložíte zadání práce** s podpisem děkana (v jedné kopii práce bude list s originálem podpisu).

Toto bude jediný oboustranný list ve Vaší práci!

Prohlášení

Prohlašuji, že jsem předloženou práci vypracoval samostatně a že jsem uvedl veškerou použitou literaturu.

V Praze dne 4. května 2017 Bc. Jan Nikl

Acknowledgements

I would like to express my deepest gratitude to my supervisor Ing. Milan Kuchařík, PhD. for kind and patient guidance, helpful suggestions, support and extensive textual corrections. My thanks also deserve to my consultant Ing. Milan Holec, PhD. for long factual discussions, introduction to the topic, providing me the simulation code and always friendly attitude. Furthermore, I would like to also thank at this place to my consultant Dr. Stefan Weber for cooperation on the articles, kind conversations and giving me opportunities in the world of science.

Bc. Jan Nikl

Název práce:

Vybrané aspekty numerických metod pro hydrodynamické simulace laserového plazmatu

Autor: Bc. Jan Nikl

Obor: Informatická fyzika
Druh práce: Diplomová práce

Vedoucí práce: Ing. Milan Kuchařík, Ph.D.
Konzultant: Dr. Stefan Andreas Weber, Ing. Milan Holec

Abstrakt:
V rámci této práce jsou vyvíjeny numerické metody pro 1D a 2D hydrodynamické kódy. Dvouteplotní popis nevazkou stlačitelnou tekutionou je aplikován v lagrangeovských souřadnicích, kde regularita 2D sítě je dosažena metodou ALE. Model absorpce laserového záření založený na stacionárních Maxwellových rovnicích je dále zkoumán a vylepšován pro numerickou robustnost a přesnost metody. Její aplikace do 2D navržená v rámci minulé práce je vylepšena pro dosažení vyššího řádu metody. Jsou porovnány sofistikované modely electron–iontových srážkových frekvencí. Schéma vedení tepla je aplikováno na dvouteplotní model a rozšířeno o teplotní relaxaci. Model nelokálního transportu záření a elektronů je doplněn o transport iontů. Provedené 1D a 2D numerické simulace jsou analyzovány a porovnány s literaturou.

Klíčová slova: lagrangeovská hydrodynamika, laserové plazma, numerické metody, dvouteplotní model, vedení tepla, absorpce laseru, nelokální transport, radiační transport

Title:

Some aspects of numerical methods for laser plasma hydrodynamics

Abstract:
Numerical methods for the 1D and 2D hydrodynamical codes are developed in the context of this thesis. Two-temperature description by a non-viscous compressible fluid is applied in Lagrangian coordinates, where regularity of the 2D mesh is maintained by the ALE method. The model of laser absorption based on stationary Maxwell's equations is studied and improved for numerical robustness and accuracy of the method. Its application in 2D, that has been developed in the previous academic work, is improved to attain higher order of the method. Sophisticated models of electron–ion collision frequencies are compared. The heat conduction scheme is applied on the two-temperature model and extended by the temperature relaxation. The ion transport is added to the model of non-local transport of radiation and electrons. Performed 1D and 2D simulations are analysed and compared with literature.

Key words: Lagrangian hydrodynamic, laser plasma, numerical methods, two-temperature model, heat conduction, laser absorption, non-local transport, radiation transport

Nomenclature

c	.....	speed of light in vacuum
π	.....	Archimedes' constant
e	.....	elementary charge
A	.....	relative atomic mass
Z	.....	average charge state
m_e	.....	electron mass
m_p	.....	proton mass
m_u	.....	unified atomic mass unit
m_i	.....	ion mass ($m_i \approx Am_u$)
k_B	.....	Boltzmann constant
h	.....	Planck constant
$\hbar$	.....	reduced Planck constant
ε_0	.....	vacuum permittivity
μ_0	.....	vacuum permeability

Contents

Introduction

Modelling of laser–target interaction is an appealing research topic, finding application in a large variety of complex physical problems. High expectations are being put to inertial confinement fusion (ICF) for example, that could solve the everlasting problem of energy production for whole mankind one day. For this reason, an extensive effort is made to numerically simulate with great accuracy the involved physical phenomena in the process of the interaction.

Several widely used approaches in this field of plasma physics include the kinetic codes, where the dynamics of the system is described in full phase space of spatial coordinates and momentum. The Boltzmann kinetic equation supplied by an appropriate collision operator governs the evolution of the system. In the context of plasma physics, Vlasov–Fokker–Planck equation (VFP), including self-consistent electric fields, is most common [1]. However, solution of the resulting partial differential equation in full seven dimensions (including the temporal domain) is extremely computationally expensive. In the limit of dominant collective behaviour of the plasma over the collisional processes, Vlasov equation arises. One of the most popular numerical approaches in this case is particle-in-cell method (PIC) [2]. However, both methods are applicable only on limited time scales due to high computational demands and they are not suited for the description of a dense, only partially ionized and highly collisional plasma appearing locally during the laser–target interaction.

Hydrodynamical simulations then present the most preferred way of the numerical modelling. The hydrodynamical description fundamentally originate from the velocity moments of the kinetic equation that form the equations of conservation. An appropriate closure model is then employed to close the system of coupled hydrodynamic equations, that is the equation of state in the case of hydrodynamics. The closed system of partial differential equations then can be computationally solved by an appropriate numerical scheme. However, two distinct approaches to description of the physical reality are recognized. The *Eulerian* approach is essentially a description of hydrodynamics from the point of view of a stationary external observer. Contrary, the *Lagrangian* approach follows the description in the reference frame co-moving with the fluid. Both points of view on the same physical phenomena are equivalent, but each of them is used in a different field of hydrodynamics. In the context of laser–target interaction, Lagrangian description is usually preferred, because the volume changes of the matter are extreme during the laser ablation and expansion.

Numerically, the computational mesh moves with the fluid, removing completely the convective part of the equations. The simulation codes following this procedure are known as *Lagrangian hydrodynamical codes*. Two codes of this kind are used and further developed in the context of this thesis. The first one is the 2D simulation code PALE2, that is being developed at the Department of Physical Electronics [3, 4]. It is able to perform the simulations in Cartesian and also cylindrical geometry, that essentially approximates full 3D evolution of the system assuming the axial symmetry of the problem for normal incidence of the laser beam. However, the problems inherent to the Lagrangian description in 2D naturally arise. The computational mesh is progressively deformed and can get even entangled at some point. *Arbitrary Lagrangian–*

Eulerian (ALE) methods are employed to prevent this pathological effect in the simulations [5, 6]. They combine the Eulerian and Lagrangian approaches together by introduction of an artificial velocity of the mesh in the case of the *direct ALE* or repetitively perform the Eulerian step in the *indirect ALE*. PALE2 follows the latter approach, where highly sophisticated methods ensure the conservation of the quantities. The two-temperature description of the fluid, i.e. with separate electron and ion temperatures, is implemented, but only the one-temperature model is available in the ALE regime. However, the performed simulations later in the thesis show that the effect on the global evolution of the system is minimal for longer laser pulses.

The second hydrodynamical code is the 1D simulation code PETE. The convective transport within the hydrodynamic simulations is not sufficient to describe complex transport mechanisms and thus an effort is made to enhance the equations of hydrodynamics by additional physical models. The most classical extension is the thermal diffusion, that is also a part of PALE2. However, the unique feature of code PETE is incorporation of the radiation transport and non-local transport of electrons as well. The radiation transport is very important part of the laser plasma simulations, especially in the context of ICF [7]. Moreover, the non-locality of the heat transport has been recognised several decades ago, but proper physical model suitable for hydrodynamical simulations has remained a stumbling-block and only approximate convolution models were used [8]. The novel model proposed in [9] solves this problem by a unified model of transport of electrons and photons, that is numerically solved by a high-order method based on finite elements, that is remarkably numerically efficient.

This work continues in the development of both codes, where the governing equations and applied discretization are briefly discussed, but the reader is pointed to the cited theses and the previous academic work [10], where more details can be found. However, the need of properly conservative numerical scheme was recognised and hence a numerical method to attain the conservation of the energy within the non-local transport model is introduced.

The indispensable part of the laser–target interaction simulations is a laser absorption algorithm. The simple methods of "absorption on critical density", where all laser power is absorbed at a single point essentially, or WKB approximation, describing the laser propagation in terms of geometrical optics, were found insufficient for precise simulations and thus the model based on stationary Maxwell's equations is employed and studied [11, 12]. However, the spatial scales appropriate for the laser absorption are considerably smaller than the hydrodynamical scale. The mesh refinement technique is improved here and also a new method specifically designed for the finite elements is proposed and implemented. Moreover, the basic algorithm is only 1D and hence not usable for 2D simulations. The method for application of it in 2D was developed in the previous work [13]. This work continues in this effort and the model is extended by bilinear interpolation, managing higher order of convergence of the method as also proven by a test problem.

As mentioned already, the physical closure is absolutely necessary for the numerical simulations. The equations of state incorporated in the simulation codes are briefly reviewed here. The coefficients related to the collision frequency are appearing at various places in the model and are also a part of this closure. They can be found

in the energy exchange between electrons and ions, permittivity for the laser absorption, heat conductivity coefficients and also the extinction coefficients for the non-local transport. Hence, the model of collision frequency is of a special interest, but the classical Spitzer-Härm formula [14] is not able to describe the low temperatures regime, where the ablation starts. More sophisticated models are implemented and compared here and also the related coefficients are derived from them.

The heat diffusion extension of the hydrodynamical equations is a part of classical hydrodynamical codes, including PALE2. The numerical scheme based on the method of mimetic operators was improved to attain the second order convergence in time in the previous work and it is now also implemented to code PETE to be able to compare the non-local and diffusion approaches together. Moreover, several heat flux limiters are implemented and their effects on the simulations are compared. Finally, electron–ion temperature relaxation is treated numerically and the heat diffusion scheme is applied on the two-temperature model here.

The unique non-local transport model of the hydrodynamical code PETE is discussed and the model is enhanced by the ion contribution. The finite element scheme is modified appropriately as well as the implementation itself. The improved laser absorption method, mentioned above, is also incorporated transparently. Stabilisation of the method was found to be beneficial in some cases and a physically based technique dedicated to this effort is proposed here.

Finally, all numerical methods are evaluated in a numerical experiment, where an extensive comparison is made including also 1D and 2D simulations in PETE and PALE2. The results are analysed and discussed here. The accuracy of the models is verified by a comparison with literature.

The rest of the thesis is organized as follows. Section 1 is dedicated to an overview of the governing equations of laser plasma hydrodynamics. Section 2 continues by description of the laser absorption algorithms and section 3 overviews the equations of state and shows the physical closure of the simulation in general. The heat diffusion is discussed and numerically solved in section 4. Later, section 5 discusses the non-local transport model and the respective finite element scheme. Finally, the results of numerical simulations are presented and analysed in section 6.

1 Laser plasma hydrodynamics

The foundations of laser plasma hydrodynamics are based on the hydrodynamical description of the system. Collisional plasma is approximated by a two-temperature non-viscous compressible fluid, whose dynamics in *Lagrangian coordinates* (i.e. the coordinates in the frame co-moving with the fluid) is governed by *Euler equations* in the form:

$$\frac{\partial \rho}{\partial t} = -\nabla \cdot \vec{u} \ , \tag{1}$$

$$\rho \frac{\partial \vec{u}}{\partial t} = -\nabla (p_i + p_e) \ , \tag{2}$$

$$\rho \frac{\partial \varepsilon_e}{\partial t} = -p_e \nabla \cdot \vec{u} \ , \tag{3}$$

$$\rho \frac{\partial \varepsilon_i}{\partial t} = -p_i \nabla \cdot \vec{u} \ , \tag{4}$$

where ρ stands for mass density, p_e and p_i denote electron and ion pressures, ε_e and ε_i are specific internal energies of electrons and ions and $\vec{u}$ represents the single fluid velocity. Together, the equations form differential *conservation laws* of mass, momentum, electron and ion energy respectively. To close the hydrodynamical system, it must be supplied by an *equation of state* (EOS). The equations of state included in the simulation codes PETE and PALE2 are reviewed in section 3.1. They provide the necessary dependence of electron and ion pressures on the density ρ and the specific internal energies ε_e and ε_i. Internally, these relations assume equilibrium two-temperature thermodynamics and quasi-neutrality condition to relate the number of species.

However, ideal hydrodynamic description is not sufficient for laser–target interaction simulations. The full *laser plasma non-local transport hydrodynamic model* modifies the energy equations (3), (4) as follows [9]:

$$\rho \left(\frac{\partial \varepsilon_e}{\partial T_e} \right)_\rho \frac{\partial T_e}{\partial t} + \rho \left(\frac{\partial \varepsilon_e}{\partial \rho} \right)_{T_e} \frac{\partial \rho}{\partial t} = -p_e \nabla \cdot \vec{u} + G_{ei}(T_i - T_e) - \nabla \cdot (\vec{q}_e + \vec{q}_R) - \nabla \cdot \vec{S} \ , \tag{5}$$

$$\rho \left(\frac{\partial \varepsilon_i}{\partial T_i} \right)_\rho \frac{\partial T_i}{\partial t} + \rho \left(\frac{\partial \varepsilon_i}{\partial \rho} \right)_{T_i} \frac{\partial \rho}{\partial t} = -p_i \nabla \cdot \vec{u} + G_{ie}(T_e - T_i) - \nabla \cdot \vec{q}_i \ . \tag{6}$$

The model introduces electron–ion temperature relaxation between the electron temperatures T_e and ion temperatures T_i as described in section 4.4. The non-local heat fluxes $\vec{q}_e$, $\vec{q}_i$, $\vec{q}_R$ were also added for electrons, ions and radiation. Their divergence then causes deposition of energy at given point and couples the equations with transported species. The heat fluxes are supplied from the non-local closure presented in section 5. However, classical thermal diffusion can be transparently inserted instead, where diffusion heat fluxes $\vec{W}_e$ and $\vec{W}_i$ computed according to section 4 are assigned to $\vec{q}_e$ and $\vec{q}_i$ respectively. The $\nabla \cdot \vec{S}$ term performs laser–plasma coupling, depositing energy of the laser wave and heating up electron species and altering the refraction index of the plasma in the end. Finally, chain rule was applied on the left hand side, where

the thermodynamic relations $\varepsilon_e(\rho, T_e)$ and $\varepsilon_i(\rho, T_i)$ are supposed to be known from the equation of state. This procedure allows construction of a single implicit scheme in temperatures for non-local transport and electron–ion relaxation eventually.

Numerically, the scheme utilizes *operator splitting method* [15, 16] and the implicit part comprising of the non-local transport or the diffusion are not solved together with the hydrodynamical part in the computational sequence. Instead, the equations of ideal hydrodynamics (1–4) are solved separately by an explicit *compatible scheme* [17]. *Predictor–corrector* technique is then applied to attain the second order convergence in temporal domain. However, the scheme is not detailed here, since the 1D version was largely covered in the previous work [10] and details about the 2D variant, making the foundations of PALE2 code, can be found in [3].

Important feature of the hydrodynamic scheme that must be noted is conservation of mass, momentum and energy, that maintains the simulation close to the physical reality for arbitrarily late times of evolution of the system. The conservation property is also related to employed *staggered* spatial discretization. It means that the scalar potentials (in the sense of general transport equation) like the density ρ, pressures p_e, p_i, temperatures T_e, T_i, etc. are discretized inside the computational cells and denoted by integer sub-index. In contrast, vector fluxes like the velocity $\vec{u}$, heat fluxes $\vec{q}_e$, $\vec{q}_i$, $\vec{q}_R$, etc. are discretized at the cell boundaries and labelled by half-integer sub-indices as depicted in Figure 1 for 1D. Consequently, central differences can be used in the transport equations (1–6) and the second order in spatial domain is achieved. Moreover, Lagrangian computational mesh is used consistently with the Lagrangian formulation of the equations of hydrodynamics (1–4). The mesh then flows with the fluid, maintaining the cell masses constant throughout the simulation. The Lagrangian character is extraordinarily advantageous for simulations, where extreme change of volumes occurs, as it typically happens during laser–target interaction.

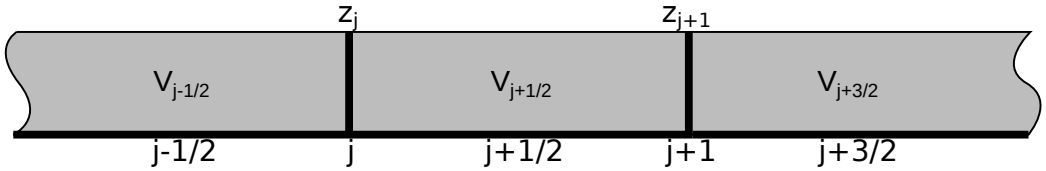

Figure 1: A schematic visualisation of the staggered spatial discretization in 1D. The node positions z_j and cell volumes $V_{j+1/2}$.

A known issue common to all 2D Lagrangian hydrodynamical codes is that the mesh can get entangled during the simulation, when the flow is turbulent for example. *Arbitrary Lagrangian–Eulerian* (ALE) approach then offers a solution for this rudimentary problem [3, 18, 4, 19]. The computational mesh is untangled/smoothed in a *rezone* step and the conservative quantities are then *remapped* on the new mesh. The ALE method is also useful for maintaining the mesh sufficiently smooth and regular. Therefore, it is largely utilized when the 2D laser absorption model presented in section 2.2 is employed, which requires sufficiently dense computational mesh in vicinity of the critical plane.

1.1 Conservative update of thermodynamic quantities

Conservation of momentum and mass within the hydrodynamical scheme has been discussed so far. However, conservation of energy was satisfied only for the equations of energy in ideal hydrodynamics approximation (3), (4), but not for the full laser plasma non-local transport hydrodynamic model (5), (6). When the operator splitting technique is applied, the equations without the hydrodynamical part simplify to:

$$\rho\left(\frac{\partial\varepsilon_e}{\partial T_e}\right)_\rho\left(\frac{\partial T_e}{\partial t}\right)_{split} = G_{ei}(T_i - T_e) - \nabla\cdot(\vec{q}_e + \vec{q}_R) - \nabla\cdot\vec{S}\ , \tag{7}$$

$$\rho\left(\frac{\partial\varepsilon_i}{\partial T_i}\right)_\rho\left(\frac{\partial T_i}{\partial t}\right)_{split} = G_{ie}(T_e - T_i) - \nabla\cdot\vec{q}_i\ . \tag{8}$$

The time derivatives were labelled by *split* in order to distinguish them from the full derivatives, because only an isochoric evolution of the system without the effect of hydrodynamics is considered here due to the splitting, but the full temporal evolution is not necessarily isochoric in any mean in general.

As mentioned earlier, the formulation of the equations of energy (7), (8) in temperatures allows the construction of an implicit scheme in temperatures for the non-local transport and eventually the electron–ion energy exchange, because the non-local transport closure is also temperature dependent. This approach is beneficial, because strong coupling between plasma and transported species can be simulated without restrictions on extremely short time steps. Moreover, thermodynamic quantities provided by an EOS are functions of density and temperature (see section 3.1), so the calculation of temperature from internal energy requires inversion of the EOS (i.e. *inverse equation of state*), that is computationally expensive. On the other hand, the energy conservation is not maintained, when general non-linear dependency of ε_e or ε_i on temperature is considered and the specific heats $(\partial\varepsilon_e/\partial T_e)_\rho$, $(\partial\varepsilon_i/\partial T_i)_\rho$ are treated as a constant coefficients. Classically, the system should be treated as non-linear in temperatures and a global system of equations should be constructed, but the resulting Jacoby matrix can be very large and dense in general due to non-local nature of the transport. Solution of the linearised system is then computationally expensive and not feasible in practice. A cure for this problem was developed, that is known as *Symmetrical Semi-Implicit* (SSI) method [20, 21]. The basic idea behind it is to solve the linearised equations for the non-local contributions and then locally correct the solution to converge to the non-linear conservative solution. When time discretization is performed and discrete time levels are denoted by integer upper indices, an auxiliary intermediate time level $n + 1/2$ is added and the update of temperatures according to the equations (7), (8) takes place between the time levels n and $n + 1/2$. Then SSI method performs additional update of temperatures from the level $n + 1/2$ to n as

follows:

$$\left(\frac{\partial \varepsilon_e}{\partial T_e}\right)_\rho^{n+1/2} \frac{T_e^{n+1} - T_e^{n+1/2}}{\Delta t} = \beta_{SSI} \left(\varepsilon_e^{n+1/2} - \varepsilon_e(\rho, T_e^{n+1/2})\right) \ , \tag{9}$$

$$\left(\frac{\partial \varepsilon_i}{\partial T_i}\right)_\rho^{n+1/2} \frac{T_i^{n+1} - T_i^{n+1/2}}{\Delta t} = \beta_{SSI} \left(\varepsilon_i^{n+1/2} - \varepsilon_i(\rho, T_i^{n+1/2})\right) \ , \tag{10}$$

where Δt is the length of the time step in this context and β_{SSI} is a given constant in the range $0 < \beta_{SSI} < 1$ in order to achieve convergence of the method, but it was set $\beta_{SSI} = 0.5$ for all performed simulations. The discretized specific internal energies $\varepsilon_e^{n+1/2}$ and $\varepsilon_i^{n+1/2}$ are obtained from the update of temperatures through the discretized equations (7) and (8):

$$(\varepsilon_e^{n+1/2} - \varepsilon_e^n) = \left(\frac{\partial \varepsilon_e}{\partial T_e}\right)_\rho^n (T_e^{n+1/2} - T_e^n) \ , \tag{11}$$

$$(\varepsilon_i^{n+1/2} - \varepsilon_i^n) = \left(\frac{\partial \varepsilon_i}{\partial T_i}\right)_\rho^n (T_i^{n+1/2} - T_i^n) \ . \tag{12}$$

Conservation of energy then holds in $\rho\varepsilon_e$ and $\rho\varepsilon_i$, but the scheme can be implicit in temperatures, that are maintained approximately consistent with the energies without a need of inversion of EOS. It has been observed that the relative discrepancies are usually lower than $< 10^{-5}$ with this method.

2 Laser absorption

Laser absorption is the main driving force in all *laser plasma* simulations and thus the laser absorption algorithm is an indispensable part of all numerical codes of this kind. Here, we are interested in laser–target interaction, where the target is usually made of solid material. After the irradiation of such target by a laser beam, highly dense and collisional plasma is created above the surface.

Inverse Bremsstrahlung is then assumed to be the main absorption mechanism for (near-)visible laser wavelengths λ_0 and particle-in-cell simulations show that incident beam intensities up to $I_{laser}\lambda_0^2 \lesssim 10^{17}$ (W/cm^2)μm^2, where relativistic and non-collisional effects can be neglected [22]. During this phenomenon, electrons are being scattered on heavier ions with collision frequency ν_{ei}. When considering more general model and collisions with other (quasi)particles, a general *electron momentum loss collision frequency* ν_e is taken instead. The global models of ν_e used in the simulation code are detailed in section 3.2.

The dispersion relation for linear harmonic electromagnetic (EM) waves with angular frequency ω_0 and wave number k takes the form:

$$\omega_0^2 = \omega_{pe}^2 + kc \ , \tag{13}$$

where ω_{pe} stands for the electron plasma frequency, that is defined as:

$$\omega_{pe}^2 = \frac{e^2 n_e}{\varepsilon_0 m_e} \ . \tag{14}$$

The symbol n_e represents electron density in the given plasma medium in this context. The resonant condition for the EM wave is then given by $\omega_0 = \omega_{pe}$. When expressed in terms of electron density, the *critical density* of the medium is obtained:

$$n_c = \frac{m_e \varepsilon_0}{e^2}\omega_0^2 = 4\pi^2 c^2 \frac{m_e \varepsilon_0}{e^2 \lambda_0^2} \ , \tag{15}$$

where $\lambda_0 = 2\pi c/\omega_0$ is the vacuum wavelength of the EM wave. The wave then does not propagate any further behind this point and is exponentially attenuated according to *Beer-Lambert law* near the *critical plane* in the range of single wavelength or more specifically in so called *penetration depth* given by $\delta_{pen} = \lambda_0/(2\pi\,\chi)$, where $\chi = \mathrm{Im}\ \hat{n}$. The complex refraction index $\hat{n} = n + i\chi$ appearing in the previous expression can be approximated in a metallic or collisional plasma medium as [23]:

$$\hat{n}^2 = \hat{\varepsilon} = 1 - \frac{\omega_{pe}^2}{\omega_0(\omega_0 + i\nu_e)} \ . \tag{16}$$

The term incorporating the collision frequency ν_e explains the statements above, because the complex relative permittivity $\hat{\varepsilon}$ is dominated by the imaginary part, when EM wave approaches the critical plane, i.e. $n_e \to n_c$, $\omega_{pe} \to \omega_0$. Energy is then deposited into the plasma, this effect is reflected by the divergence of the laser wave Poynting vector div$\vec{S}$ that acts as one of the source terms on the right hand side of the

energy conservation equation (5) in the hydrodynamical scheme. Power of the laser wave is then obviously conserved in the scheme, although reflections in plasma can be taken into account and only a fraction of the incident laser intensity is effectively absorbed.

The fundamental mechanism of the absorption gives rise to the simplest laser absorption algorithm denoted as "absorption on critical density". Laser beam is losslesly propagated through the medium until the critical plane is reached. Then the power of the incident laser beam is absorbed in first super-critical computational cell. There is present the total effectivity of the absorption, but its determination is not given self-consistently in the basic algorithm and must be externally supplied. Overall properties of the algorithm are poor, because it creates high temperature gradients and fails to simulate dynamics of the ablation, especially for lower intensities as concluded in the previous work [13]. However, it is suitable for comparison of different algorithms and techniques or sufficient for some one-temperature simulations with high fluence lasers [24].

In this text, different approach is chosen for purposes of detailed one-temperature and two-temperature simulations. This algorithm is based on the full 1D solution of Maxwell's equations in spatial domain that is referred to as *Stationary Maxwell's Equations* (SME) algorithm. Its description is given in section 2.1.

Finally, a technique for application of the absorption code in 2D simulations was developed. In connection with *Arbitrary Langragian-Eulerian* (ALE) method for computational mesh smoothing implemented in PALE2 code [4, 3], it offers a feasible method for laser plasma simulations. This algorithm is introduced later in section 2.2.

2.1 Stationary Maxwell's Equations algorithm

In order to solve laser propagation and attenuation in an inhomogeneous medium in one dimension (1D), a fully wave-based algorithm constructing a complete stationary EM field is used. This algorithm originates from [25] and has been further enhanced at the Department of Physical Electronics throughout the years [12, 11]. It essentially solves Maxwell's equations in spatial domain assuming that temporal resolution of hydrodynamical simulations $\sim$ 1 ps is much lower than a typical laser wave period $\sim$ 1 fs. Full details of the inference are beyond the scope of this text, but we refer to some of the key aspects of the algorithm later, so a brief outline of the algorithm is given.

Not taking into account free currents and charges in the medium following the quasi-neutrality closure of hydrodynamic equations, macroscopic Maxwell's equations can be written as:

$$\begin{aligned} \nabla \times \vec{E} + \frac{\partial \vec{B}}{\partial t} = 0 \ , \quad \nabla \cdot \vec{B} = 0 \ , \\ \nabla \times \vec{H} - \frac{\partial \vec{D}}{\partial t} = 0 \ , \quad \nabla \cdot \vec{D} = 0 \ , \end{aligned} \tag{17}$$

where $\vec{D}$ and $\vec{H}$ represents electric displacement field and magnetic field intensity respectively. Note that the notations of complex and real valued fields are not distin-

guished for brevity of the text, but the complex valued fields are used henceforth and the real valued fields can be obtained as the real part of them. Provided scalar relative complex permittivity $\hat{\varepsilon}$ (16) and relative magnetic permeability $\mu \approx 1$, the following holds for electric and magnetic fields:

$$\vec{B} = \mu_0 \vec{H} \ , \quad \vec{D} = \varepsilon_0 \hat{\varepsilon} \vec{E} \ . \tag{18}$$

Substituting these relations back to (17) and considering planar wave propagating along z axis, i.e. $\vec{E} = (E_x, 0, 0)$, $\vec{H} = (0, H_y, 0)$ and $\partial\vec{E}/\partial x = 0, \partial\vec{E}/\partial y = 0, \partial\vec{H}/\partial x = 0, \partial\vec{H}/\partial y = 0$, the temporal evolution of the fields in 1D is described by the system:

$$\begin{aligned} \frac{\partial E_x}{\partial z} + \mu_0 \frac{\partial H_y}{\partial t} &= 0 \ , \\ \frac{\partial H_y}{\partial z} + \hat{\varepsilon}\varepsilon_0 \frac{\partial E_x}{\partial t} &= 0 \ . \end{aligned} \tag{19}$$

Harmonic temporal evolution of the fields is then assumed in the form:

$$E_x = E(z) e^{-i\omega_0 t} \ , \quad H_y = H(z) e^{-i\omega_0 t} \ . \tag{20}$$

Substituting the fields definition (20) back to (19) and eliminating $H = H(z)$ from both equations, the *Helmholtz equation* is obtained:

$$\frac{\partial^2 E}{\partial z^2} = -\frac{\omega_0^2}{c^2} \hat{\varepsilon} E \ . \tag{21}$$

When considering $\hat{\varepsilon}$ homogeneous for the moment, this linear second-order ordinary differential equation in spatial domain has the well-known solution composed of two oppositely propagating planar waves with $E = E(z)$ expressed as follows:

$$P(z) = P_0 e^{-ikz} \ , \quad R(z) = R_0 e^{ikz} \ , \tag{22}$$

where the wave number is $k = \frac{\omega_0}{c}\sqrt{\hat{\varepsilon}} = k_0\sqrt{\hat{\varepsilon}}$.

The first term in (22) is the incident wave and the second one is the reflected wave, where the constants P_0 and R_0 are determined by boundary conditions. The Helmholtz equation (21) then can be decomposed into the system of first-order ordinary differential equations governing the propagation of each of the waves:

$$\frac{\partial P}{\partial z} + ikP = 0 \ , \tag{23}$$

$$\frac{\partial R}{\partial z} - ikR = 0 \ . \tag{24}$$

The complete EM field then can be expressed as a superposition of these waves $E = R + P$, $H = \sqrt{\varepsilon_0/\mu_0}\sqrt{\hat{\varepsilon}}(R - P)$.

The (complex) coefficient of reflection is defined as the ratio of both waves, i.e. $V = R/P$. Complementary, the quantity $A = 1/4|P|^2 = 1/4PP^*$ is introduced. The system (23), (24) then can be transformed to the new set of variables V and A

as follows:

$$\frac{\partial V}{\partial z} - i2kV = 0 \ , \tag{25}$$

$$\frac{\partial A}{\partial z} + i2k_0\chi A = 0 \ . \tag{26}$$

The system is also formed of linear complex ordinary differential equations with the formal solution similar to (22):

$$V(z) = V_0 e^{i2kz} \ , \quad A(z) = A_0 e^{-i2k_0\chi z} \ . \tag{27}$$

However, the resulting real time-averaged Poynting vector is of the main interest here as mentioned in the introduction of this section. It is defined as:

$$\vec{S} = \frac{1}{4}(\vec{E} \times \vec{H}^* + \vec{E}^* \times \vec{H}) \ , \quad S_z = \frac{1}{4}(E_x {H_y}^* + {E_x}^* H_y) \ . \tag{28}$$

With some effort, S_z can be rewritten in terms of V and A as [11]:

$$S_z = A(n(|V|^2 - 1) - 2\chi \mathrm{Im}\ V) \ . \tag{29}$$

Piecewise constant approximation of $\hat{n}$ is then assumed, justifying the constant $\hat{\varepsilon}$ in the inference. Note that this is in a good agreement with the spatial staggered discretization used in the hydrodynamical scheme (see section 1), because it can be observed that $\hat{n}$ calculated from (16) is a function of only central quantities (i.e. constant within computational mesh cell) and it must be naturally central too. Unlike a computational mesh cell that poses a homogeneous medium, nodes represent step optical interfaces. The reflection coefficient coefficient V is discretized in a conformal way on them, where left and right values on each node are evaluated. Also the coefficient A is discretized in the same manner. Using the waves formulas (27), the relations connecting values A and V on the opposing sides of the cells are derived [11]. Another set of relations is obtained from the application of interface conditions on the mesh nodes, i.e. continuity of transverse components of E and H. Together the relations form a complete system of equations for A and V provided that their respective values are known at least at some point. This piece of information is supplied by two boundary conditions in 1D (or initial conditions from the point of view of ordinary differential equations for A and V). The first one is the value of A on the right boundary of the absorption area z_{max}, where $A(z_{max})$ is equal to the intensity of the laser beam I_{laser}, because the definition of A coincides with the Poynting vector (29) in vacuum. The second restriction is applied on V, which is supposed to vanish at some point referred to as z_{min}. The procedure to estimate the position of z_{min} is based on proper calculation of the penetration depth δ_{pen} behind the critical plane at z_c. This leads to the requirement implicitly defining z_{min}:

$$\frac{\omega_0}{2\pi c} \int_{z_{min}}^{z_c} \mathrm{Im}\ \sqrt{\hat{\varepsilon}} > C_{z_{min}} \ , \tag{30}$$

where $C_{z_{min}}$ is an arbitrary constant set to $C_{z_{min}} = 4$ in all presented simulations. The left boundary condition is then $V(z_{min}) = 0$. The global layout is depicted in Figure 2.

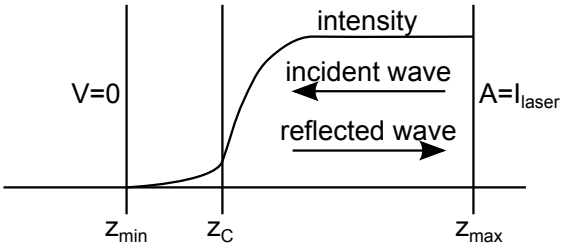

Figure 2: A schematic representation of the spatial configuration in SME algorithm.

The algorithm proceeds as follows: values of V are calculated from z_{min} node by node until z_{max} is reached. In contrast, A is propagated from z_{max} in the opposite direction. When all values of A and V are computed, Poynting vector S_z is finally calculated from the values according to (29). Its divergence $\mathrm{div}\vec{S} = \partial S_z/\partial z$ appearing in the electron energy equation (5) is then calculated using central finite difference, that is:

$$(\mathrm{div}\vec{S})_{j+1/2} = \frac{(S_z)_{j+1} - (S_z)_j}{z_{j+1} - z_j} \ , \tag{31}$$

using the index notation of section 1.

Some remarks to the algorithm should be given. Firstly, despite that some simplifications were assumed, the algorithm still remains highly accurate and reconstructs complete EM field, so it outperforms the "absorption on critical density" algorithm or often used WKB approximation [26]. Secondly, it is completely self-consistent unlike the other two algorithms and thus it does not need any other relations than a model of permittivity $\hat{\varepsilon}$ and does not end up in vicinity of the critical density like WKB and "absorption on critical density", that have to be supplied by the total reflectivity/efficiency coefficient.

Because of the wave nature of the algorithm, it can also model stationary waves in front of the critical plane originating from interference of the incident and reflected wave. To demonstrate this phenomena, following profiles of quantities were used in a solely laser absorption simulation:

$$n_e(z) = n_{e0} + (n_{eN_C} - n_{e0})\frac{\exp(-10\frac{z-z_0}{z_{N_C}-z_0}) - 1}{\exp(-10) - 1} \ , \tag{32}$$

$$T_e(z) = T_i(z) = T_0 \ + (T_{N_C} \ - \ T_0)\frac{\exp(-10\frac{z-z_0}{z_{N_C}-z_0}) - 1}{\exp(-10) - 1} \ . \tag{33}$$

Quantities T_e and T_i are electron and ion temperatures respectively. The following parameters has been set:

$$\begin{aligned} &z_0 = 0 \ \mu\mathrm{m} \ , \quad z_{N_C} = z_{max} = 5 \ \mu\mathrm{m} \ , \quad n_{e0} = 6\, n_c \ , \quad n_{eN_C} = 0.2\, n_c \ , \\ &T_0 = 10 \ \mathrm{eV} \ , \quad T_{N_C} = 100 \ \mathrm{eV} \ , \qquad Z = 13 \ , \qquad A = 27 \ , \end{aligned} \tag{34}$$

where z_0 and z_{N_C} are boundaries of the computational domain. Intensity of the incident laser beam was set $I_{laser} = 1$ (in relative units due to linearity of the absorption mechanism). Vacuum wavelength of the laser was $\lambda_0 = 1.04$ μm in correspondence to the numerical simulations in section 6 (the base frequency is taken here). The resulting profiles of quantities are plotted in Figure 3 for different number of equidistantly placed computational cells N_C.

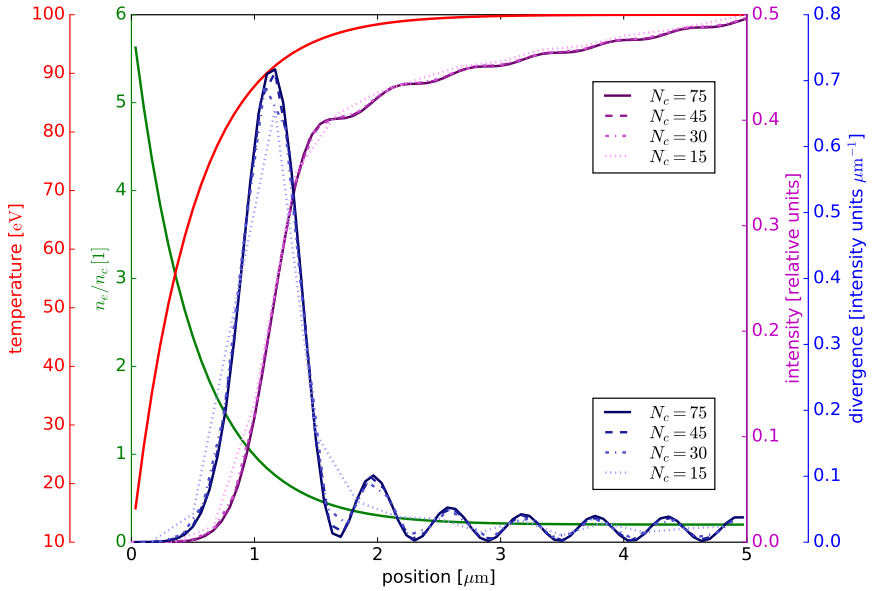

Figure 3: Comparison of laser absorption for different number of computational cells N_C.

The stationary waves formation is clearly visible there. However, some peaks are undersampled for lower number of cells and some disappear totally. Especially for the lowest number of cells, the curve of intensity seems to be smooth and one may be mistakenly convinced of its validity assuming operation of the algorithm in a limit of small waves with respect to computational cells. Unfortunately, this is not true and the algorithm can completely fail, because each wave must be sufficiently sampled due to wave nature of the algorithm. As closer investigation of the plot reveals, total reflectivity of the medium changes with the number of cells. Moreover, it is altered by the movement of the mesh during the simulation.

This phenomenon was imitated by displacing all inner mesh nodes up to one half of their mutual distance, i.e. $1/2(z_{N_C} - z_0)/N_C$. Resulting dependence of total reflectivity on the displacement is shown in Figure 4. The reflectivity clearly depend on the displacement and this effect increases for more severe undersampling. Besides that, there is visible dependency on the size of the computational cells. The algorithm clearly converges to a single solution for high N_C, but relatively slowly. These dependencies lead to creation of artificial spatial frequencies and other negative effects generally known as *aliasing*.

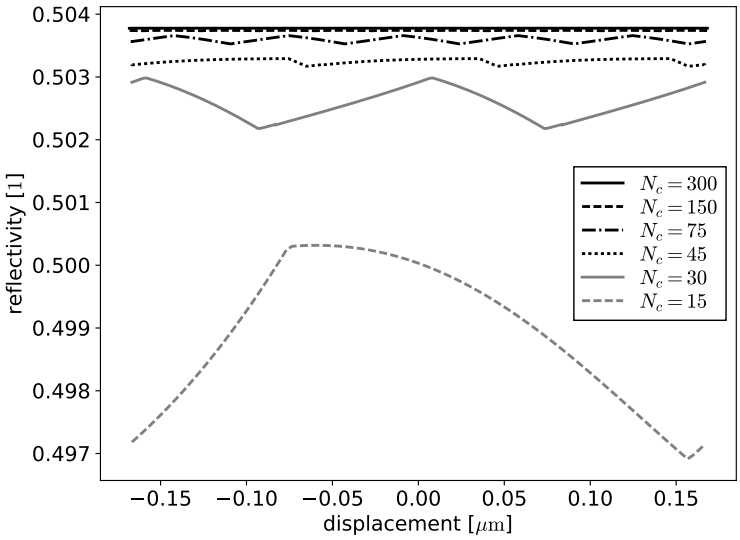

Figure 4: Dependence of total reflectivity on displacement of the computational nodes (maximal displacement was $1/2(z_{N_C} - z_0)/N_C$, full image was obtained by periodical prolongation of the curves).

2.1.1 Mesh refinement

In order to minimize the artefacts recognised in the previous section, which in some cases overgrow real profiles, the following fix was developed. It consists of linear reconstruction or interpolation of the temperature (electron and ion), density and ionization profiles onto a sub-mesh and consequent laser absorption on it. Finally, computed values are projected on the original computational mesh and used instead of the directly calculated ones. This approach is computationally significantly less expensive than refining the main mesh. However, the dependence on cell size and position of computational nodes is not removed completely.

The piecewise linear reconstruction/interpolation has been chosen for both simulation codes, providing convenient results together with reliability and reasonable computational costs. Interpolation method is used for the 2D simulation code PALE2 as described in section 2.2. On the other hand, reconstruction method is preferred in case of the code PETE, where higher intensities occur and *Arbitrary Lagrangian–Eulerian* method (ALE) is not available to smooth the computational mesh [4, 3, 19]. Under these conditions, the reconstruction is more reliable as discussed below.

Equidistant refinement is applied in both codes in the absorption area $\langle z_{min}, z_{max}\rangle$. In case of 1D code PETE, a reasonable criterion based on *Nyquist–Shannon sampling theorem* is made (the notation of discretized functions follows section 1):

$$\lambda_0/\mathrm{Re}\,\sqrt{\hat{\varepsilon}_{j+1/2}}/(x_{j+1} - x_j) \geq C_{SME} > 2\ . \tag{35}$$

The value of the constant C_{SME} is then chosen with respect to balance of computational

costs and performance of the algorithm. The constant was typically set to $C_{SME} = 10$, since spatial variation of $\hat{\varepsilon}$ is not taken into account in the formula and the most of the computational time is usually spent on non-local transport algorithm presented in section 5.

Mesh refinement for SME algorithm was proposed in [11]. Central quantity f is approximated by a piecewise linear function as:

$$f_{j+1/2}^{unlim}(x) = f_{j+1/2} + \left(\frac{\partial f}{\partial x}\right)_{j+1/2}^{unlim} (x - x_{j+1/2}) \ . \tag{36}$$

Term $(\partial f/\partial x)^{unlim}$ is an approximation of the spatial derivative using central difference:

$$\left(\frac{\partial f}{\partial x}\right)_{j+1/2}^{unlim} = \frac{f_{j+3/2} - f_{j-1/2}}{x_{j+3/2} - x_{j-1/2}} \ . \tag{37}$$

The piecewise linear function constructed this way clearly keeps the integral value over each cell same as the original piecewise constant function (i.e. $\int_{x_j}^{x_{j+1}} f_{j+1/2}^{unlim}(x)\,\mathrm{d}x = f_{j+1/2}(x_{j+1} - x_j)$). This property is extraordinarily beneficial in regions of steep gradients, where position of the gradient is approximately kept in place. When used in the context of laser absorption, if this condition is not met it can lead to a deformation of the intensity distribution and total reflectivity as shown in Figure 5.

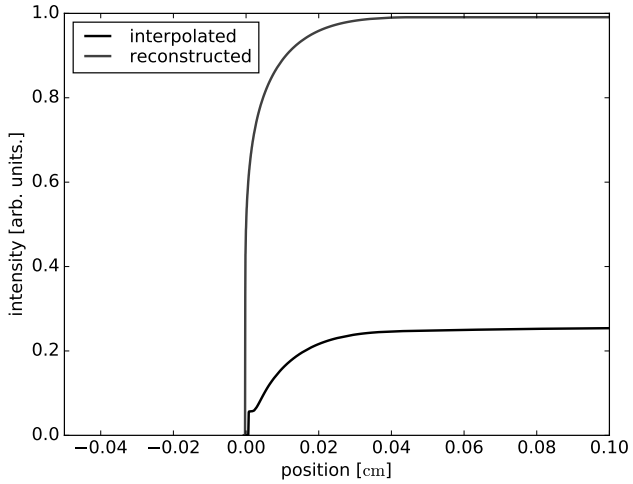

Figure 5: A typical effect of the intensity profile deformation occurring with the interpolation method compared to the reconstruction method in simulation code PETE.

However, the reconstructed function can create new local extrema. This phenomenon can lead to creation of numerical instabilities in the simulations. In order to avoid this behaviour, the approximation of the derivative needs to be limited. *Barth–Jespersen limiter* is employed in this case [27]. The limited approximation of the

derivative then takes the form:

$$\left(\frac{\partial f}{\partial x}\right)_{j+1/2} = \Phi^{BJ}_{j+1/2} \left(\frac{\partial f}{\partial x}\right)^{unlim}_{j+1/2} , \tag{38}$$

where $\Phi^{BJ}_{j+1/2} = \min\{\Phi^{BJ}_{j+1/2,j}, \Phi^{BJ}_{j+1/2,j+1}\}$. The nodal limiters are defined as follows:

$$\Phi^{BJ}_{j+1/2,j} = \begin{cases} \min\left(1, \frac{f^{max}_{j+1/2} - f_{j+1/2}}{f^{unlim}_{j+1/2}(x_j) - f_{j+1/2}}\right) & f^{unlim}_{j+1/2}(x_j) - f_{j+1/2} > 0 \\ \min\left(1, \frac{f^{min}_{j+1/2} - f_{j+1/2}}{f^{unlim}_{j+1/2}(x_j) - f_{j+1/2}}\right) & f^{unlim}_{j+1/2}(x_j) - f_{j+1/2} < 0 \\ 1 & f^{unlim}_{j+1/2}(x_j) - f_{j+1/2} = 0 \end{cases} . \tag{39}$$

Terms $f^{max}_{j+1/2}$ and $f^{min}_{j+1/2}$ are given for each computational cell as:

$$f^{min}_{j+1/2} = \min\{f_{j-1/2}, f_{j+1/2}, f_{j+3/2}\} , \quad f^{max}_{j+1/2} = \max\{f_{j-1/2}, f_{j+1/2}, f_{j+3/2}\} . \tag{40}$$

The limiter ensures that local extrema $f^{max}_{j+1/2}$ and $f^{min}_{j+1/2}$ are not exceeded by the reconstructed function inside the particular cell $j + 1/2$. The limited approximation of the derivative (38) then replaces the "unlimited" one in (36) and the limited reconstruction of the function is obtained finally.

2.1.2 Refinement on the finite elements

The mesh refinement algorithms presented so far are based on the *staggered* spatial discretization used for the hydrodynamical scheme in section 1. However, simulation code PETE includes the non-local transport model presented in section 5, that has the numerical scheme constructed with *finite element method* (FEM). One of the quantities discretized on the finite elements is electron temperature, that naturally also plays major role in the laser absorption, since the refraction index $\hat{n}$ is strongly dependent on it according to (16) and section 3.2. The idea of further mesh refinement is to utilize these *degrees of freedom* of the finite elements to refine the mesh, because increasing of the spatial order of the elements is computationally significantly less expensive than increasing the number of cells of the main mesh. Unlike the reconstruction/interpolation methods, the degrees of freedom of the finite elements actually contain additional information about the temperature profile and gradients of hydrodynamical quantities are not smeared when the spatial order is increased.

However, the laser absorption algorithm can still operate only on the basis of piecewise constant functions and thus a projection method must be constructed. Following the notation of section 5.2, the spatial basis of electron temperatures is denoted as ξ and the discrete representation of electron temperatures inside the element as $\mathbf{T}_e$. The segments of the refined mesh inside the elements are denoted as V^{Δ}_j and their number is equal to the number of degrees of freedom of the element N_{T_e} from the reasons explained later. The segments are equidistantly spaced, but eventually different approach can be used instead. The piecewise constant approximated temperatures are

written as $\mathbf{T}_e^{\Delta}$.

The key property of the projection is the conservation on each segment j:

$$\int_{V_j^{\Delta}} T_e \,\mathrm{d}x \approx \int_{V_j^{\Delta}} (\mathbf{T}_e^{\Delta})_j \,\mathrm{d}x = (\mathbf{T}_e^{\Delta})_j \left\| V_j^{\Delta} \right\| = \sum_l (\mathbf{T}_e)_l \int_{V_j^{\Delta}} \xi_l \,\mathrm{d}x = \int_{V_j^{\Delta}} \xi^T \cdot \mathbf{T}_e \,\mathrm{d}x \ . \quad (41)$$

Dividing the equation by the segment volume $\left\| V_j^{\Delta} \right\|$, the projection matrix $\mathbb{P}$ is obtained:

$$(\mathbf{T}_e^{\Delta})_j = \left(\frac{\int_{V_j^{\Delta}} \xi_l \,\mathrm{d}x}{\left\| V_j^{\Delta} \right\|} \right)_{jl} (\mathbf{T}_e)_l = \mathbb{P}_{jl} (\mathbf{T}_e)_l \ . \quad (42)$$

The projection matrix must be calculated using numerical integration in general, but it is invariant to cell scaling in 1D and thus it is normally calculated only at the beginning of the simulation, lowering the computational costs this way. Using the relation (42), discrete temperatures on the segments are determined and the laser absorption algorithm with optional reconstruction and further mesh refinement is performed. The Poynting vector divergences are computed and the process of projection on refined mesh must be reversed. Since the absorbed power of the laser is supposed to remain unchanged, conservative projection is preferred even in the reverse direction. Moreover, consistency of the projections shall be maintained. Hence, the inverse projection is used:

$$\mathbf{div}\,\mathbf{S} = \mathbb{P}^{-1} \cdot \mathbf{div}\,\mathbf{S}^{\Delta} \ , \quad (43)$$

where $\mathbf{div}\,\mathbf{S}$ and $\mathbf{div}\,\mathbf{S}^{\Delta}$ represent the discretized $\nabla \cdot \vec{S}$ term in the FEM scheme and in the laser absorption algorithm respectively. The projection matrix must be rectangular in order to has the inverse and this criterion enforces the same number of the segments and degrees of freedom as stated before. Regularity is then evident from the construction of the matrix (42). Finally, it must be noted that differential absorption within the computational cells leads to discontinuities of temperatures under some circumstances, even though the *Discontinuous Galerkin Finite Elements* (DG FEM) converge in the mean values. This problem is addressed later in the section about stabilisation of the method (5.2.1).

2.2 Extension to two dimensions

The algorithm based on SME presented in section 2.1 is directly implemented in the 1D simulation code PETE. However, it cannot be directly extended into 2D, because the full stationary solution of Maxwell's equations poses an extremely computationally expensive task there. Simpler approaches are usually preferred like the "absorption on critical density" algorithm, but it inherits the disadvantages of 1D version mentioned in the introduction. Another feasible solution are the *ray–tracing* algorithms, which simplify the task by means of geometrical optics. Propagation and reflection of finite number of rays is computed resulting in a final laser absorption estimation. Algorithms of this kind are being developed at the Department of Physical Electronics [28], but they are not able to smoothly reproduce the gradients of intensity under certain

circumstances.

Hence, a different approach is followed instead. It is directly based on the SME algorithm presented in section 2.1, but only 1D description is used, assuming that the rays impinge the target perpendicularly. This condition has a limited validity, because tightly focused lasers cannot be simulated this way and an effect of the mechanism of resonance absorption is underestimated. On the other hand, the simulations with wider laser focus have usually only slightly deformed profile of the critical plane (see section 6) and the incident rays are almost perpendicular. The cornerstone of the method based on 1D SME is a *global mapping algorithm* that maps the necessary quantities for the 1D laser absorption algorithm from the main computational mesh on an auxiliary mesh. This algorithm with originally piecewise constant interpolation of the quantities was developed in the previous work [13]. Here, the algorithm is extended to use a *bilinear interpolation* on the main mesh to improve the spatial resolution within the laser absorption scheme. However, the functions on the auxiliary mesh remain piecewise constant in order to maintain consistency with the SME algorithm.

The first step of the algorithm is construction of the auxiliary mesh that is similarly to section 2.1 denser than the main mesh in order to sample sufficiently the stationary laser waves. More precisely, the algorithm requires the following properties of the mesh:

1. the auxiliary mesh must fully cover the main mesh,
2. it is rectangular,
3. there can be no more than one mesh node of the main mesh in each cell of the auxiliary mesh.

Especially the last point is difficult to satisfy within the mesh generator. The algorithm basically averages the positions of the main mesh nodes and the last condition is checked additionally. The ratio of the number of auxiliary cells per approximately one main cell is fixed (referred to as the refinement factors later). However, the number of auxiliary mesh cells can reach enormous number of several *millions* of computational cells. Although the computational costs related to the auxiliary cells are minimal compared to the main mesh cells, an effort is made to minimize their number.

One optimization is to generate the mesh only in the absorption area. Following the notation of section 2.1, the minimal value of z_{min} given by (30) is determined on the whole 2D mesh in terms of cell indices and then the main mesh is "cut" along the minimal index. The mesh generator then operates on a mesh with a decreased number of the cells.

Another improvement of the algorithm is reduction of the number of cells in a corona. Unlike the previous technique, this one is performed within the 1D SME laser absorption algorithm itself. The cells of the auxiliary mesh are checked from the top, whether they satisfy the sampling condition (35). The procedure lowers the upper limit of the absorption area z_{max}, until the first cell satisfying the condition is reached. Provided that the real part of refraction index n is approximately monotone along the z axis as well as the sizes of computational cells, a continuous domain is obtained by

the process. It must be noted that the reflection coefficient V is not calculated on the new boundary from the Fresnel equations with vacuum on the top side, but rather the reflection coefficient is set $V = 1$, because the corona is continuing there in fact. This is a reasonable condition and the transition between the vacuum condition and this one is negligible, because the quantities are only slowly varying at the end of the corona and the refraction index is naturally close to $\hat{n} \approx 1$.

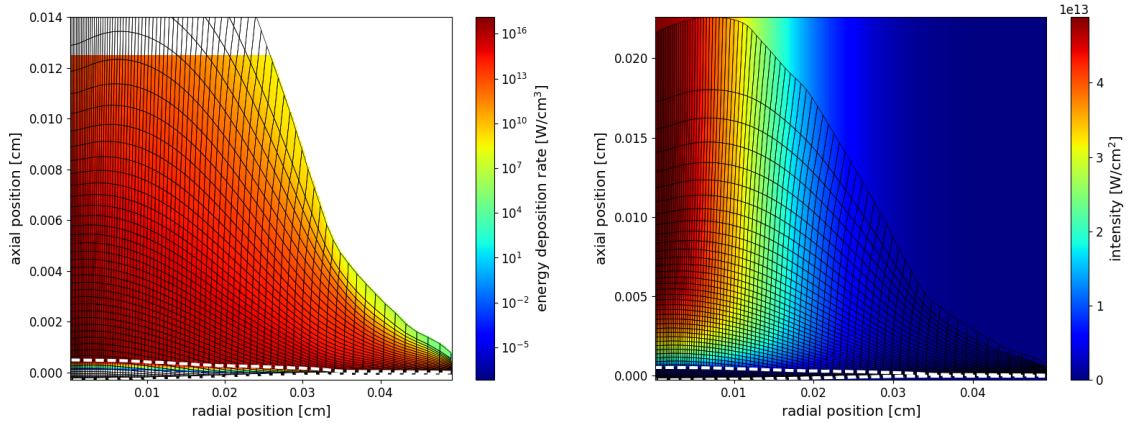

Figure 6: Detail of divergence of the Poynting vector and full image of laser intensity computed by the algorithm on the refined computational mesh with $\approx 3 \cdot 10^6$ cells (the refinement factors are 10 in axial and 5 in radial direction). The plot is taken from the 2D simulation performed in section 6 at time $t = 300$ ps. The Lagrangian mesh is outlined by the black lines and also the critical plane highlighted by the white dashed line.

The main difference between the piecewise bilinear and constant version of the algorithm is that the bilinear interpolation method uses the *dual mesh*, i.e. the mesh composed of cell centres of the main mesh. The reason for this is that the interpolation method is supposed to be consistent with the original functions at the cell centres (or rather cell centroids, i.e. geometrical centres). Hence, there appears another difficulty, because the upper boundary in the simulation is formed by the top nodes and edges of the main mesh. In order to follow exactly identical boundary, an additional layer of cells must be added to the dual mesh.

After the generation of the mesh, the algorithm proceeds similarly to the original version described in the previous work [13]. Parallelization of the code is beneficial even in this case, utilizing several processor cores for computation of the intersections of the main and the auxiliary cells. In addition to the computation of the volumes of the created intersections, there is incorporated another step in the algorithm, that calculates the centroids of the intersections. The procedure is very similar to the computation of the volumes $\|V^\wedge\| = \int_{V^\wedge} 1 \,\mathrm{d}x \,\mathrm{d}y$ of the intersections (in Cartesian coordinates x, y and analogously in cylindrical coordinates), but integrals $\int_{V^\wedge} x \,\mathrm{d}x \,\mathrm{d}y$ and $\int_{V^\wedge} y \,\mathrm{d}x \,\mathrm{d}y$ are calculated instead. The integrals are additive in the integration domain and thus contributions of all parts of the decomposed intersection area into primitives are summed together similarly to the volumes and the centroids

$\vec{x}_c^{\wedge} = (x_c^{\wedge}, y_c^{\wedge}) = (\int_{V^{\wedge}} x \,\mathrm{d}x\,\mathrm{d}y / \int_{V^{\wedge}} 1 \,\mathrm{d}x\,\mathrm{d}y, \int_{V^{\wedge}} y \,\mathrm{d}x\,\mathrm{d}y / \int_{V^{\wedge}} 1 \,\mathrm{d}x\,\mathrm{d}y)$ are obtained. Due to simplicity and similarity with the computation of the volumes, the full procedure is not detailed here.

The main difference of both methods resides in the interpolation and the mapping of the quantities. In the case of the piecewise constant interpolation, the values of mapped quantities on the intersections of the main and auxiliary mesh are directly determined by the value on the main mesh cell, in which the intersection is located. However, the situation is more complicated for the bilinear interpolation. The interpolated function on the main mesh $f = f(\vec{x})$ is projected onto each of the intersections $V^{\wedge}$ by the point value at its centroid $\vec{x}_c^{\wedge}$. This projection is close to the mean value projection and both are identical for linear functions (f' denotes the first derivative, provided that it exists on $V^{\wedge}$):

$$\int_{V^{\wedge}} f(\vec{x}) \,\mathrm{d}\vec{x} \approx \int_{V^{\wedge}} f(\vec{x}_c) + f'(\vec{x}_c)(\vec{x} - \vec{x}_c) \,\mathrm{d}\vec{x} = \\ = (f(\vec{x}_c) - f'(\vec{x}_c)\vec{x}_c)\left\|V^{\wedge}\right\| + f'(\vec{x}_c) \int_{V^{\wedge}} \vec{x} \,\mathrm{d}\vec{x} = f(\vec{x}_c)\left\|V^{\wedge}\right\| \ . \quad (44)$$

Hence, the projection is in a good agreement with the bilinear interpolation, that degenerates into a linear interpolation along each of the edges of the cell. Since the gradients of mapped quantities usually correlate with the shape of the Lagrangian mesh and also taking into account that the auxiliary cells are several times smaller than the cells of the dual mesh, the projection is highly accurate even in the interior of the cells with respect to integral values.

In order to evaluate $f(\vec{x}_c^{\wedge})$, the vector in parametric space of bilinear planes $(\vec{\alpha}, \vec{\beta})$ ($\vec{\alpha} = (\alpha_0, \alpha_1, \alpha_2, \alpha_3)^T$, $\vec{\beta} = (\beta_0, \beta_1, \beta_2, \beta_3)^T$) is determined at the beginning of the mapping. The area of the cell can be described using logical coordinates (ζ, η), $\zeta, \eta \in \langle 0, 1 \rangle$ as:

$$x = \alpha_0 + \alpha_1\zeta + \alpha_2\eta + \alpha_3\zeta\eta \ , \quad (45)$$

$$y = \beta_0 + \beta_1\zeta + \beta_2\eta + \beta_3\zeta\eta \ . \quad (46)$$

Ordering the nodes $\vec{x}_0, \vec{x}_1, \vec{x}_2, \vec{x}_3$ counter-clockwise and requiring that the nodes correspond to the logical coordinates $(0,0), (1,0), (1,1), (0,1)$ respectively, the linear system for the parameters $\vec{\alpha}, \vec{\beta}$ is obtained:

$$\begin{pmatrix} 1 & 0 & 0 & 0 \\ 1 & 1 & 0 & 0 \\ 1 & 1 & 1 & 1 \\ 1 & 0 & 1 & 0 \end{pmatrix} \begin{pmatrix} \alpha_0 & \beta_0 \\ \alpha_1 & \beta_1 \\ \alpha_2 & \beta_2 \\ \alpha_3 & \beta_3 \end{pmatrix} = \begin{pmatrix} \vec{x}_0^T \\ \vec{x}_1^T \\ \vec{x}_2^T \\ \vec{x}_3^T \end{pmatrix} \ . \quad (47)$$

After inverting the system, the parameters are explicitly given as:

$$\begin{pmatrix} 1 & 0 & 0 & 0 \\ -1 & 1 & 0 & 0 \\ -1 & 0 & 0 & 1 \\ 1 & -1 & 1 & -1 \end{pmatrix} \begin{pmatrix} \vec{x}_0^T \\ \vec{x}_1^T \\ \vec{x}_2^T \\ \vec{x}_3^T \end{pmatrix} = \begin{pmatrix} \alpha_0 & \beta_0 \\ \alpha_1 & \beta_1 \\ \alpha_2 & \beta_2 \\ \alpha_3 & \beta_3 \end{pmatrix} . \tag{48}$$

When the plane is parametrized, points (x, y) can be transformed to logical coordinates (ζ, η). The system (45), (46) is formally rewritten into the more convenient form:

$$\begin{pmatrix} \alpha_1 & \alpha_2 \\ \beta_1 & \beta_2 \end{pmatrix} \begin{pmatrix} \zeta \\ \eta \end{pmatrix} = \begin{pmatrix} x - \alpha_0 - \alpha_3\zeta\eta \\ y - \beta_0 - \beta_3\zeta\eta \end{pmatrix} . \tag{49}$$

The quadratic system can degenerate into many distinct forms and not all cases are discussed here for brevity of the text, but one can find broader analysis for example in [29]. The most important division is whether the coefficients α_3 or β_3 are zero. When both coefficients are zero, then the system becomes purely linear. It must be noted that an appropriate tolerance in this condition is used due to finite precision of computation. If only one of the coefficients is (near-)zero, then there is only one quadratic equation and the next step is skipped. In the most general case, both coefficients are non-zero and the system is reduced as follows:

$$\begin{pmatrix} \alpha_1\beta_3 - \beta_1\alpha_3 & \alpha_2\beta_3 - \beta_2\alpha_3 \\ \alpha_1\beta_3 + \beta_1\alpha_3 & \alpha_2\beta_3 + \beta_2\alpha_3 \end{pmatrix} \begin{pmatrix} \zeta \\ \eta \end{pmatrix} = \begin{pmatrix} (x - \alpha_0)\beta_3 - (y - \beta_0)\alpha_3 \\ (x - \alpha_0)\beta_3 + (y - \beta_0)\alpha_3 - 2\alpha_3\beta_3\zeta\eta \end{pmatrix} . \tag{50}$$

This system is formed of only one quadratic equation and one linear equation and it is symmetrical in $\vec{\alpha}$, $\vec{\beta}$. The notation is united with the degenerated form, where α_3 or β_3 was (near-)zero, by assigning the elements on the left hand side to $a_{11} \ldots a_{22}$, constant terms on the right hand side to b_1, b_2 and the quadratic coefficient to d. Relative positions are $\bar{x} = x - \alpha_0$ and $\bar{y} = y - \beta_0$.

Assuming that the linear part of the system (50) has a solution, the substitution into the quadratic equation is made and the quadratic equation for ζ or η is obtained:

$$(-a_{11}d)\zeta^2 + (+a_{21}a_{12} - a_{22}a_{11} + db_1)\zeta + (a_{22}b_1 - a_{12}b_2) = 0 , \tag{51}$$
$$(-a_{12}d)\eta^2 + (-a_{21}a_{12} + a_{22}a_{11} + db_1)\eta + (a_{21}b_1 - a_{11}b_2) = 0 . \tag{52}$$

In this form, the determinant of the matrix of the left hand side of (50) appears in the central part. This is unfortunate, because nearly degenerated systems have small values of β_3 or α_3 and consequently d. Hence, the equations is rewritten as:

$$(-\alpha_1\beta_3 + \beta_1\alpha_3)\zeta^2 + (-\alpha_1\beta_2 + \alpha_2\beta_1 + \bar{x}\beta_3 - \bar{y}\alpha_3)\zeta + (\bar{x}\beta_2 - \bar{y}\alpha_2) = 0 , \tag{53}$$
$$(-\alpha_2\beta_3 + \beta_2\alpha_3)\eta^2 + (+\alpha_1\beta_2 - \alpha_2\beta_1 + \bar{x}\beta_3 - \bar{y}\alpha_3)\eta + (\bar{x}\beta_1 - \bar{y}\alpha_1) = 0 . \tag{54}$$

One may observe that these equations hold even in the degenerated cases, where β_3 or α_3 are (near-)zero, and only the determinant of the original system (49) appears in the central part. One of the quadratic equations is then solved and the value of the other variable is obtained from the linear equation. Both procedures are mathematically equivalent, but the quadratic equation with larger discriminant is preferred numerically.

Also solution of a given quadratic equation must be treated carefully from the numerical point of view. The coordinate system within this procedure is translated to (α_0, β_0), normalized to (α_1, β_2) and rotated by 45 degrees in order to minimize the number of degenerated cases, because the Lagrangian mesh is very often close to a rectangular mesh. *Vieta's formulas* are used to calculate one of the roots [30] and also *Newton's method* is eventually employed to increase the precision of the found root.

When the logical coordinates (ζ, η) has been calculated, the values of the interpolated function $f = f(x, y) = \bar{f}(\zeta, \eta)$ are given as follows [18]:

$$\bar{f}(\zeta, \eta) = f_0(1-\zeta)(1-\eta) + f_1\zeta(1-\eta) + f_2\zeta\eta + f_3(1-\zeta)\eta \ , \tag{55}$$

where the values $f_0 \dots f_3$ are the known values at the nodes $\vec{x}_0 \dots \vec{x}_3$.

The final values of the mapped quantities in the auxiliary cells are then calculated as the volume-weighted average of all values inside the intersections with the dual mesh. The inverse process then uses a weighted average too, but the contribution of given node of the dual mesh to equation (55) are taken into account in addition to the volumes.

2.2.1 Test problem

A test problem was designed to verify the properties of the interpolation methods presented in section 2.2. The function $f^{test}(x, y) = \sin\left(\sqrt{x^2 + y^2}\right)$ is interpolated by the piecewise constant and piecewise bilinear methods on randomly perturbed (maximally half of the inter-node distance) equidistant rectangular meshes with the same number of nodes along each axis $N_x = N_y$. Cartesian geometry was used in both cases and the automatically generated auxiliary mesh had the ratio of the number of cells to the number of cells of the main mesh N^r along each axis. The original rectangular mesh was $\langle 0, 5\pi/4\rangle \times \langle 0, 5\pi/4\rangle$. An example is depicted in Figure 7. The grid functions on the main mesh were obtained by point projection at the centroids of respective cells.

In order to estimate the error of the interpolation, discrete L_1 and L_2 errors were calculated from the discrepancies of the values of the interpolated function $f(x, y)$ and the analytical function $f^{test}(x, y)$ at the centroids $(x_c^{a_{jl}}, y_c^{a_{jl}})$ of the auxiliary cells a_{jl} with the volumes $\|V^{a_{jl}}\|$:

$$\left\|f^{test} - f\right\|_{L_1}^{a} = \sum_{jl} \left| f^{test}(x_c^{a_{jl}}, y_c^{a_{jl}}) - f(x_c^{a_{jl}}, y_c^{a_{jl}}) \right| \|V^{a_{jl}}\| \ , \tag{56}$$

$$\left\|f^{test} - f\right\|_{L_2}^{a} = \sqrt{\sum_{jl} \left| f^{test}(x_c^{a_{jl}}, y_c^{a_{jl}}) - f(x_c^{a_{jl}}, y_c^{a_{jl}}) \right|^2 \|V^{a_{jl}}\|} \ . \tag{57}$$

Series of numerical experiments were performed comparing the interpolation

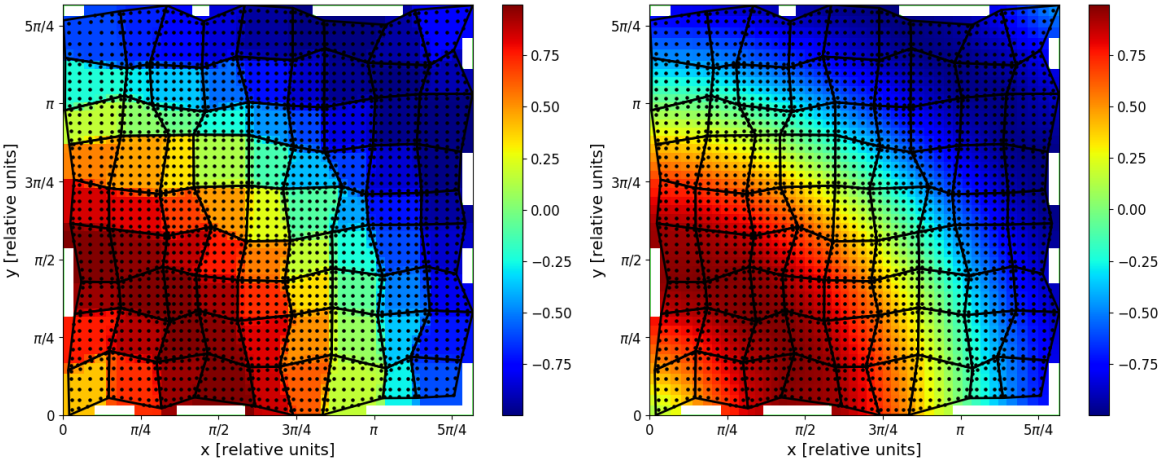

Figure 7: Interpolated function $\sin\left(\sqrt{x^2+y^2}\right)$ on randomly perturbed rectangular mesh with the number of nodes $N_x = N_y = 10$. The piecewise constant interpolation method was used on the left and the piecewise bilinear interpolation method is on the right. The main mesh is plotted by a full line and centroids of the intersections with the auxiliary mesh are represented by points. The ratio of the number of auxiliary cells to the main cells was $N^r = 5$ in both axes.

methods, where the number of nodes of the main mesh varied and also different values of the ratio N^r were used. The resulting L_1 and L_2 errors are plotted in Figure 8 and Figure 9 respectively. In order to obtain each of the points, 10 randomly perturbed main meshes were generated and the mean values are taken. The standard deviation was at least one order of magnitude lower than the nominal value in all cases.

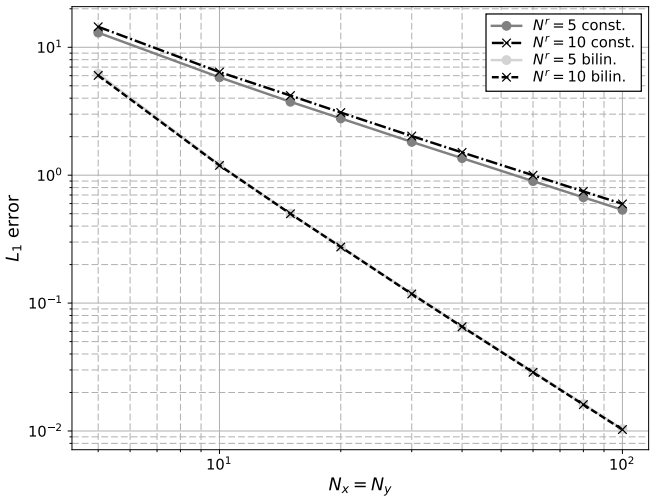

Figure 8: L_1 error of the interpolation methods (*const.* – piecewise constant, *bilin.* – piecewise bilinear) in the test problem versus the number of nodes of the main computational mesh along each axis $N_x = N_y$. The ratio of the number of auxiliary cells to the number of cells of the main mesh along each axis is denoted as N^r.

The results show superiority of the piecewise bilinear method compared to the piecewise constant interpolation method. The piecewise constant interpolation achieves only the first order convergence in L_1 norm and approximately one half in L_2 norm, but it must be noted that the total number of cells of the main mesh is $N_c = (N_x-1)(N_y-1)$ and this method cannot utilize them effectively. The spatial analysis of the errors reveals that the errors are approximately increasing toward the symmetry axis of the first quadrant as can be predicted, because the sizes of the cells along the gradient of the function f^{test} effectively increases and the method losses the accuracy rapidly. On the other hand, the piecewise bilinear interpolation reaches the second order of convergence in L_1 and also L_2 errors. Moreover, the absolute values of errors are lower in all cases compared to the piecewise constant interpolation and also the spatial distribution of the errors is more homogeneous.

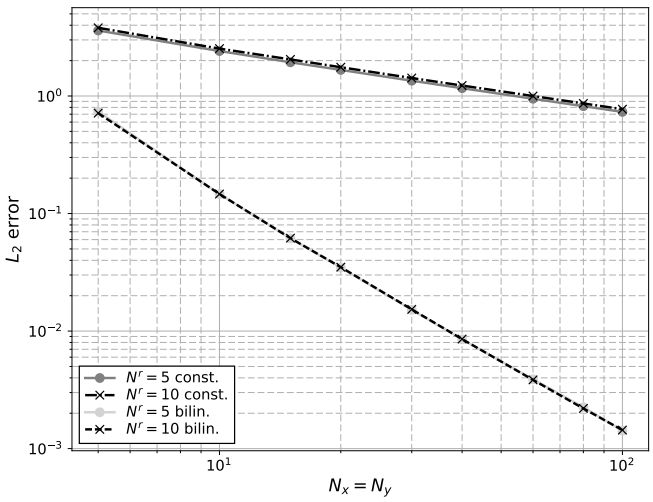

Figure 9: L_2 error of the interpolation methods (*const.* – piecewise constant, *bilin.* – piecewise bilinear) in the test problem versus the number of nodes of the main computational mesh along each axis $N_x = N_y$. The ratio of the number of auxiliary cells to the number of cells of the main mesh along each axis is denoted as N^r.

3 Physical closure

The physical closure is a necessary part of the simulation code. In the case of hydrodynamical simulations, it includes the equation of state that provides enclosing relations for the conservation laws (1), (2), (5), (6) in order to obtain self-consistent model that can be solved numerically. It relates thermodynamic state variables with appropriate potentials and other derived quantities. The primary quantity of the interest here is the pressure that appears in the equation of momentum (2) and energy (3), (4). Also heat capacities are of a great importance for the temperature based models in section 4, 5. Used equations of state are shortly described in section 3.1.

Another part of the closure model are relations for the transport coefficients and temperature relaxation coefficients as well as other quantities derived from collision frequency. We prefer a global model of ion and electron collision frequencies most of the time, that are then consistently used for the calculation of the previously mentioned coefficients. The model of electron collision frequency is presented in section 3.2. Later, the relations for electron–ion exchange coefficients are introduced in section 3.3. Heat conductivity coefficient is then derived in 3.4 for electrons. The extinction coefficient of electrons used in the non-local transport model (see section 5) are presented in section 3.5. Similarly, description of ion collision frequency is given in section 3.6 and it is followed by inference of ion heat conductivity coefficient in section 3.7. Finally, the extinction coefficient of ions are presented in section 3.8.

3.1 Equations of state

In the simulation code PALE2, there are four different equations of state available, ideal gas, SESAME, QEOS and BADGER. Simulation code PETE is designed similarly, providing SESAME, BADGER and eventually FEOS equations of state.

SESAME is a representative of tabulated equations of state. It in fact consists of vast number of discrete data points obtained experimentally in the *Los Alamos National Laboratory*[31, 32, 33]. These values are then interpolated in temperatures and densities.

The quotidian equation of state (QEOS) is historically one of the most popular analytical models used for hydrodynamic simulations. Conceptually, the equation of state consists of three parts integrated into the single model by the expression for *Helmholtz free energy* [34]:

$$F_{tot}(\rho, T_e, T_i) = F_i(\rho, T_i) + F_e(\rho, T_e) + F_b(\rho, T_e) \tag{58}$$

The electron contribution F_e is primarily based on the *Thomas–Fermi theory* for electrons [35]. The term F_b represents the semi-empirical bonding corrections [36] that effectively lower the total pressure at solid densities and give correct values of bulk modulus. The ion fluid represented by F_i term is described by liquid and solid scaling laws and by the Cowan model [37].

Later, the model was implemented in the library MPQeos [38]. It was then further extended in FEOS package, where proper treatment of mixtures has been added, cold

curve has been improved and also liquid–vapour phase coexistence area is calculated rigorously [39].

Finally, BADGER is a feature rich library offering various models for construction of the equation of state [40]. The ion equation of state is based on QEOS, but scaled binding energies (SBE) model is used instead of the empirical fitting constants. Electron ionization model has been separated from the electron equation of state in the library and three different models are available. The classical Thomas–Fermi model is one of the options, where electrons are treated as a continuum surrounding a nucleus. In contrast, there are also Screened Hydrogenic with l-splitting (SHM) and also individual electron accounting (IEM) models, that treat electrons discretely as a part of the quantum system of atom. The electron equation of state takes into account free electrons as well as bound electrons, which are classically neglected. Coulomb interaction and charge screening are then calculated between all species.

In practice, the equations of state are tabulated and interpolated to accelerate the computation [41]. Although QEOS, BADGER and FEOS are analytical models, direct calculations are computationally demanding, especially in 2D.

3.2 Electron collision frequency

Collision frequencies are one of the most important parts of the closure of the numerical scheme. Electron–ion collision frequency first appeared in the definition of $\hat{\varepsilon}$ (16), that is a cornerstone of the laser absorption model. Later in section 3.4, it also determines the *diffusion coefficients* for the heat diffusion scheme introduced in section 4. Likewise, it governs the *electron–ion energy exchange rate coefficients* presented in section 3.3, which effectively drive heating of ions during the ablation process. However, notion of *momentum loss collision frequency* and *energy loss collision frequency* must be distinguished. The first one describes momentum transfer during scattering of particles and the latter one models transfer of energy along the trajectory of a given particle. In order to clarify the description, quantities related to energy transfer are denoted by ϵ in upper index in following sections.

For purposes of the hydrodynamical scheme, a global model of collision frequency is needed. It must cover wide range of temperatures from room temperature to approximately $\sim$ 10keV. Moreover, densities ranging from a solid to a corona must be included. In the limit of ideal plasma, classical *Spitzer–Härm* approximation of electron–ion momentum loss collision frequency holds [14]:

$$\nu_{SH} = \frac{4}{3}\sqrt{2\pi}\frac{Z\ e^4 m_e n_e}{(m_e k_B T_e)^{3/2}} \ln\Lambda\ , \tag{59}$$

where $\ln\Lambda$ symbolically represents *Coulomb logarithm*. Classically defined in plasma as $\ln\Lambda = \ln b_{max}/b_{min}$, the logarithm declines to near-zero values for low temperatures ($\sim$ 10 eV) and the whole theory fails in this area ($b_{max} \approx b_{min}$). In order to prevent this behaviour and provide at least partially physically relevant predictions, Coulomb logarithm has been extended in work of *Lee and More* [42]. The modified form of the

Coulomb logarithm can be written as follows:

$$\ln\Lambda = \max(2, \ln\sqrt{1+(b_{max}/b_{min})^2}) \ , \tag{60}$$

$$b_{max} = \frac{\sqrt{k_B T/m_e}}{\max(\omega_{pe}, \omega_0)} \ , \tag{61}$$

$$b_{min} = \max\left(\frac{Ze^2}{k_B T}, \frac{\hbar}{\sqrt{m_e k_B T}}\right) \ . \tag{62}$$

The maximum impact parameter b_{max} is derived from the Debye screening length v_{Te}/ω_{pe} including the effect of high frequency laser EM field $\omega_0 \gtrsim \omega_{pe}$, where $v_{Te} = \sqrt{kT_e/m_e}$ is thermal velocity of electrons. Minimal impact parameter b_{min} originates from the larger of the classical normal angle deflection limit or de Broglie wavelength $\hbar/(m_e v_{Te})$.

In the case of momentum transfer, collision frequency is usually dominated by electron–ion collisions, especially for high-Z materials. This can be read from a linear Z-dependence of ν_{SH} (59). The electron–electron momentum loss collision frequency is approximated for high temperatures by the formula (in CGS units with temperatures in eV)[43]:

$$\nu_{el\text{-}el} = 7.7 \cdot 10^{-6} \frac{n_e}{T_e^{3/2}} \ln\Lambda_{ee} \quad [s^{-1}] \ , \tag{63}$$

with Coulomb logarithm for electron–electron collisions given as:

$$\ln\Lambda_{ee} = \max\left(10, 23.5 - \ln(n_e^{1/2} T_e^{-5/4}) - (10^{-5} + (\ln T_e - 2)^2/16)^{1/2}\right) \ . \tag{64}$$

Unlike electron–ion collision frequency (59), there is no additional dependence on Z in (63).

Collisions between electrons are then well approximated in the model by the correction factor $g(Z)$ [44]:

$$\tilde{\nu}_{SH} = g(Z)\nu_{SH} = \frac{1.0 + 0.24Z}{0.24(Z + 0.24)} \nu_{SH} \ . \tag{65}$$

The modified collision frequency $\tilde{\nu}_{SH}$ then approaches for high temperatures approximately the sum of ν_{SH} and $\nu_{el\text{-}el}$ as can be noticed in Figure 10. The difference of both functions for low temperatures is mainly caused by the different Coulomb logarithms for electron–ion and electron–electron collisions.

Electron–electron collisions are contributing even for cold material, where the dependence $\sim T_e^2$ is known, but these effects are mainly of the interest for ultra-short laser pulses [45], because electron–phonon interaction (described below) prevails for higher temperatures [46].

For temperatures approximately under *Fermi temperature* that is defined as $T_F = (3\pi^2 n_e \hbar^3)^{2/3}/(2m_e k_B)$, plasma no longer consists of free electrons and electron degeneracy must be taken into account. Typical values of Fermi temperature are about $\sim 1 - 10$ eV for metals and the value is 11.7 eV for Aluminium for example [47]. Moreover, electron–phonon interaction is participating, when ion temperature is under the

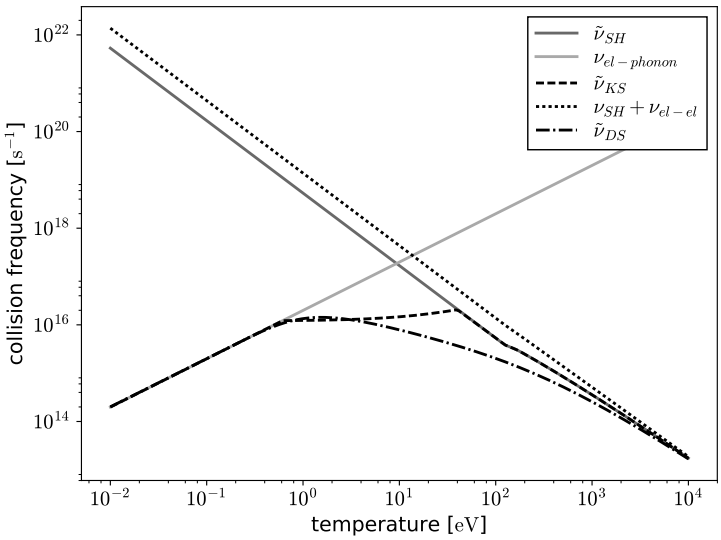

Figure 10: Momentum loss collision frequency as function of temperature ($T = T_e = T_i$) obtained from different models. Aluminium with density of solid ($\varrho = 2.7$ g/cm^3) is considered with mean ionization $Z = 2.5$. The fitting constants are taken from section 3.4.

melting point. Electrons are being scattered by phonons, i.e. lattice vibrations quanta. According to [22], collision frequency in the limit of a cold solid is:

$$\nu_{el\text{-}phonon} = 2k_S \frac{e^2 k_B T_i}{\hbar^2 v_F} \ , \tag{66}$$

where v_F denotes Fermi velocity $v_F = \hbar \sqrt[3]{3\pi^2 n_e}/m_e$. The multiplicative empirical constant k_S allows adapting the model to experimental data (see below). It should be also noted that the linear dependency of the collision frequency on temperature for low temperatures is macroscopically meaningful, because it results in a constant thermal conductivity coefficient as it is shown in section 3.4.

The previous two collisional frequencies ν_{SH} and $\nu_{el\text{-}phonon}$, both valid for different range of temperatures, are then interpolated on the whole range by a harmonic mean:

$$\nu_{KS}^{-1} = \nu_{SH}^{-1} + \nu_{el\text{-}phonon}^{-1} \ . \tag{67}$$

One may observe that the model maintains the same limits (see Figure 11), because $\nu_{el\text{-}phonon}$ diverges for high temperatures and thus ν_{SH} dominates and vice versa. However, the model overestimates collision frequencies for intermediate temperatures. This issue has been addressed in [22] by a plausible criterion:

$$\nu_{KS} < v_e/r_0 = v_e \left(\frac{3}{4} \pi n_i \right)^{1/3} \ , \tag{68}$$

where $v_e = \sqrt{v_F^2 + k_B T_e/m_e}$ is the characteristic velocity of electrons, which approaches Fermi velocity v_F for low temperatures and thermal velocity $k_B T_e/m_e$ in a hot plasma. The expression (68) states essentially that the mean free path given by v_e/ν_{KS} is not allowed to be shorter than the typical inter-atomic distance in the medium r_0. The resulting model as well as the criterion are depicted in Figure 11.

Only electron–ion or electron–phonon interactions were considered for laser absorption by Inverse Bremsstrahlung in section 2. However, electron–electron correction can be applied for the purposes of heat conduction by using $\tilde{\nu}_{SH}$ (65) instead of ν_{SH} in the definition of ν_{KS} (67). The modified collision frequency is denoted by $\tilde{\nu}_{KS}$. The application of the criterion (68) then can be justified by the fact that the classical theory of elastic electron–electron collisions does not hold for the region of temperatures near the Fermi temperature.

In order to obtain the value of k_S mainly for optical purposes, one can utilise bulk reflectivity of the material. Reflectivity coefficient (for normal incidence) is given by:

$$R = \left| \frac{\hat{n} - 1}{\hat{n} + 1} \right|^2 \quad . \tag{69}$$

The complex refraction index $\hat{n}$ is evaluated from (16). This procedure brings for example the value $k_S = 9.4$ for Aluminium in the visible range [22]. For comparison, the value for Copper is $k_S \doteq 435$ with the parameters $\lambda_0 = 2\pi c/\omega_0 = 0.266$ μm, $Z = 4.4,\ A = 63.5,\ \varrho = 8.94$ g/cm^3, $R = 0.34,\ T = 0.0258$ eV [48, 47].

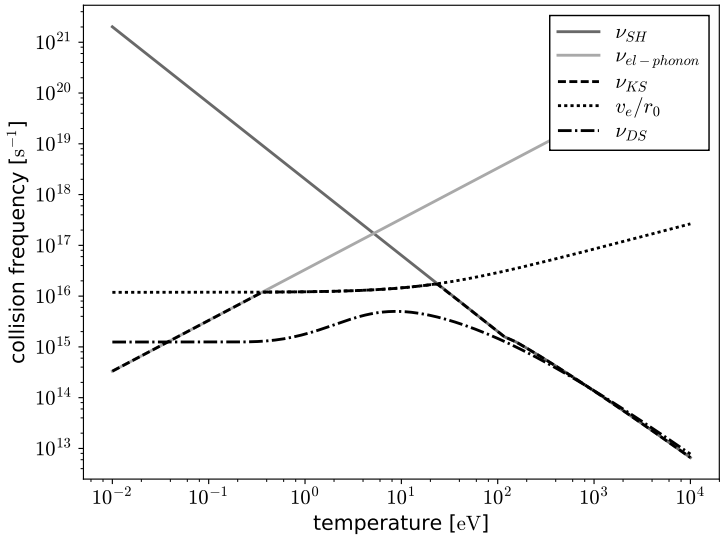

Figure 11: Collisional frequency as function of temperature ($T = T_e = T_i$) obtained from different models. Aluminium with density of solid ($\varrho = 2.7$ g/cm^3) is considered with mean ionization $Z = 2.5$ and wavelength of the laser irradiation $\lambda_0 = 1.05$ μm.

The preceding paragraph shows that the value of k_S significantly varies for different materials and parameters. Values of a few hundreds are usual, which rises questions

about validity of the model. Another issue is the sharp cut-off by in fact ad hoc criterion or weak dependence on the laser wavelength. These points have been addressed later in the model based on *Drude–Sommerfeld* theory [26, 49]. Ion temperature dependence has been completely removed from the model and ions are assumed to be static. However, the linear dependency on temperature, in this case electron temperature, in solids remains and it is attributed to properly treated electron degeneracy instead of electron–phonon scattering. Modifications to Coulomb scattering are made for slow electrons with velocities v satisfying $Ze^2/(\hbar v) \geq 1$ [50]. The model then allows to properly estimate the collision frequency depending on both, electron temperature T_e and laser wave angular frequency ω_0. Furthermore, the model covers *warm dense matter* (WDM) regime, where $(\hbar v_{Te}/(Ze^2))(m_e v_{Te}^2/(\hbar\omega_0)) = m_e v_{Te}^3/(Ze^2\omega) < 1$ and of course Spitzer regime, where the opposite holds. However, $\hbar\omega_0/(m_e v_{Te}^2) < 1$ holds for most of the time, because only the (near-)visible range laser wavelengths are considered here. The interpolated formula takes the form:

$$\nu_{DS} = 2\sqrt{2\pi}\frac{Ze^4 n_e}{m_e^{1/2}(k_B T_e)^{3/2}} \ln\left(1 + k_{DS}\frac{1.32}{\sqrt{2\pi}}\frac{k_B T_e}{(m_e^{1/2} Ze^2 \max(\omega_0, \omega_{pe}))^{2/3}}\right) F(T_e, \hbar\omega_0) \ . \tag{70}$$

The Fermi factor $F(T_e, \hbar\omega_0)$ is obtained from exact averaging over the *Fermi–Dirac distribution* (denoted by $\langle\cdot\rangle$):

$$F(T_e, \hbar\omega) = \sqrt{\frac{\pi}{2}}\left\langle\frac{v_{Te}}{v}\right\rangle = 3\left(\frac{v_{Te}}{v_F}\right)^3 \ln\left(\frac{1 + \exp\left(\dfrac{\mu}{k_B T_e}\right)}{1 + \exp\left(\dfrac{\mu - \hbar\omega}{k_B T_e}\right)}\right)\frac{1}{1 - \exp\left(-\dfrac{\hbar\omega}{k_B T_e}\right)} \ . \tag{71}$$

The chemical potential μ is approximated by the formula:

$$\frac{\mu}{k_B T_e} = -\frac{3}{2}\ln\Theta + \ln\frac{4}{3\sqrt{\pi}} + \frac{C_A\Theta^{-(C_b+1)} + C_B\Theta^{-(C_b+1)/2}}{1 + C_A\Theta^{-C_b}} \ , \tag{72}$$

where $\Theta = T_e/T_F$ and the constants are $C_A = 0.25054, C_B = 0.072$ and $C_b = 0.858$ [51].

One may prove that the collision frequency approaches the Spitzer–Härm formula for ν_{SH} in the limit of high temperatures ($T_e \to \infty$). This is also clearly visible in Figure 11. On the other hand, it violates the linear dependency on temperature in cold solids that we intended to maintain. This is however only the case of high frequency laser field and the collision frequency that appears in the permittivity $\hat{\varepsilon}$ according to (16). When slow transport phenomena are considered like heat diffusion, substituted frequency is set $\omega_0 = 0$ and the linear dependency is restored again (see Figure 12). This is implied by *Pauli blocking* incorporated by the term $F(T_e, \hbar\omega_0)$ that effectively lowers the number of electrons available for scattering in highly degenerate plasma.

We also introduce electron–electron correction of heat conduction by the factor

$g(Z)$ similarly to (65):

$$\tilde{\nu}_{DS} = 2\sqrt{2\pi} g(Z) \frac{Ze^4 n_e}{m_e^{1/2}(k_B T_e)^{3/2}} \ln\left(1 + \frac{k_{DS}}{g(Z)} \frac{1.32}{\sqrt{2\pi}} \frac{k_B T_e}{(m_e^{1/2} Ze^2 \max(\omega_0, \omega_{pe}))^{2/3}}\right) F(T_e, \hbar\omega_0) \,. \tag{73}$$

It does not alter the linear regime for low temperatures and only Spitzer regime is affected. Unlike $\tilde{\nu}_{KS}$, the transition between the region of intermediate temperatures and Spitzer regime is smooth, but even the range between $\approx 100 \div 1000$ eV is slightly deviated from $\tilde{\nu}_{SH}$. This consequently impacts temperature profiles in corona for low intensity lasers as it has been observed in section 6.

Constant k_{DS} appearing in (70) is purely empirical and it serves for fitting the model to experimental data. The same procedure used for estimating the value of k_S can be utilised here, but the recommended value $k_{DS} = 1$ by the authors is usually sufficient, because of the robustness of the model. It can be observed in Figure 11 that the ν_{DS} curve crosses the ν_{KS} curve near the room temperature and thus it gives similar values of reflectivity coefficient there.

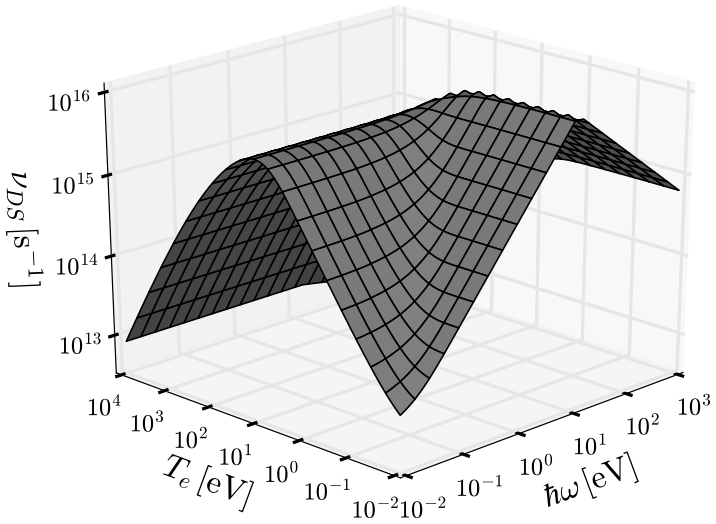

Figure 12: Drude–Sommerfeld collision frequency model plotted as a function of electron temperature T_e and photon energy $\hbar\omega$. Aluminium with density of solid ($\varrho = 2.7$ g/cm^3) is considered with mean ionization $Z = 2.5$

Different situation can occur for other metals, which deviate from the underlying *free electron model*. Empirical correction is then suggested by [52] in (71). There is an extra factor appearing in front of $\hbar\omega/(k_B T_e)$ that will be denoted as C_{DS}^1. By comparison with experimental data, the paper proves that the appropriate value for Gold is $C_{DS}^1 = 5$. Other verified values are not known to us and we preferred original

value $C_{DS}^1 = 1$, since the effect of this constant for nanosecond laser pulses is usually negligible.

Another factor C_{DS}^2 will be introduced later in the section about heat conductivity coefficient 3.4. The constant multiplies the dimensionless factor Θ. This modification can be seen as a correction of the model for chemical potential μ (72) that cannot cover wide range of materials without any corrections. It must be noted that none of the corrections alter the investigated limit cases of the collision frequency model, i.e. linearity of dependence of ν_{DS} on temperature for a cold solid and the Spitzer regime for a hot plasma.

Simulation code PETE has been designed modularly, so it allows switching of various collision frequency models. However, presented results for PALE2 use well-established model ν_{KS} for laser absorption and heat diffusion or classical Spitzer–Härm model $\tilde{\nu}_{SH}$ limited for low temperatures is used for heat diffusion instead. Therefore, a comparison of results achieved with different collision frequency models is given in section 6 for the simulation code PETE.

3.3 Energy exchange coefficients

The energy exchange coefficients G_{ei} and G_{ie} are used in section 4 for electron–ion temperature relaxation mechanism. The coefficients are defined as follows:

$$G_{ei} = \rho \left(\frac{\partial \varepsilon_e}{\partial T_e} \right)_\rho \nu_{ei}^\epsilon \ , \tag{74}$$

$$G_{ie} = \rho \left(\frac{\partial \varepsilon_i}{\partial T_i} \right)_\rho \nu_{ie}^\epsilon \ , \tag{75}$$

where ν_{ei}^ϵ and ν_{ie}^ϵ are electron–ion and ion–electron energy loss collision frequency respectively. In order follow the philosophy of a single global collision frequency model, these collision frequencies are derived from the electron–ion momentum loss collision frequency by the formula [22]:

$$\nu_{ie}^\epsilon / Z = \nu_{ei}^\epsilon = \frac{2m_e}{m_i} \nu_{ei} = \frac{2m_e}{A m_u} \nu_{ei} \ . \tag{76}$$

The electron–ion momentum loss collision frequency ν_{ei} is then taken from one the models presented in section 3.2, i.e. ν_{SH}, ν_{KS} or ν_{DS}. The introduced factor $2m_e/m_i$ originates from mechanics of the collisions, where energy transfer between the species is highly ineffective due to their significantly different masses. This phenomena leads to almost independent equilibration of electrons and ions assuming that $\nu_{ei}^\epsilon \ll \nu_{ee}^\epsilon \approx \nu_{ee}$. This justifies the construction of the computational scheme, because assumption ${\nu_{ei}^\epsilon}^{-1} \gg \Delta t \gg {\nu_{ee}^\epsilon}^{-1}$ is supposed to hold for hydrodynamical simulations, where Δt is a typical time length of a computational step. Hence, single species are assumed to be in local thermal equilibrium (LTE), but two-temperature model is used, where electrons and ions have separate temperatures.

The fitting constants for the models of collision frequency are obtained from the

characteristic cold ion heating time $\tau_i = m_i/(2m_e\nu_{ei})$. This constant can be determined experimentally from pump-probe experiments and it has usually values about ~ 10 ps. For example, it has value $\tau_i \approx 20$ ps for Aluminium [22].

Total energy conservativity of electron and ion energy equations (5), (6) enforces the symmetrical form of the energy exchange terms and of the coefficients as well, i.e. $G_{ei} = G_{ie}$. Unfortunately, this symmetry is not fulfilled when a general equation of state is used for calculation of the specific heats $(\partial\varepsilon_e/\partial T_e)_\rho$ and $(\partial\varepsilon_i/\partial T_i)_\rho$. Therefore, ideal gas definitions are taken instead:

$$G_{ei} = \frac{Z\rho}{Am_u}k_B\nu^\epsilon_{ei} = \frac{2Z\rho}{(Am_u)^2}m_e k_B\nu_{ei} = \frac{\rho}{Am_u}k_B\nu^\epsilon_{ie} = G_{ie}\ . \tag{77}$$

These relations then satisfy the symmetry condition of the exchange coefficients for any electron–ion momentum loss collision frequency model. However, the model is very approximative, but since we are interested mainly into nanosecond laser pulses, an exact description of electron–ion coupling is not needed for the initial phases of the simulation as show the results in section 6.

3.4 Electron heat conductivity coefficient

Electronic heat diffusion must be enclosed by a proper model of heat conductivity coefficient. We decided to formulate it in a consistent manner using one central model of collision frequency introduced in section 3.2. However, different values of the appropriate fitting constants are taken as described below.

The simplest presented model consists of Spitzer–Härm formula [14] corrected by the electron–electron collisions factor [44] and limited by the heat conductivity coefficient of the cold solid κ_{solid}:

$$\tilde{\kappa}_{SH} = \max(\kappa_{solid}, \kappa_{SH})\ , \tag{78}$$

$$\kappa_{SH} = \kappa_0\frac{n_e k_B^2 T_e}{m_e\tilde{\nu}_{SH}}\ . \tag{79}$$

The constant κ_0 has a weak dependence on ionization and values for different Z were tabulated [53]. However, considering validity of the formula only in the high temperature region, where the plasma is fully ionised, the maximal value $\kappa_0 = 13.6$ is usually taken.

In order to generalise the model for lower temperatures, *Wiedemann–Franz law* is supposed to apply there. It attributes heat conduction in metals to electron transport phenomena giving rise to the relation between heat conductivity coefficient and electrical conductivity: $\kappa \sim \sigma T$. Based on this relation, the same dependence on temperature and collision frequency is obtained as before. Finally, the general formula for heat conductivity coefficient can be written as [9]:

$$\kappa = \kappa_0\frac{n_e k_B^2 T_e}{m_e\tilde{\nu}_e} = \kappa_0\frac{n_e k_B^{3/2}}{\sqrt{m_e}}\tilde{\lambda}_e\sqrt{T_e}\ , \tag{80}$$

where $\tilde{\nu}_e$ is the *total electron momentum loss collision frequency* and $\tilde{\lambda}_e$ denotes the *electron momentum loss mean free path*. The collision frequency $\tilde{\nu}_e$ refers to one of the models introduced in section 3.2, i.e. $\tilde{\nu}_{SH}$, $\tilde{\nu}_{KS}$ or $\tilde{\nu}_{DS}$. The respective heat conduction coefficients are then denoted by the same lower index: κ_{SH}, κ_{KS} or κ_{DS}.

All models of heat conductivity coefficient are plotted in Figure 13. The requirement on consistency of the models with κ_{solid} for low temperatures determines the unknown fitting constants k_{KS} and C^2_{DS}. This condition yields for solid Aluminium with heat conductivity coefficient $\kappa_{solid} = 2.76 \cdot 10^{11}$ erg/s/cm/eV [54] values $k_{KS} = 5.7$ and $C^2_{DS} = 7.12$. Procedure for automated calculation of these constants was directly integrated into the simulation code PETE, where only the value of κ_{solid} is taken as a input parameter. It should be noted that complicated full inversion of the expression for $\tilde{\nu}_{DS}$ (73) is not needed, because the Fermi factor $F(T_e, \hbar\omega = 0)$ given by (71) is approaching a simple dependence $\sim T^{3/2}$ in the limit of low temperatures. The logarithm in (73) can be expanded into a Taylor series in the temperature argument and one finally obtains the dependence $\tilde{\nu}_{DS} \sim T_e$ for low temperatures that can be readily inverted.

The rest of the constants are set $C^1_{DS} = 1$ and $k_{DS} = 1$, because high frequency electrical field is not present here ($\omega_0 = 0$) and consistency with the Spitzer formula (79) is assumed.

It is worth noting that the formula (80) can be simplified significantly for one-temperature model ($T_e = T_i = T$) and the global collision frequency model $\tilde{\nu}_{KS}$ (67). Under these conditions it can be rewritten as:

$$\kappa_{KS} = \max(\kappa_{lim}, \kappa_{solid} + \kappa_{SH}) \ . \tag{81}$$

The symbol κ_{lim} stands for the limiting criterion derived from (68) by substituting into (80):

$$\kappa_{lim} = \kappa_0 \frac{n_e r_0 k_B^2 T}{m_e v_e} \ . \tag{82}$$

The resulting formula is conveniently simple and does not need the determination of fitting constant k_{KS}. It has been also implemented in this form in simulation code PALE2.

All models are compared in Figure 13. The limit of constant heat conductivity coefficient for low temperatures (< 1 eV) can be seen. On the other hand, the models are approaching Spitzer formula (79) for high temperatures (> 100 eV), that states the classical $\sim T_e^{5/2}$ temperature dependence in a hot plasma. The models however differ for intermediate temperatures ($1 \div 100$ eV), where Drude-Sommerfeld model gives smoothest transition between the limiting cases. However, the simplest formula $\tilde{\kappa}_{SH}$ (the maximum of κ_{SH} and κ_{solid} curves) significantly underestimates the values of heat conductivity coefficient in this region compared to the other two models. Since the model based on Drude-Sommerfeld theory was developed specifically for WDM (Warm Dense Matter) regime and verified by measurements on FLASH/DESY [49], it is supposed to be more accurate there. However, ν_{KS} is remarkably close to ν_{DS} for most of the time. Hence, it poses a feasible compromise due to its simplicity.

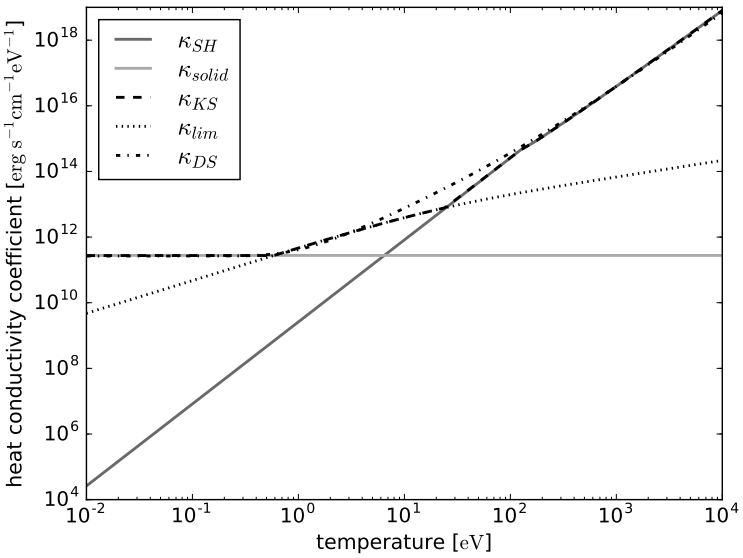

Figure 13: Dependence of heat conductivity coefficient on temperature obtained from different models of total electron collision frequency. Aluminium with density of solid ($\varrho = 2.7$ g/cm^3) is considered with mean ionization $Z = 2.5$.

3.5 Electron extinction coefficients

A crucial parameter for the non-local transport model presented in section 5 is the *electron extinction coefficient* k_e. The coefficient k_e is defined as [9]:

$$k_e^{-1} = \frac{128}{3\pi}\lambda_e^\epsilon \doteq 13.6\lambda_e^\epsilon \ , \tag{83}$$

where λ_e^ϵ refers to *electron energy loss mean free path*. For the purposes of the non-local transport model, it is the characteristic distance travelled by an electron along its trajectory s before it loses its microscopical kinetic energy ϵ_e by collisions with ions:

$$\frac{\mathrm{d}\epsilon_e}{\mathrm{d}s} = -\frac{\epsilon_e}{\lambda_e^\epsilon} \ . \tag{84}$$

Energy loss collision frequency can be approximated for fast electrons by the formula [43] (in CGS units with temperatures in eV):

$$\nu_{NRL}^\epsilon = 4.2 \cdot 10^{-9} \frac{n_i Z^2}{A(\epsilon_e/k_B)^{3/2}} \ln\Lambda \quad [\mathrm{s}^{-1}] \ . \tag{85}$$

Approximating the velocity of electrons by the thermal velocity v_{Te}, final expression for the electron mean free path λ_e^ϵ is obtained:

$$\lambda_e^\epsilon = \frac{v_{Te}}{\nu_{NRL}^\epsilon} = 5.9 \cdot 10^{-9} \frac{A^2 T_e^2}{\rho Z^2 \ln\Lambda} \quad [\mathrm{cm}] \ . \tag{86}$$

Note that ν_{NRL} is almost identical with any of the previous models for energy loss collision frequency ν_{ei}^{ϵ} (76) in Spitzer regime, when thermal energy of electrons was substituted $\epsilon_e = k_B T_e/2$.

Validity of (86) is questionable for lower temperatures ($\lesssim$ 100 eV) as discussed for ν_{SH} (59) before. However, resulting values calculated from (86) for conditions of solid material are of the order $\sim$ Å. Values approximately of the same order are known for the mean free path of low energy electrons in solids [55]. Models for calculation of it from material parameters are also available [56]. Unfortunately, mean free path in solids is strongly dependent on energy of incoming particles. This piece of information is not included in the presented model of non-local transport model in section 5, since only energy intensity of electron flux is used as primary quantity. Only kinetic codes solving the full Vlasov–Fokker–Planck equation are capable of fully determining momentum and energies of transported species [1, 57]. On the other hand, multi-group BGK transport, that can split the energy spectrum into several separate transport groups, poses a feasible solution of this problem and it is one of the possible topics of future research.

3.6 Ion collision frequency

Since non-local transport of ions is considered in the model as well as ion heat diffusion, appropriate models of collision frequencies are introduced in this section.

In order to maintain consistency of *ion–electron momentum loss collision frequency* ν_{ie} with the electron–ion collision frequency models presented in section 3.2, a conversion formula is used. Because total momentum is conserved during the scattering, relation $p_e \nu_{ei} = p_i \nu_{ie}$ must hold, where p_e and p_i are electron and ion momentum respectively. Thus, the conversion factor is obtained assuming quasi-neutrality ($n_e = Z n_i$) in the form:

$$\nu_{ie} = \frac{p_e}{p_i}\nu_{ei} = \frac{n_e m_e}{n_i m_i}\nu_{ei} = Z\frac{m_e}{m_i}\nu_{ei} \ . \tag{87}$$

Another contributing phenomena is the ion–ion scattering and the corresponding *ion–ion momentum loss collision frequency* ν_{ii}. It is approximated for fast ions by [43] (in CGS units with temperatures in eV):

$$\nu_{ii} = 1.8 \cdot 10^{-7} \frac{n_i Z^4}{A^{1/2} T_i^{3/2}} \ln \Lambda_{ii} \quad [\mathrm{s}^{-1}] \ , \tag{88}$$

where the ion–ion Coulomb logarithm $\ln \Lambda_{ii}$ is given by:

$$\ln \Lambda_{ii} = \max\left(10,23 - \ln\left(2\sqrt{2} n_i^{1/2} Z^3 T_i^{-3/2}\right)\right) \ . \tag{89}$$

However, validity of these formulas breaks down for low temperatures and the collision frequency is reaching extreme values. In order to limit the collision frequency

to reasonable values, the plausible criterion similar to one used for ν_{KS} (68) is applied:

$$\nu_{ii} < v_{Ti}/r_0 = v_{Ti}\left(\frac{3}{4}\pi n_i\right)^{1/3}, \tag{90}$$

where $v_{Ti} = \sqrt{k_B T_i/m_i}$ is the ion thermal velocity. It states that collisions cannot occur on distances shorter than the characteristic inter-atomic distance r_0. This crude approximation is justified later by discussion of ion heat conductivity coefficient in section 3.7, where the momentum loss collision frequency ν_{ii} is utilised.

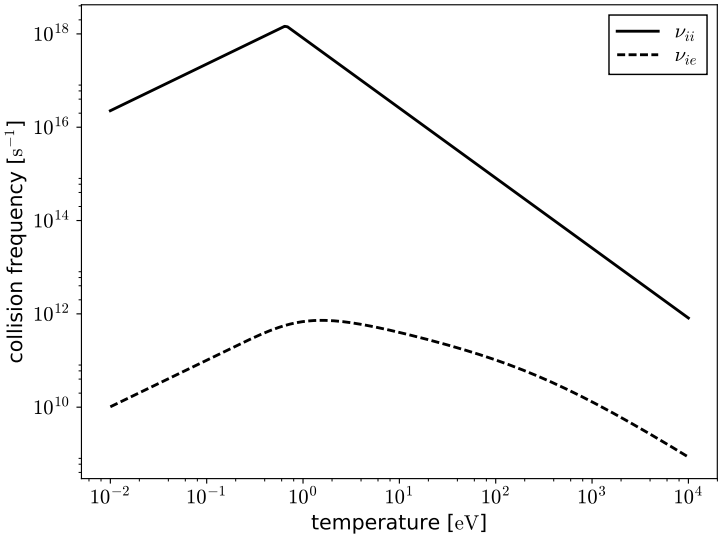

Figure 14: Momentum loss collisional frequency as function of temperature ($T = T_e = T_i$). Aluminium with density of solid ($\varrho = 2.7$ g/cm^3) is considered with mean ionization $Z = 2.5$. Drude–Sommerfeld model was used for calculation of ν_{ie} (see section 3.2).

Both collision frequencies are depicted in Figure 14. It can be concluded that ν_{ii} dominates over ν_{ie} mainly due to strong $\sim Z^4$ dependence in (88). Therefore, ν_{ie} contribution to the *total ion momentum loss collision frequency* $\nu_i = \nu_{ii} + \nu_{ie}$ can be neglected for most of the materials, especially when T_e dependence of ν_{ie} is taken into account (assuming $T_e > T_i$). However, electrons are known to contribute significantly for higher energies of incoming ion species leading to the well-known *Bethe formula* [58]. Unfortunately, the energies of incoming species are not known as discussed in section 3.5 and hence only collision frequencies for local temperature are taken, which maintain the diffusion limit of the transport.

3.7 Ion heat conductivity coefficient

In order to fully enclose the two-temperature heat transfer model described in section 4, *ion heat conductivity coefficients* are supplemented in addition to electron coefficients

introduced in section 3.4. Similar formula to (80) is applied [9]:

$$\kappa_i = \kappa_0 \frac{n_i k_B^2 T_i}{m_i \nu_i} \ , \tag{91}$$

where ν_i is taken from section 3.6.

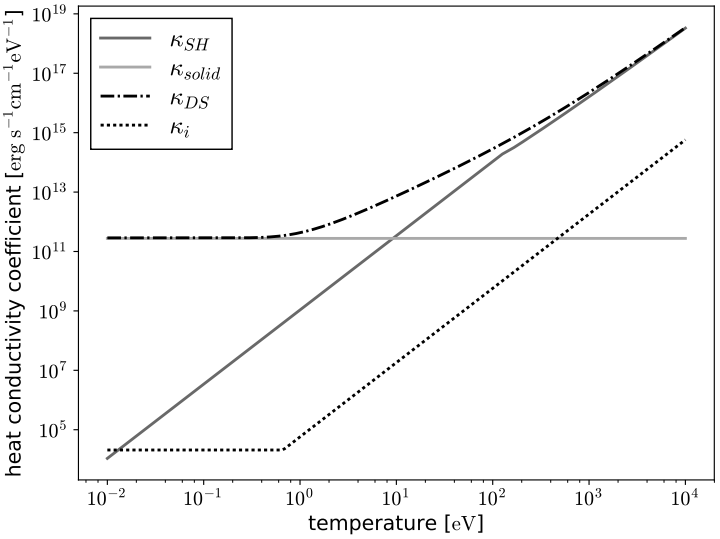

Figure 15: Dependence of the ion heat conductivity coefficient κ_i on temperature ($T = T_e = T_i$) compared to selected models of electron heat conductivity coefficient from section 3.4. Aluminium with density of solid ($\varrho = 2.7$ g/cm^3) is considered with mean ionization $Z = 2.5$.

Resulting heat conductivity coefficient is compared to electron ones in Figure 15. Ion coefficients show to be several orders of magnitude lower than electron one for all temperatures and this effect is even stronger, when taking into account that electron temperatures are typically higher than ion temperatures in plasma. Similar situation occurs in metals, where equilibrium temperature $T = T_e = T_i$ may be considered at the beginning, but heat conduction is strongly dominated by electrons. One should not speak of ion, but rather *lattice* heat conduction there, because ions are integrated into a lattice structure in metals and also phonon scattering must be taken into account. However, it can be typically neglected completely due to small magnitude [45]. This also justifies the procedure for determination of the fitting constants for collision frequency models that attributed all heat conductivity in solids to electrons as described in section 3.4. On the other hand, the model for κ_i gives approximately valid results even in metals, because the values of the lattice conductivity coefficients several orders of magnitude lower than κ_{solid} are known [59].

3.8 Ion extinction coefficient

Since non-local transport of hot ions is also included in the model, ion extinction coefficients must be supplied. Consistently with section 3.5, the ion extinction coefficient k_i is defined as [9]:

$$k_i^{-1} = \frac{128}{3\pi}\lambda_i^\epsilon \doteq 13.6\lambda_i^\epsilon \ , \tag{92}$$

where λ_i^ϵ denotes *ion energy loss mean free path* in this context.

The formula for *ion–ion energy loss collision frequency* is given by (in CGS units with temperatures in eV) [43]:

$$\nu_{ii}^\epsilon = 1.8 \cdot 10^{-7} \frac{n_i Z^4}{A^{1/2}\epsilon_i/k_B} \left((\epsilon_i/k_B)^{-1/2} - 2.2\, T_i^{-1/2} \exp\left(-\frac{\epsilon_i}{k_B T_i}\right)\right) \ln\Lambda_{ii} \quad [\mathrm{s}^{-1}] \ , \tag{93}$$

where ϵ_i denotes microscopical kinetic energy of the colliding ion.

When velocity of ions is approximated by respective thermal velocity v_{Ti} and thermal energy $\epsilon_i = k_B T_i/2$ is substituted into (93), final expression for ion energy loss mean free path is obtained in the form:

$$\lambda_i^\epsilon = \frac{v_{Ti}}{\nu_{ii}^\epsilon} = 5.7 \cdot 10^{-11} \frac{A T_i^2}{\rho Z^4 \ln\Lambda_{ii}} \quad [\mathrm{cm}] \ . \tag{94}$$

Note that the values of λ_i^ϵ are extremely small for low temperatures and transport of ions is effectively disallowed there. The model of non-local transport presented in section 5 assumes free ions and is built from the classical kinetic theory [9]. None of these assumptions holds for low temperatures, where ions are strongly correlated or bounded in a lattice structure. On the other hand, one may think of high energy ions coming from hotter regions that penetrate significantly deeper into the material. Unfortunately, the number of such particles together with their energies are pieces of information that are not included in the transport model. The only available quantity is the total energy intensity of ion flux. Following the discussion in section 3.5, the limit of diffusion transport is maintained and thus only local thermal energies are taken into account.

4 Heat diffusion

Heat diffusion is a classical method of treatment of heat transport phenomena occurring in a medium. Historically, it is used widely in hydrodynamical codes [60]. However, it is well justified only when *Knudsen number* $Kn = \lambda/L$ is sufficiently small, where λ denotes *mean free path* of particles and L is a characteristic distance of a certain phenomena in the medium [61, 62]. In the context of heat transfer, the definition $L = T/|\nabla T|$ can be used, describing the spatial magnitude of temperature perturbations. Unfortunately, the necessary condition $Kn \ll 1$ is not usually met in a conduction zone or a corona for example, where λ can reach $\gtrsim 1$ mm range according to section 3.5. For this reasons, *flux limiters* are necessary, that limit overestimated heat fluxes there. Several types of flux limiters are introduced in section 4.3.

The heat diffusion equation can be derived from a general energy conservation law applied on heat transfer:

$$\rho \frac{\partial \varepsilon}{\partial t} + \nabla \cdot \vec{W} = 0 \ , \tag{95}$$

where $\varepsilon = \varepsilon(t, \vec{x})$ is the *specific internal energy* and $\vec{W} = \vec{W}(t, \vec{x})$ refers to the *heat flux*. The whole phenomena is assumed to be isochoric and thus $\partial\rho/\partial t$ is set zero.

Fourier's law of heat conduction is then taken for the determination of the heat fluxes:

$$\vec{W} = -\kappa \nabla T \ . \tag{96}$$

The symbol κ denotes the *heat conductivity coefficient* here. From the physical point of view, the law essentially states that the fluxes are instantaneously and completely locally responding on a change of temperature. Both of these statements have a limited validity. In the case of ultra-short laser pulses, the temporal dependence is questionable, because of finite relaxation times, and equation (96) is replaced for example by a hyperbolic conservation equation [63]. However, only non-locality of the heat transfer is of the interest for longer pulses and hence a scheme for non-local transport is presented in section 5.

When substituting (96) into (95), the final form of the heat diffusion equation is obtained:

$$\rho \left(\frac{\partial \varepsilon}{\partial T} \right)_\rho \frac{\partial T}{\partial t} = \nabla \cdot (\kappa \nabla T) + f_s \ , \tag{97}$$

where the added term $f_s = f_s(t, \vec{x})$ denotes an arbitrary explicitly given (heat) source function introduced for generalisation of the formulation.

The resulting equation (97) is a *parabolic partial differential equation*, when the coefficient κ as well as $a = \rho(\partial\varepsilon/\partial T)_\rho$ are positive and uniformly lower bounded functions of $(t, \vec{x})$. Unfortunately, both of these coefficients are temperature dependent, making the equation non-linear. For example in plasma, strong dependence $\kappa \sim T^{5/2}$ is typical (see section 3.4). Therefore, non-linear transformation of (95) and (96) is used as described in section 4.1. This procedure effectively removes the strong non-linearity of κ, but a still remains non-linear. Plausible assumption is then made that a is only weakly varying function of temperature. This requirement is for example fully met for ideal gas equation of state, where the specific heat $(\partial\varepsilon/\partial T)_\rho$ is constant. Nevertheless,

the fully conservative form of heat transfer comprising of equation (95) and (96) is preferred whenever it is possible. Also the semi-implicit numerical scheme for heat diffusion introduced in section 4.2 is based on this formulation of the heat transfer equation.

Only the general form of heat diffusion equation has been discussed so far. When applied on the two-temperature model of plasma, the energy equations for electrons and ions are following:

$$\rho \frac{\partial \varepsilon_e}{\partial t} = \nabla \cdot (\kappa_e \nabla T_e) + G_{ei}(T_i - T_e) + f_e \ , \tag{98}$$

$$\rho \frac{\partial \varepsilon_i}{\partial t} = \nabla \cdot (\kappa_i \nabla T_i) + G_{ie}(T_e - T_i) + f_i \ . \tag{99}$$

These equations are derived from the general form of the diffusion equation (97), but the terms responsible for electron–ion energy exchange were added. When ignoring all other terms on the right hand sides of (98) and (99) for the moment, the terms $G_{ei}(T_i - T_e)$ and $G_{ie}(T_e - T_i)$ lead to temperature relaxation between electrons and ions and drive the system towards local equilibrium, i.e. $T_e = T_i$. In order to satisfy energy conservation of the equations, the sum of $\rho\frac{\partial \varepsilon_e}{\partial t} + \rho\frac{\partial \varepsilon_i}{\partial t}$ integrated over the whole domain V must be zero, when setting sources $f_e = f_i \equiv 0$ and applying adiabatic boundary conditions, i.e. $\vec{W}|_{\partial V} \equiv 0$. Utilizing Gauss theorem, only the energy exchange terms remain. In order to satisfy the energy conservation for any solution in temperatures, the coefficients of energy exchange must be equal, i.e. $G_{ei} = G_{ie}$. This requirement was further discussed in section 3.3 and symmetrizes the equations (98) and (99). Unfortunately, non-linearity appears even in these terms, since both coefficients depend on temperatures. However, the energy exchange terms are supposed to be quantitatively small compared to the other terms, because energy loss collision frequency is typically very small in a hot plasma (see sections 3.2 and 3.3).

The electron heat conductivity coefficient κ_e is taken from one of the models presented in section 3.4 and ion heat conductivity coefficient κ_i are calculated according to section 3.7. The heat conductivity coefficients as well as the specific heats $(\partial \varepsilon_e/\partial T_e)_\rho$ and $(\partial \varepsilon_i/\partial T_i)_\rho$ and the energy exchange coefficients are (after the non-linear transformation) frozen, i.e. set constant throughout the time step similarly to section 5.

4.1 Non-linear transformation

In order to remove the non-linearity in the heat conductivity coefficient of the general diffusion equation (97), a non-linear transformation is applied. The key parameter is the nominal order of temperature dependency of κ denoted as p. In the case of plasma simulations, it has value $p = 5/2$, since the Spitzer regime is dominating here (see sections 3.4 and 3.7). Non-linear transformation is then performed in temperature as

follows [64]:

$$\theta = T^{p+1} \ , \tag{100}$$

$$\bar{\kappa} = \frac{\kappa}{p+1}\theta^{-\frac{p}{p+1}} = \frac{\kappa}{p+1}T^{-p} \ , \tag{101}$$

$$\bar{a} = \frac{a}{p+1}\theta^{-\frac{p}{p+1}} = \frac{a}{p+1}T^{-p} \ . \tag{102}$$

This allows to rewrite the system of equations (95) and (96) in the form:

$$\bar{a}\,\frac{\partial\theta}{\partial t} + \nabla\cdot\vec{W} = 0 \ , \tag{103}$$

$$\vec{W} = -\bar{\kappa}\nabla\theta \ . \tag{104}$$

The resulting system of equations (103) and (104) has completely analogical form as the original system (95), (96). However, $\bar{\kappa}$ is free of the nominal power dependency. On the other hand, a slight additional non-linearity was brought into the coefficient $\bar{a}$, but conservation of the scheme is not threatened, because the diffusion scheme presented in section 4.2 gives values of heat fluxes, that were not transformed, and conservative update of ε through equation (95) can be used.

Different situation occurs when one applies the transformation on the two-temperature system (98), (99). It essentially breaks the symmetry of the system jeopardizing the convergence. Hence, application of the non-linear transformation on the energy exchange terms is discouraged.

4.2 Semi-implicit diffusion scheme

A semi-implicit diffusion scheme of the second order in space and time was derived in the previous work [13]. It is based on the *mimetic operators* approach [65], where discrete operators are introduced, that take over some of the properties of their continuous analogues. A brief description of the scheme is given here. It must be noted that the scheme is derived for the general heat diffusion equation (97) or rather the system of equations of heat transfer (95),(96), because the specific electron and ion equations (98), (99) are taking exactly the same form except the energy exchange terms, that are discussed separately in section 4.4.

As discussed in the introduction, the fully conservative form of heat transfer is preferred comprising of the equations (95),(96). In order to derive a self-consistent system of equations, the temperature T and the heat flux $\vec{W}$ are chosen as the primary variables. Since the temperature will be eliminated later and only fluxes will remain, the conservation will not perish. The system of governing equations is following:

$$a\,\frac{\partial T}{\partial t} + \nabla\cdot\vec{W} = f_s \ , \tag{105}$$

$$\vec{W} = -\kappa\nabla T \ . \tag{106}$$

This can be also seen as a decomposition of the original second order partial differential

equation (97) into a system of first order partial differential equations.

The system (105), (106) has completely identical form as the transformed system (105), (106) (except the source function f_s, but it is not affected by the transformation). This fact is utilised in the simulation code and the diffusion solver does not need to distinguish between the two forms and the preceding non-linear transformation can be easily removed from the computation sequence. Hence, the two forms are not distinguished even in the text for brevity of the description and we always refer to the system (105), (106), even thought the non-linear transformation was used for all numerical simulations presented in section 6.

The system of equations (105), (106) is solved on the domain V with a Lipschitz boundary, where the boundary conditions of the Neumann type (from the point of view of the diffusion equation (97)) are assumed in the form:

$$-\vec{W} \cdot \vec{n}\Big|_{\partial V} = \psi_W \ , \tag{107}$$

where $\vec{n}$ denotes the outer normal and $\psi_W = \psi_W(t, \vec{x})$ is a smooth function on the boundary ∂V. However, the adiabatic boundary condition was usually used for the simulations of laser plasma simulations in section 6, i.e. $\psi_W \equiv 0$.

Semi-implicit time discretization of the system (105), (106) and the boundary condition is performed as follows:

$$a\frac{T^{n+1} - T^n}{\Delta t} + \nabla \cdot \vec{W}^{n+1/2} = f_s^{n+1/2} \ , \tag{108}$$

$$\vec{W}^{n+1/2} = -\kappa \nabla T^{n+1/2} \ , \tag{109}$$

$$-\vec{W}^{n+1/2} \cdot \vec{n}\Big|_{\partial V} = \psi_W^{n+1/2} \ . \tag{110}$$

The discrete time levels are denoted by the integer in upper index, where n refers to the current time level and Δt is the length of the computational step. The half-integer values are abbreviations of $f_s^{n+1/2} = \frac{1}{2}(f_s^n + f_s^{n+1})$, $T^{n+1/2} = \frac{1}{2}(T^n + T^{n+1})$ and $\psi_W^{n+1/2} = \psi_W(t^n + \frac{1}{2}\Delta t)$. For simplicity, the coefficients a and κ are written without upper indices, because they are taken constant during the time step as mentioned in the introduction, so strictly speaking $a = a^n$ and $\kappa = \kappa^n$ in the context of discretized equations.

The next step is the definition of *abstract operators* that unify the equations (108–110) into the form:

$$D\vec{W}^{n+1/2} + \Omega T^{n+1} = F^{n+1/2} \ , \tag{111}$$

$$\vec{W}^{n+1/2} - GT^{n+1/2} = 0 \ , \tag{112}$$

where we call D generalised divergence operator, G generalised gradient operator and

finally Ω generalised mass operator. The function of the right hand side F is defined as:

$$F^{n+1/2} = \begin{cases} f_s^{n+1/2} + \Omega T^n & \text{on } V \\ \psi_W^{n+1/2} & \text{on } \partial V \end{cases} . \tag{113}$$

Similarly, the operators are defined as follows:

$$GT = -\kappa \nabla T \ , \tag{114}$$

$$D\vec{W} = \begin{cases} \nabla \cdot \vec{W} & \text{on } V \\ -\vec{W} \cdot \vec{n} & \text{on } \partial V \end{cases} , \tag{115}$$

$$\Omega T = \begin{cases} (a/\Delta t)T & \text{on } V \\ 0 & \text{on } \partial V \end{cases} . \tag{116}$$

All linear operators are defined for functions of spatial coordinates on closure of V, where we omitted the temporal dependence, because it appears in the equations (111), (112) only parametrically, since the time discretization has been already performed. However, the coefficients a, κ and Δt are assumed to be given on the current time level.

The appropriate function spaces must be mentioned for completeness. Hilbert spaces H and $\vec{H}$ of scalar and vector valued smooth functions of spatial coordinate on the closure of domain V respectively are used, where the inner products are defined as ($u, v \in H$ and $\vec{U}, \vec{V} \in \vec{H}$):

$$(u, v)_H = \int_V u \ v \ \mathrm{d}V + \oint_{\partial V} u \ v \ \mathrm{d}S \ , \tag{117}$$

$$(\vec{U}, \vec{V})_{\vec{H}} = \int_V \frac{1}{\kappa} \vec{U} \cdot \vec{V} \, \mathrm{d}V \ . \tag{118}$$

The cornerstone of the method of mimetic operators is the definition of the *primary operator* and inference of all other operators consistently from it. In this case, the primary operator is said to be the divergence operator D [65].

Utilizing Gauss theorem ($\int_V \nabla \cdot \vec{U} \, \mathrm{d}V = \oint_{\partial V} \vec{U} \cdot \vec{n} \, \mathrm{d}S$) and the definitions of inner products (117), (118) and as well the definitions of operators D and G (115), (114), a useful relation between the operators can be derived:

$$(D\vec{U}, u)_H = (\vec{U}, Gu)_{\vec{H}} \ . \tag{119}$$

It states that $G = D^*$, meaning that G is the adjoint operator to D in appropriate inner products.

We now proceed by elimination of the temperature T^{n+1} from the equations (111), (112) inside the domain V, where the inverse of Ω exists, since it is positive definite there. The resulting equation for fluxes then can be written as (I is the identity

operator):

$$\left(I \ + \frac{1}{2} G\Omega^{-1} D\right) \vec{W}^{n+1/2} = \frac{1}{2} G\Omega^{-1} F^{n+1/2} + \frac{1}{2} G T^n \ . \tag{120}$$

The next step in the inference of the scheme is the spatial discretization of the continuous operators and finally of the equation (120). We do not give full definitions of the spatially discretized operators here and we point the readers to the previous work [13], where detailed description of 1D discretization was made, including a comparison of two possible variants, or to the original paper [65], where 2D case is discussed. However, it must be noted that the spatial discretization is *staggered* consistently with the hydrodynamic scheme described in section 5. This means that the heat fluxes from Hilbert space $\vec{H}$ are projected onto the boundaries of computational cells unlike the temperatures from Hilbert space H that are projected into the computational cells.

Two families of inner products are distinguished for spatial discretization. These are *natural inner products* denoted as $(u, v)_{HC}$ and $(\vec{U}, \vec{V})_{HL}$ for scalar and vector grid functions respectively. The key feature is that both of them are consistent with their respective inner products (117), (118). Another family are *formal inner products* written as $[u, v]_{HC}$ and $[\vec{U}, \vec{V}]_{HL}$. These inner products are useful for the construction of the matrix of the scheme, because they are free of geometry related coefficients and also they separate function values on each of the grid points.

In order to relate both types of inner products, conversion operators are introduced. They are formally defined by the implicit relations:

$$(u, v)_{HC} = [\mathcal{M}u, v]_{HC} \ , \tag{121}$$

$$(\vec{U}, \vec{V})_{HL} = [\mathcal{L}\vec{U}, \vec{V}]_{HL} \ . \tag{122}$$

However, they can be expressed explicitly using the definitions of the natural and formal inner products [13, 65].

Finally, the primary operator must be discretized. In this case, the primary operator is the divergence operator D as mentioned earlier. Its discrete analogue $\mathcal{D}$ is defined as a *central finite difference* approximation of it.

Keeping in mind the relation $G = D^*$, the similar relation $\mathcal{G} = \mathcal{D}^*$ for discrete operators in natural inner products is required. The discrete gradient operator $\mathcal{G}$ is then implicitly given by:

$$(\mathcal{D}\vec{U}, u)_{HC} = (\vec{U}, \mathcal{D}^* u)_{HL} \tag{123}$$

and in formal inner products:

$$[\mathcal{D}\vec{U}, \mathcal{M}u]_{HC} = [\vec{U}, \mathcal{L}\mathcal{D}^* u]_{HL} \ . \tag{124}$$

Utilizing the adjoint operator $\mathcal{D}^{\circledast}$ to $\mathcal{D}$ in formal inner products, (124) can be rewritten as:

$$[\vec{U}, \mathcal{D}^{\circledast}\mathcal{M}u]_{HC} = [\vec{U}, \mathcal{L}\mathcal{D}^* u]_{HL} \ . \tag{125}$$

This yields the important relation $\mathcal{D}^{\circledast}\mathcal{M} = \mathcal{L}\mathcal{D}^*$. Hence, the discrete gradient operator $\mathcal{G}$ is explicitly given by:

$$\mathcal{G} = \mathcal{D}^* = \mathcal{L}^{-1}\mathcal{D}^{\circledast}\mathcal{M} \ . \tag{126}$$

It can shown that the conversion operator $\mathcal{L}$ is positive definite and banded by definition [13, 65]. Therefore, its inverse exists, but it may not be banded any more. This pose a severe issue for the simulation code, because inversion of a full matrix is computationally expensive operation in general. This is addressed later by using the compound $\mathcal{LG}$ instead of only plain operator $\mathcal{G}$.

The abstract operator Ω must be formally also discretized, but since it leads by point projection to only a discrete operator with a diagonal matrix, the same notation Ω is used for it too.

Finally, the system of equations (111), (112) can be formally discretized as follows:

$$\mathcal{D}\vec{W}^{n+1/2} + \Omega T^{n+1} = \mathcal{F}^{n+1/2} \ , \tag{127}$$

$$\vec{W}^{n+1/2} - \mathcal{G}T^{n+1/2} = 0 \ , \tag{128}$$

where $\mathcal{F}$ refers to the point projection of the function of the right hand side F.

Temperatures can be eliminated from the system similarly to the equation (120) resulting in the heat flux equation:

$$\left(\mathcal{I} + \frac{1}{2}\mathcal{G}\Omega^{-1}\mathcal{D}\right)\vec{W}^{n+1} = \frac{1}{2}\mathcal{G}\Omega^{-1}\mathcal{F} + \frac{1}{2}\mathcal{G}T^{n} \ . \tag{129}$$

As proposed earlier, the discrete operator $\mathcal{G}$ cannot be used alone, because the matrix on the left hand side of (129) is not banded in general. Multiplying both sides by operator $\mathcal{L}$ and applying property (126), the equation is taking form:

$$\left(\mathcal{L} + \frac{1}{2}\mathcal{D}^{\circledast}\mathcal{M}\Omega^{-1}\mathcal{D}\right)\vec{W}^{n+1} = \frac{1}{2}\mathcal{D}^{\circledast}\mathcal{M}\Omega^{-1}\mathcal{F} + \frac{1}{2}\mathcal{D}^{\circledast}\mathcal{M}T^{n} \ . \tag{130}$$

It must be noted that the equation (130) holds only inside the domain V, where the inverse operator Ω^{-1} exists, because the Neumann type boundary condition was used. Hence, the right hand side can be simplified using the definition of F (113) and point projected function f_s:

$$\left(\mathcal{L} + \frac{1}{2}\mathcal{D}^{\circledast}\mathcal{M}\Omega^{-1}\mathcal{D}\right)\vec{W}^{n+1/2} = \frac{1}{2}\mathcal{D}^{\circledast}\mathcal{M}\Omega^{-1}f_s^{n+1/2} + \mathcal{D}^{\circledast}\mathcal{M}T^{n} \ . \tag{131}$$

The discrete heat fluxes $\vec{W}^{n+1/2}$ on the boundary of V are then determined by the boundary condition (110) applied on the appropriate grid functions.

The final matrix of the semi-implicit scheme (131) is positive definite and also banded [65]. Moreover, it is tridiagonal in 1D [13]. This allows to employ very effective solvers for this linear system. *Thomas algorithm* is used in 1D and *conjugate gradient method* (CG) [66] preconditioned by *alternating–direction implicit* (ADI) method is used in 2D [67].

Finally, the update of temperatures can be performed based on the equation (127):

$$T^{n+1} = T^{n} + \Omega^{-1}f_s^{n+1/2} - \Omega^{-1}\mathcal{D}\vec{W}^{n+1/2} \ . \tag{132}$$

However, this approach is discouraged, since energy conservation is not guaranteed due to a weak dependence of coefficient a and consequently Ω on temperature. Therefore, the update through the equation of energy conservation (95) is preferred:

$$\varepsilon^{n+1} = \varepsilon^n + \frac{\Delta t}{\rho} f_s^{n+1/2} - \frac{\Delta t}{\rho} \mathcal{D}\vec{W}^{n+1/2} \ . \tag{133}$$

The grid function of density ρ does not change during the step, since the phenomena is assumed to be isochoric and thus the time level index was omitted.

4.3 Heat flux limiter

Heat flux limiters are a necessary part of the heat diffusion scheme, because diffusion approximation is usually made even beyond the domain of validity as mentioned in the introduction. Normally, this leads to overestimations of heat fluxes in the medium. Subsequent heat flux limiting methods then limit the heat flux directly or indirectly in order to approach reasonable values. *Free-streaming heat flux* is usually taken as the reference one:

$$W_e^{fs} = n_e v_{Te} k_B T_e = \frac{k_B}{m_u} \sqrt{\frac{k_B}{m_e}} \frac{Z}{A} \rho T_e^{3/2} \ , \tag{134}$$

$$W_i^{fs} = n_i v_{Ti} k_B T_i = \frac{k_B}{m_u} \sqrt{\frac{k_B}{m_u}} A^{-3/2} \rho T_i^{3/2} \ . \tag{135}$$

Only a portion of W^{fs} is taken as the maximal value of heat flux $W^{max} = f^{max} W^{fs}$, where the type of the specie was omitted, because the limiting methods are identical. The constant f^{max} can be used for adjustment of the values to empirical or theoretical predictions [60, 68, 69]. The value $f^{max} = 0.05$ was used for the simulations in section 6, but also a comparison of results with different values is made there. However, the constant cannot fully reflect the non-locality of the transport and whole method is only approximative as discussed in the introduction.

The most straight-forward method of flux limiting is to directly limit the values of heat flux by the formula of type $\min(\left|\vec{W}\right|, W^{max})$. Unfortunately, the values of heat flux are then almost solely driven by the value of W^{max} in corona, since (unlimited) heat fluxes strongly exceed the limit W^{max} in a large area as can be concluded from the simulations in section 6. Moreover, the situation is more complicated in staggered discretization (see section 1), because W^{max} is naturally a central quantity by definition. Therefore, we define nodal heat flux fraction in 1D first of all:

$$f_j^{lim} = \begin{cases} \dfrac{\left|\vec{W}_j\right|}{W_{j-1/2}^{max}} & \vec{W}_j \cdot \vec{z}_0 > 0 \\ \dfrac{\left|\vec{W}_j\right|}{W_{j+1/2}^{max}} & \vec{W}_{j+1} \cdot \vec{z}_0 < 0 \end{cases} \ , \tag{136}$$

where $\vec{z}_0$ is the unit vector along the z axis. The formula has upwind nature in order

to stabilise the heat flux limiting methods, that is found to be absolutely necessary when strong limiting is applied.

The simple *direct cut-off heat flux limiter* then can be formally written as:

$$\vec{W}_j^{cutoff} = \min\left(1, \frac{1}{f_j^{lim}}\right) \vec{W}_j \ . \tag{137}$$

However, the sharp threshold value in the limiter may cause non-physical behaviour and create artefacts in the simulation (see section 6). Therefore, the heat flux limiter is used mainly as a reference. The heat flux limiter based on harmonic mean, which we refer to as *direct harmonic mean heat flux limiter*, smoothly limits the heat flux and hence is preferred in this case:

$$\vec{W}_j^{harm} = \frac{1}{1 + f_j^{lim}} \vec{W}_j \ . \tag{138}$$

In order to maintain the behaviour of the diffusion transport, flux limiters based on heat conductivity coefficient reduction are applied instead, because the dependence on the gradient of temperature is preserved.

First of all, the central heat flux fraction must be introduced:

$$f_{j+1/2}^{lim} = \max\left(\frac{\left|\vec{W}_j\right|}{W_j^{max}}, \frac{\left|\vec{W}_{j+1}\right|}{W_{j+1}^{max}}\right) \ , \tag{139}$$

where the nodal heat flux limit is taken as $W_j^{max} = \min(W_{j-1/2}^{max}, W_{j+1/2}^{max})$,

The *harmonic mean heat flux limiter* then gives modified heat conductivity coefficients as follows:

$$\kappa_{j+1/2}^{harm} = \frac{1}{1 + f_{j+1/2}^{lim}} \kappa_{j+1/2} \ . \tag{140}$$

Another possible construction of heat flux limiter is referred to as the *rescaling heat flux limiter* here:

$$\kappa_{j+1/2}^{rescale} = \min\left(1, \frac{1}{f_{j+1/2}^{lim}}\right) \kappa_{j+1/2} \ . \tag{141}$$

This version of flux limiter is also present in the 2D simulation code PALE2 unlike the other forms, that are only implemented in the 1D code PETE.

However, it can be observed that the two heat flux limiters (140) and (141) are highly similar and also the simulations in section 6 support it. An advantage and also a disadvantage, depending on the point of view, of both of them is that they do not prohibitively limit heat fluxes and the fluxes can still reach extremely high values locally. The heat flux fraction (139) then does not fully reflect the action of the heat flux limiter on the heat fluxes. Moreover, strong heat fluxes can affect the spatial profiles of quantities significantly. On the other hand, the behaviour remains fully diffusive, because the coefficients κ are theoretically arbitrary in the definition of the

general diffusion equation (97) as opposed to the heat fluxes $\vec{W}$ that are defined by (96).

4.4 Electron–ion temperature relaxation

Electron–ion temperature relaxation has not been discussed so far, even though it plays a key role in the simulation of laser plasma, because ions are heated exclusively from electrons in the model (see section 5). Two different approaches are discussed here, even though only one of them is actually used. The starting point for both of them are the equation (105), (106) formulated for two-temperature system according to (98), (99):

$$a_e \frac{\partial T_e}{\partial t} + \nabla \cdot \vec{W}_e = f_e + G_{ei}(T_i - T_e) \ , \tag{142}$$

$$\vec{W}_e = -\kappa_e \nabla T_e \ , \tag{143}$$

$$a_i \frac{\partial T_i}{\partial t} + \nabla \cdot \vec{W}_i = f_i + G_{ie}(T_e - T_i) \ , \tag{144}$$

$$\vec{W}_i = -\kappa_i \nabla T_i \ . \tag{145}$$

Proceeding similarly to section 4.2, the system of partial differential equations is discretized in time and abstract operators are introduced for both species ($G_{ei} = G_{ie}$ operators are zero on ∂V):

$$D_e \vec{W}_e^{n+1/2} + \Omega_e T_e^{n+1} = F_e^{n+1/2} + G_{ei}(T_i^{n+1} - T_e^{n+1}) \ , \tag{146}$$

$$\vec{W}_e^{n+1/2} - G_e T_e^{n+1/2} = 0 \ , \tag{147}$$

$$D_i \vec{W}_i^{n+1/2} + \Omega_i T_i^{n+1} = F_i^{n+1/2} + G_{ie}(T_e^{n+1} - T_i^{n+1}) \ , \tag{148}$$

$$\vec{W}_i^{n+1/2} - G_i T_i^{n+1/2} = 0 \ . \tag{149}$$

Unlike section 4.2, the temperatures cannot be eliminated from the system and also definitions of Hilbert spaces for the heat fluxes are different for electrons and ions (see the definition of inner products (118)). Therefore, the heat fluxes are eliminated instead:

$$\left(\frac{1}{2} D_e G_e + \Omega_e + G_{ei}\right) T_e^{n+1} = F_e^{n+1/2} + G_{ei} T_i^{n+1} - \frac{1}{2} D_e G_e T_e^n \ , \tag{150}$$

$$\left(\frac{1}{2} D_i G_i + \Omega_i + G_{ie}\right) T_i^{n+1} = F_i^{n+1/2} + G_{ie} T_e^{n+1} - \frac{1}{2} D_i G_i T_i^n \ . \tag{151}$$

The operators of the left hand side are later denoted as $\left(\tilde{A}_e + G_{ei}\right)$ and $\left(\tilde{A}_i + G_{ie}\right)$ for simplification of notation in the text. Both operators $\tilde{A}_e$ and $\tilde{A}_i$ possesses positive properties, they are self-adjoint and positive, because $D_e G_e = D_e D_e^* = G_e^* G_e$ (and analogously for ions) according to (119). It must be also noted that functional spaces of electron and ion temperatures are identical according to the definition (117). Moreover, the inverse of $G_{ei} = G_{ie}$ exists inside the domain V. These facts allow to eliminate one

of the temperatures in each equation:

$$\left(\tilde{A}_i G_{ei}^{-1} \tilde{A}_e + \tilde{A}_e + \tilde{A}_i\right) T_e^{n+1} = \tilde{A}_i G_{ei}^{-1} \left(F_e^{n+1/2} - \frac{1}{2} D_e G_e T_e^n\right) + \left(F_i^{n+1/2} - \frac{1}{2} D_i G_i T_i^n\right) , \tag{152}$$

$$\left(\tilde{A}_e G_{ie}^{-1} \tilde{A}_i + \tilde{A}_i + \tilde{A}_e\right) T_i^{n+1} = \tilde{A}_e G_{ie}^{-1} \left(F_i^{n+1/2} - \frac{1}{2} D_i G_i T_i^n\right) + \left(F_e^{n+1/2} - \frac{1}{2} D_e G_e T_e^n\right) . \tag{153}$$

The Neumann type boundary conditions (107) need special treatment, because heat fluxes were completely removed from the system. However, this problem is fully revealed only after spatial discretization. The spatial discretization then follows section 4.2. One possibility is then to revert the elimination of heat fluxes on the boundary, where heat fluxes are determined by the boundary condition. Another possibility is to solve a larger linear system containing also auxiliary temperatures beyond the boundary, which are given by equations (147) and (149) (or rather their discrete analogues). Note that multiplication of these auxiliary equations by discrete operator $\mathcal{L}$ is also beneficial here.

The linear system (152), (153) represents the final form of the scheme in terms of abstract operators. The operators of the left hand side are positive definite, but when spatially discretized, they do not lead to operators with banded matrices in general. Inversions of full matrices are then needed and this approach becomes computationally expensive. Moreover, the scheme is not energy conservative, since it is temperature based unlike the original scheme from section 4.2. These disadvantages prevail over the advantages and different approach is used instead.

The second approach is based on the *operator splitting* method [16, 15], where the temporal evolution of temperature or specific internal energy according to (98), (99) is split into two parts. The first one is diffusive and solved by the semi-implicit scheme introduced in section 4.2 and the other one is solely describing electron–ion energy exchange:

$$a_e \frac{\partial T_e}{\partial t} = G_{ei}(T_i - T_e) , \tag{154}$$

$$a_i \frac{\partial T_i}{\partial t} = G_{ie}(T_e - T_i) . \tag{155}$$

The numerical scheme is then based on the explicit analytical solution of the equations (154), (155) [64]. The coefficients a_e, a_i are assumed to be constant during the time step, because non-linearity of $\varepsilon(T)$ relation is assumed to be weak. One then observes that the sum of the equations is exactly zero and thus $E^{relax} = a_e T_e + a_i T_i$ is an invariant. Inserting the invariant into both equations, the system of two ordinary

differential equations is obtained:

$$a_{ei}\,\frac{\mathrm{d}T_e}{\mathrm{d}t} = -G_{ei}T_e + G_{ei}\frac{E^{relax}}{a_e + a_i}\ , \tag{156}$$

$$a_{ei}\,\frac{\mathrm{d}T_i}{\mathrm{d}t} = -G_{ie}T_i + G_{ie}\frac{E^{relax}}{a_e + a_i}\ , \tag{157}$$

where total heat capacity was introduced as $a_{ei} = 1/(1/a_e + 1/a_i)$.

The equations (156) and (157) can be solved analytically, giving rise to the expressions for temperatures:

$$a_e T_e^{n+1} = \frac{E^{relax}}{1 + \frac{a_i}{a_e}} + a_{ei}(T_e^n - T_i^n)\exp\left(-\frac{G_{ei}}{a_{ei}}\Delta t\right)\ , \tag{158}$$

$$a_i T_i^{n+1} = \frac{E^{relax}}{1 + \frac{a_e}{a_i}} + a_{ei}(T_i^n - T_e^n)\exp\left(-\frac{G_{ie}}{a_{ei}}\Delta t\right)\ . \tag{159}$$

However, the scheme is still not energy conservative, because of the non-linear nature of dependency of internal energy on temperature. Therefore, the scheme must be rather formulated in terms of increments of ε_e and ε_i. In order to obtain this form, $a_e T_e^n$ and $a_i T_i^n$ terms are subtracted from (158) and (159) respectively and specific internal energies are reintroduced:

$$\rho(\varepsilon_e^{n+1} - \varepsilon_e^n) = a_{ei}(T_i^n - T_e^n)\left(1 - \exp\left(-\frac{G_{ei}}{a_{ei}}\Delta t\right)\right)\ , \tag{160}$$

$$\rho(\varepsilon_i^{n+1} - \varepsilon_i^n) = a_{ei}(T_e^n - T_i^n)\left(1 - \exp\left(-\frac{G_{ie}}{a_{ei}}\Delta t\right)\right)\ . \tag{161}$$

The resulting scheme is conveniently simple and clearly energy conservative. It should be also noted that the Taylor polynomial of the first order of the exponentials in (160), (161) gives directly the explicit scheme for temperature relaxation. This scheme then can be seen as an extended version of it for arbitrarily long time steps as long as the non-linearity of ε does not play the main role in convergence.

The computational sequence then comprises of the update of temperatures by the diffusion scheme producing temperatures on an intermediate time level. The temperature scheme follows, starting from the intermediate time level and ending on the new time level. The key assumption for the operator splitting is that the two phenomena are not tightly coupled, but this is not usually the case for heat transport and el–ion temperature relaxation. Otherwise, the fully implicit approach in temperatures for the non-local transport scheme introduced in section 5 is also available, but no significant differences between both approaches were observed in section 6.

5 Non-local transport model

Following the discussion in section 4, the diffusion approximation of heat transfer is not sufficient to describe complex transport phenomena in plasma. The main concerns about validity of the model are rising from the fact that the mean free paths of the transported species highly exceed the spatial scales of temperature perturbations and this leads to overestimations of heat fluxes. This problem was addressed by application of additional *heat flux limiters* in section 4.3, that crudely limit the heat fluxes to physically meaningful values. Indications of non-locality of the transport were recognised several decades ago [60] and various models of non-local transport have been developed since then [70, 71, 72]. The main focus of the still ongoing research is pointed on transport of hot electrons in plasma, because electrons hold most of the energy of the plasma [22] and hot electrons are produced by laser–plasma interaction [51]. However, there are three main transport regimes that must be distinguished by the *Knudsen number* Kn.

As described in section 3.5, the mean free path of electrons can overgrow the spatial scale of a corona. On the other hand, no steep gradients in densities nor temperatures are present. Nevertheless, the Knudsen number of electrons becomes $Kn_e > 10$. The plasma is typically hot in corona ($\gtrsim 100$ eV) and under-critical for the laser wave and with densities several orders of magnitude lower than the density of solid material. The electrons in this zone can easily pass through, so the regime is referred to as the *free streaming* regime. The thermal diffusion itself manifestly overestimates the heat exchange and (near) saturation of temperature is observed. Heat fluxes or consequently heat conductivity coefficients are strongly driven by heat flux limiters as concluded in section 4.3. The proper non-local electron transport model presented in section 5.1 usually does not reproduce this phenomena, because of the transparency of the area, and the evolution of the system is typically closer to adiabatic expansion as predicted theoretically and experimentally [73].

The second regime describes so called *conduction zone*, where density declines rapidly in a rarefaction wave and transport phenomena drive the ablation of the material. The Knudsen number has moderate values $0.001 < Kn_e < 10$ there. The non-local transport is very effective in this area, because hot electrons created near the critical plane can penetrate the upstream and heat the material. Diffusion approximation leads to creation of non-linear heat waves [22], but there are significant differences of both approaches as shown in the simulation results in section 6.

The last, but not least important regime is characteristic by low values of Knudsen number $Kn_e < 0.001$. This is typically the case of solid material or moderate shock waves. The medium is opaque for electrons and they are stopped on short distances as discussed in section 3.5. The expansion in small parameter of distribution function is possible using Chapman–Enskog method [74] and the regime is approximately diffusive. Classical thermal diffusion is able to describe the transport in this area, but even non-local transport model described in section 5.1 maintains the diffusive limit of the transport for small mean free path and hence it is possible to describe the transport within it, provided that an appropriate closure model is supplied for calculation of the mean free path. However, stronger shock waves can cause pre-heating of the material by

non-local transport, that cannot be precisely described by classical thermal diffusion, but we do not investigate this effect in details in this text and further improvements of the physical model may be needed to properly describe this phenomena.

Historically, the non-local nature of the transport was addressed by models based on spatial convolution of the heat fluxes. This approach was pioneered by the work of Luciani, Mora and Virmount (LMV) [70, 75], where a convolution over the classical Spitzer-Härm heat fluxes (see section 4) was applied. Even though that the model solved the ubiquitous problem of flux limiting in heat diffusion simulations (see section 4.3) and was able to estimate the pre-heating of the material, the model must be supplied by an ad-hoc parameter residing in the convolution kernel. Fitting of proper Fokker–Planck (FP) simulations is then necessary and reliability of the model in hydrodynamical codes is questionable. Later, the mentioned problems were addressed in the model of Albritton, Williams, Bernstein and Swartz (AWBS) [71], where the convolution kernel is derived from a solution of a simplified form of the FP equation. The LMV convolution kernel was further improved by adding electric field in [76] and other improved versions of the methods appeared [77]. However, numerical issues inherently included in the LMV/AWBS models were revealed [78]. Consequently, several models removing this deficiency were proposed later [79, 80]. Furthermore, several theoretical models were derived from simplified Fokker–Planck equation [81, 82, 83] later followed by simulation codes solving the non-local closure in Fourier space [84, 85].

Another drawback of the classical convolution based approach originates from the inability to extend the models to more dimensions. An innovative model was presented by Schurtz, Nicolai and Busquet (SNB) [72], that can be solved in multi-dimensions. The basic form of the model originates from solution of the simplified Boltzmann equation proposed by Bhatnagar, Gross and Krook (BGK) [86]. However, its extensions were developed to include self-consistent electric and magnetic fields [87].

Although the convolution based models became very popular due to their implementation simplicity, they are inherently based on the Chapman–Enskog small parameter expansion method [74], that is the foundation of the Spitzer-Härm heat conduction model [14].

Problems of anisotropy of the transport was recognised and models based on angular moments of simplified Boltzmann equation were proposed later [88, 89, 90, 91].

A completely different approach was proposed relatively recently, where a simplified kinetic model of non-local transport is incorporated into a hydrodynamical simulation [92]. Due to long time scales typical for hydrodynamics, a stationary BGK kinetic equation is solved. The BGK operator was then further improved and theoretically validated in [93, 94].

Based on this approach, a first-principal method was developed in [9], that relies on numerical solution of BGK Boltzmann transport equation for photons, electrons and ions. This text continues the development and implementation of this transport closure into the simulation code PETE as described in section 5.1. The advantages of this model include proper description of angular distributions, where Legendre or small parameter expansions are not made. Instead, dimensionality of the problem is increased by additional solid angle of propagation of transported species. Hence, almost full phase space is formed, but averaging over the energy spectrum is performed and also

the time scales remain on the level of hydrodynamics making the model viable closure of the hydrodynamic simulations. However, numerical solution of the linear kinetic equation necessarily increases the computational costs of the simulations, but *high order finite element* scheme presented in section 5.2 is employed to handle numerically the transport phenomena with remarkable effectiveness.

Only electron species has been discussed so far, but similar division with respect to Knudsen number can be applied on other particles like ions. The contribution of ion thermal diffusion was insignificant, because of small values of the heat conductivity coefficient compared to the electron one (see section 3.7). Similarly, the non-local transport of ion species is typically weaker than the electron transport due to high extinction coefficient according to section 3.8. However, the two transport mechanisms are not directly comparable, since the electron and ion temperatures approximately coincide in a solid and the conduction zone, but not in a corona. The electron temperature is typically several orders of magnitude higher than the ion temperature at the same point in space. This effect together with the fact that the ion collision frequency decreases with temperature causes that ions does not fully reach the free-streaming limit. However, non-local ion heat transport is usually neglected in hydrodynamical codes and literature about modelling of this phenomena is rather scarce, but theoretical studies based on Fokker–Planck equation exist [95, 96]. The state-of-art ion transport model is presented here together with other transport mechanisms.

Finally, radiation transport is one of the most important parts of the simulation. Together with the hydrodynamical description of plasma, it forms the specific research area of radiation hydrodynamics [62, 97, 98]. In particular, radiation transport is very important even for laser–target simulations. Unlike electrons or ions, radiation is not governed by the charge conservation law. From the numerical point of view, the reflective boundary conditions are not enforced. Hence, radiation freely escapes the corona leading to the *radiation cooling* effect [99]. It is known that radiation transport is dominant for high-Z materials, that produce strong X-ray radiation, which cools the plasma on one hand. On the other hand, it is transported into the upstream of the laser ablation wave, through the conduction zone and finally reaching the rarefaction wave. It is absorbed and eventually re-emitted there. In some cases, the transport is sufficiently strong to cause the formation of so called *double ablation front* structure, where an ablation front similar to the laser ablation one is growing within the rarefaction wave [100, 101].

All three transport mechanisms, i.e. electron, ion and radiation transport, are all described in a similar manner as shown in section 5.1. All together, the model essentially poses a closure of the two-temperature single fluid hydrodynamical scheme presented in section 1. Eventually, the diffusion scheme is employed, but due to implicit nature of both schemes, operator splitting technique is used in order to connect them together similarly to section 4.4. The temporal discretization is solved this way, but the spatial discretization does not match in general, because the finite element (FEM) scheme allows arbitrary spatial order of the temperature elements. Therefore, the mean value projection is applied on electron and ion temperatures. The discretized temperatures on the finite elements then enter the hydrodynamical scheme in this form and the reverse process, when the temperatures from the hydrodynamical scheme up-

date the non-local scheme quantities, is solved consistently by uniform incrementation. This treatment is usually sufficient from the practical point of view, but a consistent high-order approach, that would utilize additional degrees of freedom in temperatures within the hydrodynamical scheme, is one of the possible topics of future research.

5.1 BGK non-local transport model

Section 1 introduced the equations of laser plasma hydrodynamics (1), (2), (5), (6), but the closure for non-local heat fluxes of electrons $\vec{q}_e$, ions $\vec{q}_i$ and radiation $\vec{q}_R$ has not been given yet. The aim of this section is to give a description of the BGK non-local transport model [9], which provides these terms and closes the system of equations.

The primary physical quantity used in the non-local transport model are *radiation specific intensity* $I_R^\nu = I_R^\nu(t,\vec{x},\vec{n},\nu)$, *electron specific intensity* $I_e^{|\vec{v}|} = I_e^{|\vec{v}|}(t,\vec{x},\vec{n},|\vec{v}|)$ and *ion specific intensity* $I_i^{|\vec{v}|} = I_i^{|\vec{v}|}(t,\vec{x},\vec{n},|\vec{v}|)$ given for particles at time t, position $\vec{x}$ in direction given by the unit vector $\vec{n}$ with frequency ν or non-relativistic velocity $\vec{v}$. In fact, the specific intensities can be seen as an infinitesimal amount of energy $\mathrm{d}E$ transported by the species with frequencies in the interval $(\nu, \nu+\mathrm{d}\nu)$ or velocities in $(|\vec{v}|, |\vec{v}|+\mathrm{d}|\vec{v}|)$ in the time interval $\mathrm{d}t$, across the oriented surface element $\mathrm{d}\vec{S}$ into the solid angle $\mathrm{d}\omega$ around the direction $\vec{n}$:

$$\mathrm{d}E_R = I_R^\nu(t,\vec{x},\vec{n},\nu)\vec{n}\cdot\mathrm{d}\vec{S}\,\mathrm{d}\omega\,\mathrm{d}t\,\mathrm{d}\nu\ , \tag{162}$$

$$\mathrm{d}E_e = I_e^{|\vec{v}|}(t,\vec{x},\vec{n},|\vec{v}|)\vec{n}\cdot\mathrm{d}\vec{S}\,\mathrm{d}\omega\,\mathrm{d}t\,\mathrm{d}|\vec{v}|\ , \tag{163}$$

$$\mathrm{d}E_i = I_i^{|\vec{v}|}(t,\vec{x},\vec{n},|\vec{v}|)\vec{n}\cdot\mathrm{d}\vec{S}\,\mathrm{d}\omega\,\mathrm{d}t\,\mathrm{d}|\vec{v}|\ . \tag{164}$$

Equivalently, the specific intensities can be derived from their respective particle distributions $f_R(t,\vec{x},\vec{n},\nu)$, $f_e(t,\vec{x},\vec{n},|\vec{v}|)$ and $f_i(t,\vec{x},\vec{n},|\vec{v}|)$ in the phase space of spatial coordinates $\vec{x}$ and momentum $\vec{p}$ as follows ($(\vec{x},\vec{p}) = (\vec{x},\vec{n},|\vec{v}|)$):

$$\frac{I_R^\nu(t,\vec{x},\vec{n},\nu)}{h\nu c} = f_R(t,\vec{x},\vec{p})\,\mathrm{d}\vec{x}\,\mathrm{d}\vec{p} = \frac{h^3\nu^2}{c^3} f_R(t,\vec{x},\vec{n},\nu)\,\mathrm{d}\vec{x}\,\mathrm{d}\omega\,\mathrm{d}\nu\ , \tag{165}$$

$$\frac{I_e^{|\vec{v}|}(t,\vec{x},\vec{n},\nu)}{|\vec{v}|\,\frac{m_e}{2}|\vec{v}|^2} = f_e(t,\vec{x},\vec{p})\,\mathrm{d}\vec{x}\,\mathrm{d}\vec{p} = |\vec{v}|^2 f_e(t,\vec{x},\vec{n},|\vec{v}|)\,\mathrm{d}\vec{x}\,\mathrm{d}\omega\,\mathrm{d}|\vec{v}|\ , \tag{166}$$

$$\frac{I_i^{|\vec{v}|}(t,\vec{x},\vec{n},\nu)}{|\vec{v}|\,\frac{m_i}{2}|\vec{v}|^2} = f_i(t,\vec{x},\vec{p})\,\mathrm{d}\vec{x}\,\mathrm{d}\vec{p} = |\vec{v}|^2 f_i(t,\vec{x},\vec{n},|\vec{v}|)\,\mathrm{d}\vec{x}\,\mathrm{d}\omega\,\mathrm{d}|\vec{v}|\ . \tag{167}$$

This expressions explain the relation of the specific intensities to the classical kinetic theory and the second moment of the distributions in electron/ion velocities and the first moment in photon frequencies. As can be observed, all species are treated completely equally from the theoretical point of view and this fact allows construction of a single versatile numerical scheme. The equations for the specific intensities of electrons

and ions are then derived from the BGK kinetic equations [9]:

$$\frac{\partial f_e}{\partial t} + \vec{v}\cdot\nabla_{\vec{x}} f_e + \frac{q_e}{m_e}\vec{E}\cdot\nabla_{\vec{v}} = \frac{n_i}{n_e}\frac{\partial Z}{\partial t} S_e + \nu_{ei}^{|\vec{v}|}(S_e^{|\vec{v}|} - f_e) + \nu_{\sigma_e}^{|\vec{v}|}(\bar{f}_e - f_e) \ , \tag{168}$$

$$\frac{\partial f_i}{\partial t} + \vec{v}\cdot\nabla_{\vec{x}} f_i + \frac{q_i}{m_i}\vec{E}\cdot\nabla_{\vec{v}} = \nu_{ii}^{|\vec{v}|}(S_i^{|\vec{v}|} - f_i) \ , \tag{169}$$

where electric field $\vec{E}$, electron and ion source functions $S_e^{|\vec{v}|}$ and $S_i^{|\vec{v}|}$, electron–ion scattering collision frequency $\nu_{ei}^{|\vec{v}|}$, electron–electron scattering collision frequency $\nu_{\sigma_e}^{|\vec{v}|}$, ion–ion scattering collision frequency $\nu_{ii}^{|\vec{v}|}$, electron and ion charges q_e, q_i have been added. The symbol $\bar{f}_e$ represents in this context angular mean of the distribution f_e, i.e. $\bar{f}_e = \frac{1}{4\pi}\int_{4\pi} f_e \,\mathrm{d}\omega$. Substituting the specific intensity definitions (165–167) into (168), (169), the equations of transport expressed in terms of specific intensities are obtained in similar form to the radiation transport equation:

$$\frac{1}{c}\frac{\partial I_R^\nu}{\partial t} + \vec{n}\cdot\nabla_{\vec{x}} I_R^\nu = k_R^\nu(I_{S_R}^\nu - I_R^\nu) + \sigma_R^\nu(\bar{I}_R^\nu - I_R^\nu) \ , \tag{170}$$

$$\begin{aligned}\frac{1}{|\vec{v}|}\frac{\partial I_e^{|\vec{v}|}}{\partial t} + \vec{n}\cdot\nabla_{\vec{x}} I_e^{|\vec{v}|} = {} & \frac{q_e}{m_e}\vec{n}\cdot\vec{E}(5|\vec{v}|^{-1}\, I_e^{|\vec{v}|}) + \frac{1}{|\vec{v}|}\frac{n_i}{n_e}\frac{\partial Z}{\partial t} I_{S_e}^{|\vec{v}|} + \\ & + k_e^{|\vec{v}|}(I_{S_e}^{|\vec{v}|} - I_e^{|\vec{v}|}) + \sigma_e^{|\vec{v}|}(\bar{I}_e^{|\vec{v}|} - I_e^{|\vec{v}|}) \ ,\end{aligned} \tag{171}$$

$$\frac{1}{|\vec{v}|}\frac{\partial I_i^{|\vec{v}|}}{\partial t} + \vec{n}\cdot\nabla_{\vec{x}} I_i^{|\vec{v}|} = \frac{q_i}{m_i}\vec{n}\cdot\vec{E}(5|\vec{v}|^{-1}\, I_i^{|\vec{v}|}) + k_i^{|\vec{v}|}(I_{S_i}^{|\vec{v}|} - I_i^{|\vec{v}|}) \ , \tag{172}$$

where the opacity k_R^ν, extinction coefficients for electrons $k_e^{|\vec{v}|}$ and ions $k_i^{|\vec{v}|}$ were introduced, that are related to the collision frequencies as $k_e^{|\vec{v}|} = \nu_{ei}^{|\vec{v}|}/|\vec{v}|$, $k_i^{|\vec{v}|} = \nu_{ii}^{|\vec{v}|}/|\vec{v}|$. Similarly, the scattering coefficients for radiation σ_R^ν and electrons $\sigma_e^{|\vec{v}|} = \nu_{ee}^{|\vec{v}|}/|\vec{v}|$ were added. Moreover, there are the specific intensity source functions for radiation $I_{S_R}^\nu$, electrons $I_{S_e}^{|\vec{v}|}$ and ions $I_{S_i}^{|\vec{v}|}$. The angular mean of the specific intensity of radiation is $\bar{I}_R^\nu$ and electrons $\bar{I}_e^{|\vec{v}|}$.

The equations (170–172) present a kinetic problem in the full phase spaces $(\vec{x}, \vec{n}, \nu)$ and $(\vec{x}, \vec{n}, |\vec{v}|)$ respectively and hence the equations have 7 dimensions in general. Solution of the full 7D kinetic equations is enormously computationally expensive and is typically performed only for specific tasks in specialised kinetic codes [1, 57]. However, time scales of hydrodynamical codes are usually considerably larger than time scales of dynamics of the transported species $\Delta t \gg L/c$, $\Delta t \gg L/v_{Te}$, $\Delta t \gg 1/\omega_{pe}$, $\Delta t \gg L/v_{Ti}$, $\Delta t \gg 1/\omega_{pi}$, where L is a typical spatial scale, and stationary approximation is then sufficient. At this point, it must be stressed that mainly super-thermal species contribute to the energy transport, weakening the given requirements [61]. Moreover, the full spectra of the species are simplified to one energy group approximation and isotropic scattering is neglected in 1D, because non-diffusive radiation transport regime is of the main interest [62, 102]. When stationary electric fields are not taken into account consistently with the quasi-neutrality closure of hydrodynamics, the equations

are then reduced to the conveniently simple form:

$$\vec{n} \cdot \nabla I_R = k_R (I_{S_R} - I_R) \ , \tag{173}$$

$$\vec{n} \cdot \nabla I_e = k_e (I_{S_e} - I_e) \ , \tag{174}$$

$$\vec{n} \cdot \nabla I_i = k_i (I_{S_i} - I_i) \ , \tag{175}$$

where I_R, I_e and I_i are *total intensities* defined as:

$$I_R(t, \vec{x}, \vec{n}) = \int_0^\infty I_R^\nu(t, \vec{x}, \vec{n}, \nu) \, \mathrm{d}\nu \ , \tag{176}$$

$$I_e(t, \vec{x}, \vec{n}) = \int_0^\infty I_e^{|\vec{v}|}(t, \vec{x}, \vec{n}, |\vec{v}|) \, \mathrm{d}|\vec{v}| \ , \tag{177}$$

$$I_i(t, \vec{x}, \vec{n}) = \int_0^\infty I_e^{|\vec{v}|}(t, \vec{x}, \vec{n}, |\vec{v}|) \, \mathrm{d}|\vec{v}| \ . \tag{178}$$

The other terms $k_R, k_e, k_i, I_{S_R}, I_{S_e}, I_{S_i}$ were obtained by proper averaging of their spectral analogues $k_R^\nu, k_e^{|\vec{v}|}, k_i^{|\vec{v}|}, I_{S_R}^\nu, I_{S_e}^{|\vec{v}|}, I_{S_i}^{|\vec{v}|}$ respectively. However, the full inference of the transport model from the Boltzmann equation with BGK collision operator and radiation transport equation is out of the scope of this text and can be found in [9].

The equations (173–175) then present only a 3D problem for the specific intensities in 1D hydrodynamical approximation, because the time coordinate is included only parametrically in the equations. However, it must be noticed that all terms on the right hand side are temperature dependent and hence the temporal domain appears within the coupling with the hydrodynamic system through the equations of energy (5), (6), that are solved implicitly in temperatures according to section 5.2.

The mean Planck opacities k_R are calculated from scaling laws according to [103] and are not detailed here. Although, the mean extinction coefficients were introduced for electrons in section 3.5 and for ions in section 3.8. The intensity source function for radiation originate from the *gray body* approximation governed by *Stefan–Boltzmann law* σT_R^4, where the temperature of radiation is set $T_R = T_e$. *Maxwell–Boltzmann* distributions are assumed to be the source functions of electrons and ions with respective temperatures. The intensity source functions are then defined as follows:

$$I_{S_R} = \frac{\sigma}{\pi} T_e^4 \ , \tag{179}$$

$$I_{S_e} = n_e \frac{\sqrt{2}}{\sqrt{m_e}} \left(\frac{k_B}{\pi} \right)^{3/2} T_e^{3/2} \ , \tag{180}$$

$$I_{S_i} = n_i \frac{\sqrt{2}}{\sqrt{m_i}} \left(\frac{k_B}{\pi} \right)^{3/2} T_i^{3/2} \ . \tag{181}$$

Finally, the non-local heat fluxes defining the closure of the laser plasma hydro-

dynamical model presented in section 1 are defined as:

$$\vec{q}_R = \int_{4\pi} \vec{n} I_R \,\mathrm{d}\omega \ , \tag{182}$$

$$\vec{q}_e = \int_{4\pi} \vec{n} I_e \,\mathrm{d}\omega \ , \tag{183}$$

$$\vec{q}_i = \int_{4\pi} \vec{n} I_i \,\mathrm{d}\omega \ . \tag{184}$$

The fluxes are substituted in this form into the equations (5), (6) and complete equations of conservation of energy for non-local transport hydrodynamics are obtained:

$$\rho \frac{\partial \varepsilon_e}{\partial t} = -p_e \nabla \cdot \vec{u} + G_{ei}(T_i - T_e) - \int_{4\pi} \vec{n} \cdot \nabla (I_e + I_R) \,\mathrm{d}\omega - \nabla \cdot \vec{S} \ , \tag{185}$$

$$\rho \frac{\partial \varepsilon_i}{\partial t} = -p_i \nabla \cdot \vec{u} + G_{ie}(T_e - T_i) - \int_{4\pi} \vec{n} \cdot \nabla I_i \,\mathrm{d}\omega \ . \tag{186}$$

However, several remarks considering this procedure must be given. The reasonable assumptions $c \gg \vec{u}, |\vec{v}| \gg |\vec{u}|$ were made for the transported species and hence there are no convective terms originating from the transition between the laboratory and the fluid related frame. In other words, the functions of non-local transport in Eulerian coordinates are identified with their Lagrangian analogues.

Another note regards the fact that only energy equations are modified by the non-local transport model, but other moments of the distribution functions are not coupled with the equations of two-temperature hydrodynamics (1–4). This simplification follows the approximation of non-viscous fluid and stability considerations together with conservation properties of the scheme. Also the radiation pressure is usually significantly lower than the thermal pressure in hydrodynamic simulations [22]. However, it can be observed that the equations (185), (186) are fully energy conservative thanks to the formulation of the transport in terms of the specific intensities, that is one of the important advantages of the model.

In order to conclude this section, it must be noted that the BGK model, despite its simplicity, allows integration of larger number of terms into the hydrodynamic equations as proposed in [9], but their physical justification, implementation and appropriate physical closure models are one of the possible topics of the future research. One of the perspective approaches is the *multi-group* transport, that separates the transported species into different energy groups, increasing the accuracy of the averaged transport coefficients, that can be eventually obtained from the *atomic codes* [104, 105].

5.2 Finite element scheme

The previous section (5.1) introduced the BGK non-local transport model making the closure of the equations of non-local laser plasma hydrodynamics (1), (2) and (185), (186). This section aims to derive appropriate numerical scheme for solution of the transport model utilizing the *Finite Element Method* (FEM) [106, 107]. The beneficial property of this approach is the possibility of application of arbitrarily high order

elements thanks to the abstract nature of the description. In particular, *Discontinuous Galerkin* finite elements are employed, that provide a feasible option for solution of advection problems [108, 109] and computational efficiency [110]. The implementation in the simulation code PETE uses highly scalable MFEM library [111].

In order to summarize the governing system of equations that are solved numerically, it must be recalled that solely hydrodynamical part of the equations (1–4) is solved explicitly. Diffusion and electron–ion heat exchange are eventually solved separately due to operator splitting technique as discussed in section 1.1. The laser absorption acts as an explicit energy source, but it can be integrated together with the hydrodynamical part or in the finite element scheme according to section 2.1.2. Hence, the term $\nabla \cdot \vec{S}$ appears later in the construction as an explicit term. Similarly to the diffusion scheme, the non-local transport numerical scheme is also incorporated by application of the operator splitting method, solving the modified equations (185) and (186):

$$\rho \left(\frac{\partial \varepsilon_e}{\partial T_e} \right)_\rho \left(\frac{\partial T_e}{\partial t} \right)_{split} = G_{ei}(T_i - T_e) - \int_{4\pi} \vec{n} \cdot \nabla (I_e + I_R) \, \mathrm{d}\omega - \nabla \cdot \vec{S} \ , \tag{187}$$

$$\rho \left(\frac{\partial \varepsilon_i}{\partial T_i} \right)_\rho \left(\frac{\partial T_i}{\partial t} \right)_{split} = G_{ie}(T_e - T_i) - \int_{4\pi} \vec{n} \cdot \nabla I_i \, \mathrm{d}\omega \ . \tag{188}$$

In this form, the system of equations is still incomplete and the proper non-local closure model must be provided. Thanks to the unified treatment of the transported species, the equations for specific intensities (173–175) can be rewritten into the general form of transport equation for purposes of numerical solution:

$$\vec{n} \cdot \nabla I = k_I (S - I) \ , \tag{189}$$

where the specific intensity I can be identified with one of the intensities I_R, I_e or I_i. The general source function S replaces I_{S_R}, I_{S_e} or I_{S_i} and k_I stand for k_R, k_e or k_i.

Together, the equations (187–189) formulate the *non-local transport coupled problem*, coupling the local evolution of temperature with fluxes of transported species. Mathematically, the problem consists of the closed system of differential equations non-linear in temperatures, since the coefficients $(\partial \varepsilon_e / \partial T_e)_\rho$, $(\partial \varepsilon_i / \partial T_i)_\rho$, $G_{ei} = G_{ie}$, κ and the source function S are all non-linear functions of temperature(s) in general. Plausible simplification is then made similarly to the section 4 and the specific heats and the electron–ion energy exchange coefficients are assumed "frozen", i.e. constant throughout the computational time step. In addition, the extinction coefficient k_I is also taken constant in order to maintain linearity of equation (189) in terms of the unknowns of the system. The transport equation (189) is then linearised in temperature as follows:

$$\vec{n} \cdot \nabla I = S_A T + S_b - k_I I \ , \tag{190}$$

where the temperature T corresponds to electron or ion temperature depending on the transported specie. The newly introduced coefficients S_A and S_b are also assumed constant during the time step. The equations (187), (188) and (190) then represent a

linear system in the temperatures T_e, T_i and the specific intensities I_R, I_e and I_i.

The linear non-local transport coupled problem is solved by the *Discontinuous Galerkin Bhatnagar–Gross–Krook Transport and Temperatures Scheme* (DG–BGK&TS) [9]. The discretization is performed in the temporal domain Δt, the spatial domain $\Omega_{\vec{x}}$ and the propagation directions domain $\Omega_{\vec{n}}$. The methods for transport of particles using discretization in directions are generally known as *discrete–ordinate* methods or S_N methods [97, 112, 110]. Another attribute that is usually given to this methods is *short-characteristics* methods, because the propagation is solved always locally between adjacent computational cells. The full inference of the scheme is out of scope of this text and can be found in [9], but a brief overview of it is given in order to show additional ion transport terms as well as the newly added laser absorption term and the temperature stabilization presented in section 5.2.1.

First of all, the proper domains for solution of the system must be defined. The temperature equations (187), (188) are solved on the global domain $\Omega_{t,\vec{x}} = \Delta t \times \Omega_{\vec{x}}$. In contrast, the transport equations (190) are solved on the higher dimensional domain $\Omega_{t,\vec{x},\vec{n}} = \Delta t \times \Omega_{\vec{x}} \times \Omega_{\vec{n}}$, that also includes the angular domain. The spatial discretization then divides the spatial domain $\Omega_{\vec{x}}$ into finite elements domains $\Omega^e_{\vec{x}}$ and the corresponding multi-dimensional domains are denoted similarly as $\Omega^e_{t,\vec{x}}$, $\Omega^e_{t,\vec{x},\vec{n}}$. All the element spatial domains are assumed to have Lipschitz boundary Γ with the normal $\vec{n}_\Gamma$.

The Sobolev functional spaces H^1 with zero and first derivative in the Hilbert space L^2 are defined on these domains. In particular, it is the global space H_I and element space H^e_I for the test and trial functions of the specific intensities I, the space H_{T_e} and $H^e_{T_e}$ for the electron temperatures functions and the space H_{T_i} and $H^e_{T_i}$ for the ion temperatures functions.

Application of *Galerkin variational* principal on the equations non-local transport coupled problem (187), (188), (190) yields:

$$\int_{\Omega_{t,\vec{x},\vec{n}}} \Psi \left(\vec{n} \cdot \nabla I + k_I I - (S_A T + S_b)\right) \mathrm{d}\Omega_{t,\vec{x},\vec{n}} = 0 \quad \forall \Psi \in H_I \ , \tag{191}$$

$$\int_{\Omega_{t,\vec{x}}} \Xi \left(a_e \frac{\mathrm{d}T_e}{\mathrm{d}t} - G_{ei}(T_i - T_e) + \int_{4\pi} \vec{n} \cdot \nabla (I_e + I_R) \, \mathrm{d}\omega \right) \mathrm{d}\Omega_{t,\vec{x}} = \\ = \int_{\Omega_{t,\vec{x}}} \Xi \left(-\nabla \cdot \vec{S} \right) \mathrm{d}\Omega_{t,\vec{x}} \quad \forall \Xi \in H_{T_e} \ , \tag{192}$$

$$\int_{\Omega_{t,\vec{x}}} \tilde{\Xi} \left(a_i \frac{\mathrm{d}T_i}{\mathrm{d}t} - G_{ie}(T_e - T_i) + \int_{4\pi} \vec{n} \cdot \nabla I_i \, \mathrm{d}\omega \right) \mathrm{d}\Omega_{t,\vec{x}} = 0 \quad \forall \tilde{\Xi} \in H_{T_i} \ , \tag{193}$$

where the coefficients $a_e = \rho(\partial \varepsilon_e / \partial T_e)_\rho$ and $a_i = \rho(\partial \varepsilon_i / \partial T_i)_\rho$ were introduced similarly to section 4. The time derivatives are written as ordinary derivatives, because the dependence on spatial coordinate appears in temperatures only parametrically in this *mixed formulation*.

The transport equation (191) is then rewritten into *discontinuous Galerkin vari-*

ational form on each of the elements:

$$\int_{\Omega^e_{t,\vec{x},\vec{n}}} \Psi \left(\vec{n}\cdot\nabla I + k_I I - (S_A T + S_b)\right) \mathrm{d}\Omega^e_{t,\vec{x},\vec{n}} = \\ = \int_{\Delta t}\int_{\Omega_{\vec{n}}}\int_{\Gamma_{\vec{n}\cdot\vec{n}_\Gamma<0}} \Psi\left((I-\tilde{I})\vec{n}\cdot\vec{n}_\Gamma\right)\mathrm{d}\Gamma\,\mathrm{d}\Omega_{\vec{n}}\,\mathrm{d}t \quad \forall\Psi\in H^e_I \ , \quad (194)$$

where *upwind numerical fluxes* are applied on the right hand side, inducing integration only over the part of the boundary Γ, where $\vec{n}\cdot\vec{n}_\Gamma < 0$ holds, i.e. the inflow of the numerical flux into the cell. The intensity $\tilde{I}$ then represents the intensity of the adjacent element.

The temperature equations (192), (193) are also rewritten to variational form on the separate elements $\Omega^e_{t,\vec{x}}$, but remain formally identical following the mixed formulation. The construction of the scheme then becomes clear, the transport equation (194) performs the non-local coupling between the temperature evolution equations on single elements. For given temperature, the transport equation (190) is completely time-less, forming an ordinary differential equation on the global spatial domain $\Omega_{\vec{x}}$. Hence, explicit upwind scheme can be employed. In contrast, the temperature evolution equations are solved completely locally on the domain $\Omega^e_{t,\vec{x}}$ using an implicit scheme in temperatures. However, the key feature of the DG–BGK&TS scheme resides in the local inclusion of the transport equation (194) into the local implicit scheme as will be shown later.

The whole transport model is implemented the 1D hydrodynamical simulation code PETE, but the scheme can be analogously extended to more dimensions. In 1D slab geometry, that is used in PETE, the equations (187), (188), (190) take the form:

$$\cos(\phi)\frac{\partial I}{\partial z} = -k_I I + S_A T + S_b \ , \quad (195)$$

$$a_e\frac{\mathrm{d}T_e}{\mathrm{d}t} + G_{ei}T_e + \int_0^{2\pi}\int_0^{\pi}\cos(\phi)\frac{\partial I_e + I_R}{\partial z}\sin(\phi)\,\mathrm{d}\phi\,\mathrm{d}\theta = G_{ei}T_i - \frac{\partial S_z}{\partial z} \ , \quad (196)$$

$$a_i\frac{\mathrm{d}T_i}{\mathrm{d}t} + G_{ie}T_i + \int_0^{2\pi}\int_0^{\pi}\cos(\phi)\frac{\partial I_i}{\partial z}\sin(\phi)\,\mathrm{d}\phi\,\mathrm{d}\theta = G_{ie}T_e \ , \quad (197)$$

where ϕ is the azimuthal angle and θ is the polar angle in the spherical coordinates $(\phi,\theta)\in\langle 0,\pi\rangle\times\langle 0,2\pi\rangle$ corresponding to the direction of propagation $\vec{n}$.

In order to proceed, the discrete functional basis must be defined. In particular, polynomial bases of given order are utilized in code PETE, but the general formulation of the problem allows even different choices of bases. The bases are ω_t, ω_θ, ω_ϕ for temporal domain, polar and azimuthal domain. It must be noted that these basis are global, i.e. identical for all spatial elements. In contrast, the bases for spatial domain $\Omega^e_{\vec{x}}$ are different for each element and discretized quantity. There is basis ψ for the specific intensities, ξ for the electron temperatures and $\tilde{\xi}$ for the ion temperatures. The interpolation bases are then produced as combinations of these bases:

$$\boldsymbol{\Psi} = \omega_t\otimes\omega_\theta\otimes\omega_\phi\otimes\psi \ , \quad \boldsymbol{\Xi} = \omega_t\otimes\xi \ , \quad \tilde{\boldsymbol{\Xi}} = \omega_t\otimes\tilde{\xi} \ . \quad (198)$$

The quantities appearing in (195–197) are discretized on the finite elements using the newly defined interpolations bases as follows:

$$I_{R/e/i}(t,\vec{x},\vec{n}(\theta,\phi)) = \boldsymbol{\Psi}^T(t,\theta,\phi,\vec{x})\cdot\mathbf{I}_{R/e/i}\ , \qquad T_e(t,\vec{x}) = \boldsymbol{\Xi}^T\cdot\mathbf{T}_e\ , \tag{199}$$

$$T_i(t,\vec{x}) = \tilde{\boldsymbol{\Xi}}^T\cdot\mathbf{T}_i\ , \qquad \frac{\partial S_z}{\partial z}(t,\vec{x}) = \boldsymbol{\Xi}^T\cdot\mathbf{div}\,\mathbf{S}\ . \tag{200}$$

It must be noted that the laser power deposition term is written symbolically as $\frac{\partial S_z}{\partial z}$ following the formulation of equation (196). The intensity discretization is identical for all specific intensities I_R, I_e and I_i.

Substitution of the discretized functions (200) back into the equations (195–197) in variational form analogues to (192–194) yields the *discrete variational* form in 1D slab geometry:

$$\int_{\Delta t}\int_0^{2\pi}\int_0^{\pi}\int_{\Delta z}\boldsymbol{\Psi}\otimes\left[\left(\cos(\phi)\,\frac{\partial\boldsymbol{\Psi}^T}{\partial z}\,k_I\boldsymbol{\Psi}^T\right)\mathbf{I}_{R/e} - S_A^{R/e}\boldsymbol{\Xi}^T\cdot\mathbf{T}_e - S_b^{R/e}\right]\mathrm{d}z\sin(\phi)\,\mathrm{d}\phi\,\mathrm{d}\theta\,\mathrm{d}t =$$
$$= \int_{\Delta t}\int_0^{2\pi}\int_0^{\pi}\int_{\Gamma_{\vec{n}\cdot\vec{n}_\Gamma<0}}\boldsymbol{\Psi}\otimes\left[\left(\boldsymbol{\Psi}^T\cdot\mathbf{I}_{R/e} - \boldsymbol{\Psi}^T\cdot\tilde{\mathbf{I}}_{R/e}\right)\cos(\phi)n_{\Gamma_z}\right]\mathrm{d}\Gamma_z\sin(\phi)\,\mathrm{d}\phi\,\mathrm{d}\theta\,\mathrm{d}t\ , \tag{201}$$

$$\int_{\Delta t}\int_0^{2\pi}\int_0^{\pi}\int_{\Delta z}\boldsymbol{\Psi}\otimes\left[\left(\cos(\phi)\,\frac{\partial\boldsymbol{\Psi}^T}{\partial z}\,k_I\boldsymbol{\Psi}^T\right)\mathbf{I}_i - S_A^i\tilde{\boldsymbol{\Xi}}^T\cdot\mathbf{T}_i - S_b^i\right]\mathrm{d}z\sin(\phi)\,\mathrm{d}\phi\,\mathrm{d}\theta\,\mathrm{d}t =$$
$$= \int_{\Delta t}\int_0^{2\pi}\int_0^{\pi}\int_{\Gamma_{\vec{n}\cdot\vec{n}_\Gamma<0}}\boldsymbol{\Psi}\otimes\left[\left(\boldsymbol{\Psi}^T\cdot\mathbf{I}_i - \boldsymbol{\Psi}^T\cdot\tilde{\mathbf{I}}_i\right)\cos(\phi)n_{\Gamma_z}\right]\mathrm{d}\Gamma_z\sin(\phi)\,\mathrm{d}\phi\,\mathrm{d}\theta\,\mathrm{d}t\ . \tag{202}$$

In 1D, the normal n_{Γ_z} of the element boundary Γ reduces to only two scalar values ($n_{\Gamma_z} = \pm 1$) depending on the orientation of the space. Consequently, the integration over the inflow part of the boundary $\Gamma_{\vec{n}\cdot\vec{n}_\Gamma<0}$ poses only selection of the left or right node in 1D. The coefficients S_A and S_b were specialised for each of the transported specie in the equations. The temperature evolution equations follows:

$$\int_{\Delta t}\int_{\Delta z}\boldsymbol{\Xi}\otimes\left[\left(a_e\,\frac{\mathrm{d}\boldsymbol{\Xi}^T}{\mathrm{d}t} + G_{ei}\boldsymbol{\Xi}^T\right)\cdot\mathbf{T}_e + \right.$$
$$\left. + \left(\int_0^{2\pi}\int_0^{\pi}\cos(\phi)\,\frac{\partial\boldsymbol{\Psi}^T}{\partial z}\sin(\phi)\,\mathrm{d}\phi\,\mathrm{d}\theta\right)\cdot(\mathbf{I}_R + \mathbf{I}_e)\right]\mathrm{d}z\,\mathrm{d}t =$$
$$= \int_{\Delta t}\int_{\Delta z}\boldsymbol{\Xi}\otimes\left[G_{ei}\tilde{\boldsymbol{\Xi}}^T\cdot\mathbf{T}_i - \boldsymbol{\Xi}^T\cdot\mathbf{div}\,\mathbf{S}\right]\mathrm{d}z\,\mathrm{d}t\ , \tag{203}$$

$$\int_{\Delta t}\int_{\Delta z} \tilde{\boldsymbol{\Xi}} \otimes \left[\left(a_i \frac{\mathrm{d}\tilde{\boldsymbol{\Xi}}^T}{\mathrm{d}t} + G_{ie}\tilde{\boldsymbol{\Xi}}^T \right) \cdot \mathbf{T}_i + \right.$$
$$\left. + \left(\int_0^{2\pi} \int_0^{\pi} \cos(\phi) \frac{\partial \boldsymbol{\Psi}^T}{\partial z} \sin(\phi)\, \mathrm{d}\phi\, \mathrm{d}\theta \right) \cdot \mathbf{I}_i \right] \mathrm{d}z\, \mathrm{d}t =$$
$$= \int_{\Delta t}\int_{\Delta z} \tilde{\boldsymbol{\Xi}} \otimes \left[G_{ie}\boldsymbol{\Xi}^T \cdot \mathbf{T}_e \right] \mathrm{d}z\, \mathrm{d}t \ . \quad (204)$$

Together, the equations (201–204) form a complete linear system of equations for discrete specific intensities $\mathbf{I}_R$, $\mathbf{I}_e$, $\mathbf{I}_i$ and temperatures $\mathbf{T}_e$ and $\mathbf{T}_i$. It is worth to recall that the term $\mathbf{div}\,\mathbf{S}$ is explicit and does not increase the number of unknowns. For fully discrete form of the system, we point the reader to [9], where all discrete matrices are properly constructed, and the inference of discrete form of the newly added terms for ion transport and laser absorption is analogous to construction of other terms. However, the key aspects of the discrete scheme must be mentioned. The DG–BGK&Ts scheme allows various time discretizations, but fully implicit, i.e. *backward Euler*, discretization is normally used. It offers high stability and low computational costs, because the scheme can be expressed only in terms of the discrete functions on the new time level $n+1$ (following the notation of the previous sections) and the quantities on the old time level n are explicitly known and can be directly substituted. This procedure effectively lowers the dimensions of the system and hence saves the computational resources.

The innovative idea behind the scheme is that the transport equations (201), (202) are locally substituted into the temperature evolution equations (203), (204) after the full discretization, where the discrete intensity is expressed in the form $\mathbf{I} = \mathbf{AT} + \mathbf{b}$ with a particular matrix $\mathbf{A}$ and vector $\mathbf{b}$ [9, 113, 114]. A complete system of linear equations for temperatures is then formed and solved locally. The discrete analogues of transport equations (201), (202) provide the non-local coupling between the elements on the global domain $\Omega_{\vec{x}}$.

Specifically in 1D slab geometry, the situation is very simple, the Dirichlet boundary condition on zero intensity $I(z_0) \equiv 0$ is applied in a cold solid, where no transport takes place. From the point of view of the ordinary differential equations in intensities formed by the transport equations with fixed temperatures (201), (202), the condition presents an initial condition. The spatial domain is then swept from z_0 to the opposite boundary z_{N_z}. During the sweep, the intensities inside the elements as well as the temperatures are (re)calculated on the time level $n+1$. When the vacuum boundary z_{N_z} is reached, reflective boundary condition is activated for electrons and ions, but zero source intensity for radiation as mentioned in the introduction of section 5, and a new sweep in opposite direction can start. This procedure is repeated several times until satisfactory convergence is reached. The relative change of internal energy is taken as the measure of the convergence in this case. The whole spatial configuration is depicted in Figure 16. However, it is worth to note that the situation becomes more complex when the spatial dimensions of the simulation are increased and finding proper ordering becomes non-trivial [115].

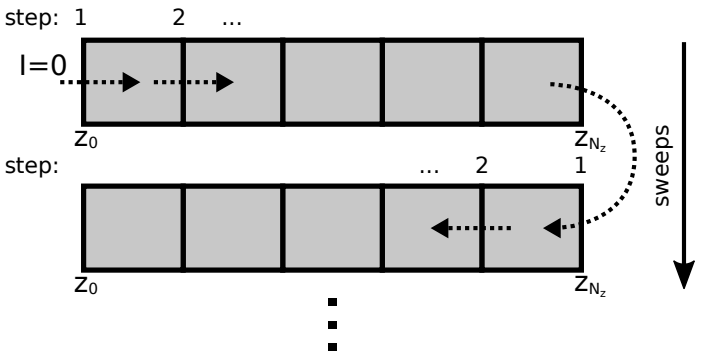

Figure 16: A schematic visualization of the computational sequence in 1D slab geometry.

5.2.1 Stabilised DG method

The numerical scheme presented in the previous section (5.2) is usually highly stable, but the coupling of the non-local transport scheme with the hydrodynamical scheme is performed through the mean values as mentioned in the introduction. This approach is sometimes not sufficient, especially, when the laser absorption is included in the model through the term $\mathbf{div}\,\mathbf{S}$. The degrees of freedom of the electron temperature $\mathbf{T}_e$ remain distorted after passing through the absorption area, where the elements undergo strong non-uniform heating. Even though the convergence in mean value is preserved and a corona is not usually of the main interest in the simulations, it is beneficial to stabilise the method. This problem is common to many DG schemes and hence the technique of *stabilised discontinuous elements* (SDG) has been developed [106, 107, 116]. In fact, it resides in introduction of additional terms including artificial diffusion. Here, we propose more physical setting, where classical thermal diffusion is used locally instead. Similarly to the section about heat diffusion (4), the diffusion operator of type $\nabla \cdot (\kappa_{SH} \nabla T_e)$ is considered. In variational form, the following holds after the Gauss theorem is applied:

$$\int_{\Omega_{t,\vec{x}}} \Xi(\nabla \cdot (\kappa_{SH} \nabla T_e))\,\mathrm{d}\Omega_{t,\vec{x}} = \int_{\Delta t} \int_{\Gamma} \kappa_{SH} \Xi(\vec{n}_\Gamma \cdot \nabla T_e)\,\mathrm{d}\Gamma\,\mathrm{d}t - \int_{\Omega_{t,\vec{x}}} \kappa_{SH} \nabla \Xi \cdot \nabla T_e\,\mathrm{d}\Omega_{t,\vec{x}}\ . \tag{205}$$

However, only the symmetrical part of the right hand side is used in order to eliminate linear functions from the kernel of the operator, because correction of slope of linear functions is also intended. Consequently, the term of corresponding to the diffusion is added to the left hand side of (203):

$$\alpha_{SDG} \kappa_{SH} \frac{\partial \boldsymbol{\Xi}}{\partial z} \otimes \frac{\partial \boldsymbol{\Xi}^T}{\partial z}\ , \tag{206}$$

where α_{SDG} is a constant typically chosen $\alpha_{SDG} \ll 1$ in order to preserve behaviour mainly driven by the transport equation.

Several remarks must be made. The mean value on the elements is preserved as can be observed for example by the assignment $\Xi \leftarrow 1$ in (205) without the asymmet-

rical term on the right hand side. That is in agreement with the fact that the method is meant only as a correction that should not perturb the convergence in mean values. The Spitzer-Härm heat conductivity defined in section 3.4 is applied to effectively allow the application of the correction only in hot plasma, because the coefficient is close to zero for low temperatures. The non-linearity of the heat conduction in temperature is also advantageous here for the same reason. However, the diffusion acts only in the interior of the elements, where distortion of values of temperature degrees of freedom may occur and the DG elements admit discontinuity of temperatures on the boundaries of the elements. The proposed term effectively solves this problem, but fine tuning of the multiplicative constant α_{SDG} is sometimes required depending on the given problem. A fully high-order scheme including the hydrodynamical part poses an elegant alternative and it is one of the possible topics of future research as mentioned in the introduction of section 5.

6 Numerical simulations

This section presents the results of the numerical simulations performed with the 1D simulation codes PETE and 2D code PALE2. An extensive comparison is made between different physical models and numerical methods in order to show various aspects of the methods. It includes the classical thermal diffusion model reviewed in section 4, that is present in both codes, and also the state-of-art non-local transport model for radiation, electrons and ions described in section 5, that is specific for code PETE. Moreover 1D and 2D simulations were performed to show the effects of higher dimensional treatment of the problem. Finally, the results are validated by a comparison with literature.

In order to achieve full comparability of the results, a single experimental scenario from [117] has been chosen. The authors present results of numerical experiments for pre-pulse of 100 TW LULI laser system, that are supported by measured values of partial ionization. The calculations of detailed distributions of ion species and resulting average ionizations were obtained by postprocessing of the results of hydrodynamical simulations. Moreover, the achieved results with the simulation code CHIVAS are discussed with respect to the other codes, MULTI [118] and FILM [119]. It must be stressed that the codes CHIVAS and MULTI have incorporated radiation transport model, making them ideal candidates for full comparison with our radiation transport model. However, the hydrodynamical codes are also enhanced by atomic physics codes that are not integrated in the codes PETE and PALE2, but the results with several equations of state are compared here instead.

The pre-plasma was created in the experiment by irradiation of an aluminium target by 600 ps long laser pulse with wavelength $\lambda_0 = 0.53$ μm. The temporal profile is approximated by a Gaussian pulse with peak intensity $I_{laser} = 5 \cdot 10^{13}$ W/cm^2, where the temporal width (FWHM) of the pulse is taken as one half of the full length, i.e. $t_{FWHM} = 300$ ps. The maximum peak offset is equally set $t_{offset} = 300$ ps. The spatial profile of the pulse is not fully detailed in the paper and only 1D simulations were performed there. Therefore, a Gaussian spatial pulse shape is used here for simplicity and the spot diameter (FWHM) is set $d_{FWHM} = 280$ μm in according to the paper.

The geometry of the computational mesh was also unified in all simulations in order to attain maximal comparability. The 1D simulations used single geometrical mesh spreading from $z_0 = -100$ μm to $z_{N_z} = 0$ μm with $N_z = 300$ cells and geometrical factor $C_g = 0.97$. The geometrical factor of the mesh increases its density in the ablation area, setting the volume ratio of each two consequent computational cells:

$$z_j \;\; = z_0 + (z_{N_z} - z_0)\frac{C_g^j - 1}{C_g^{N_z} - 1} \qquad j \in \{1, \ldots, N_z - 1\} \; . \tag{207}$$

The orders of polynomial bases were set: 2nd for electron temperatures, 0th for ion temperatures, 3rd for specific intensities and the azimuthal angle ϕ and 0th for the polar angle θ. The selection of the values follows the considerations that electron dynamics is the more dramatic than dynamics of ions as can be observed later. The intensities form numerical fluxes in the mixed formulation (195–197) and the order

of the polynomials is lowered by the divergence operator in the contribution to the energy equations. Hence, the order of the intensity polynomials is increased by one to maintain compatibility of the bases. Finally, the polar angle variation is eliminated totally following the 1D symmetry in code PETE, i.e. polar isotropy of the transport.

The 2D simulation code PALE2 has been configured to use cylindrical geometry with the computational mesh $\langle r_0, r_{N_r}\rangle \times \langle z_0, z_{N_z}\rangle = \langle 0, 500\rangle \times \langle -50, 0\rangle$ in microns. The number of cells was $N_r = 80$ in radial direction and $N_z = 140$ in axial, where geometrical factors were set 0.95 and 1.03 respectively. The *indirect ALE* method was used with the Eulerian part (consisting of mesh rezoning and remapping of all quantities from the Lagrangian to the rezoned mesh) performed after each 25 Lagrangian time steps. This approach maintains sufficiently regular computational mesh for the laser absorption algorithm. Rezoning boundary condition was set to apply mirroring of the nodes on the central axis $r = 0$ and the outer surface $r = r_{N_r}$, allowing free sliding of the of the mesh in z axis. In contrast, the top and bottom boundaries used convex combination of 0.2 rezoned position and 0.8 Lagrangian positions of the nodes to keep the evolution maximally physically realistic, but allow minor smoothing to avoid creation of non-convex cells. Rezoning itself used *Winslow smoothing* of the computational mesh [120, 121].

Both codes used primarily interpolated QEOS equation of state to improve the comparability of the results, although QEOS is not normally available in PETE, but the interpolation tables were manually transferred between the codes. Other equations of state were also tested, but QEOS offers remarkable reliability from the point of view of hydrodynamical simulations, because it smoothly models an extensive range of densities and temperatures and also the results are in reasonable agreement with the reference profiles as shown on the following pages.

6.1 1D simulations

The first set of plots in Figure 17 compares the results computed by the 1D simulation code PETE with non-local transport of electrons and ions and classical heat diffusion approximation with the reference data from [117]. Several key aspects distinguishing both approaches can be clearly observed there. The non-local transport leads to higher temperatures in the corona, because the heat fluxes are significantly lower mainly in the early phases of the simulation as shown in Figure 18. The energy is not equally strongly transferred from the vicinity of critical plane, where most of the laser energy is deposited, to the cold material of the target. This *flux inhibition* leads to decreasing of the ablation rate and recession rate of the surface and consequently to lower coronal densities. On the other hand, the diffusion launches non-linear heatwave at the beginning of the simulation, heating the upstream of the laser ablation wave significantly more effectively. However, the heat flux is enormous and its non-physically large value must be strongly penalized by the heat flux limiter as will be discussed later. Also the diffusion maintain high values of the heat flux in the most of the corona leading to *temperature saturation* unlike the non-local transport model, that shows more rapid decrease of the temperatures in corona. An interesting observation can be made that the non-local transport allows penetration of (nearly) solid material unlike the

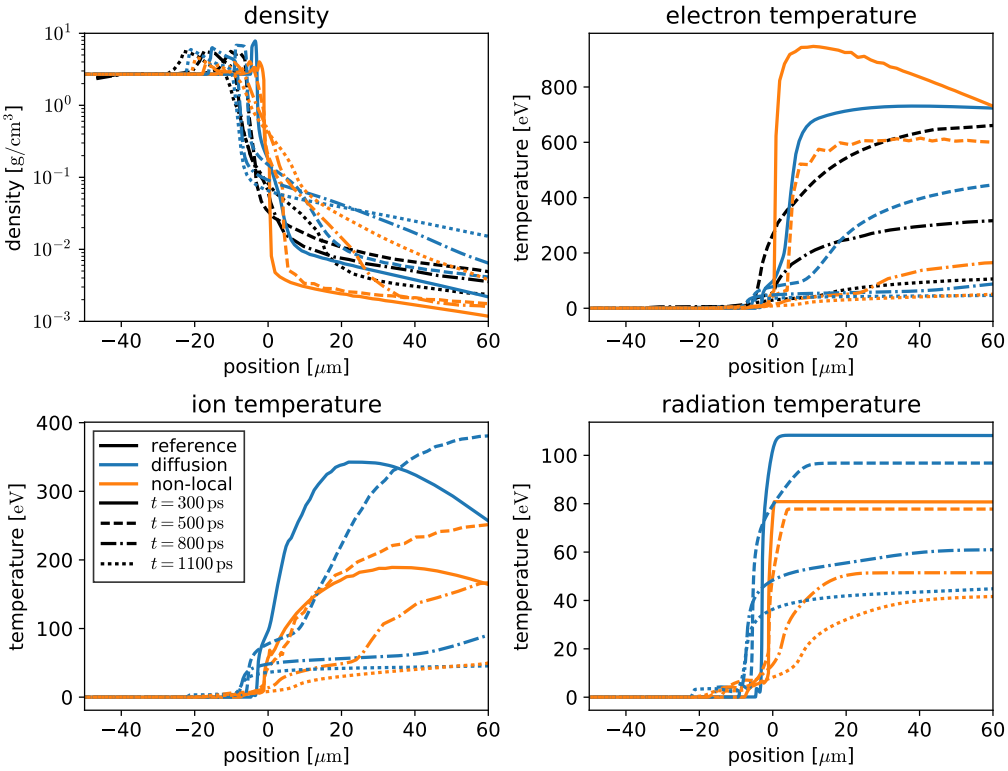

Figure 17: The density and temperature profiles at different times according to the reference [117] (*reference*), obtained from simulations with heat diffusion of electrons and ions with radiation transport (*diffusion*) and non-local transport of electrons and ions also with radiation transport (*non-local*).

heat diffusion that mainly acts in the expanded matter. This effect originates directly from the non-local nature of the transport, where the diffusion approximation by the dependence only on the local gradient of temperature is not sufficient.

The ion temperatures behave oppositely to the electron ones. The reason of this phenomena can be explained mostly by the typical decreasing dependency of the electron–ion collision frequencies as shown in section 3. Ion temperature is driven by the exchange of energy with electrons, because the energy equation of ions (5) is mostly dominated by this source term in corona, since the pressure declines rapidly there and ion heat transfer is conservative and hence does not act as a source in the global sense. However, ions do not redistribute the energy even locally by the diffusion or the non-local transport. The values of ion heat flux are minuscule compared to the electron ones. The ineffectiveness of the transport mainly due to prohibitively small values of the mean free path also leads to deformations of the profiles of the heat flux. Ions are not able to converge to a self-similar solution in the form of non-linear heatwave, because of the strong coupling with electrons and insufficient heat transport.

From the quantitative point of view, the most important transport mechanism is

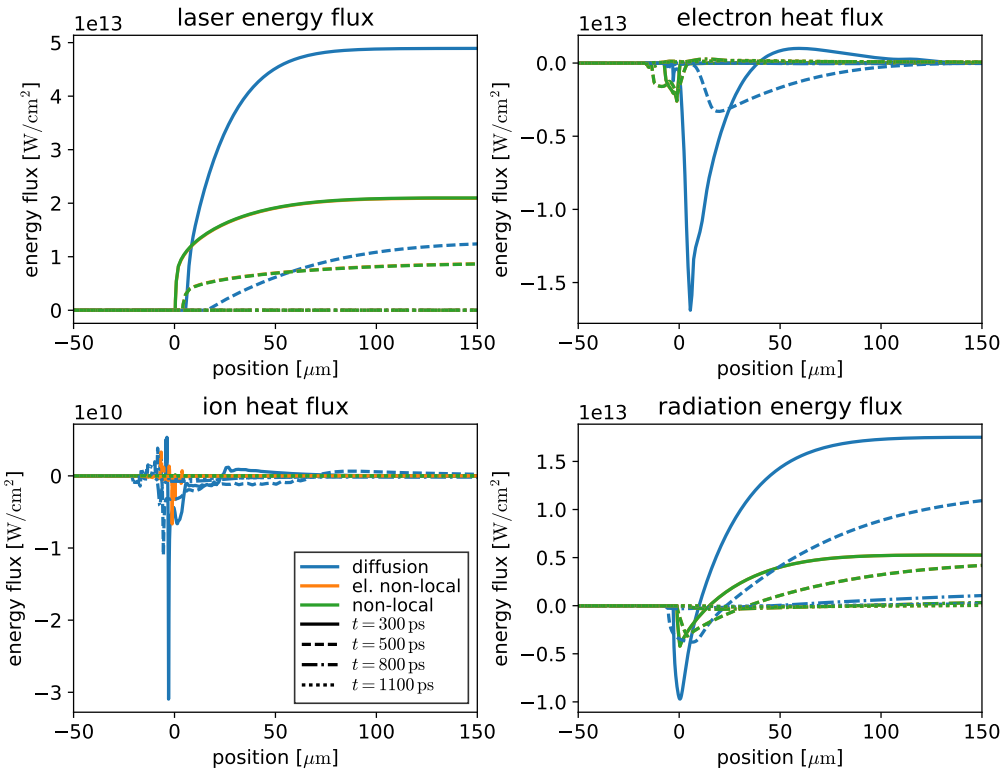

Figure 18: The energy fluxes at different times of the simulations with full thermal diffusion (*diffusion*), electron non-local transport and ion diffusion (*el. non-local*) and fully non-local transport (*non-local*). All simulations were performed with active radiation transport. Note that laser energy flux is not oriented unlike the rest of the fluxes, since its orientation towards the target does not change. Also the simulations *el. non-local* and *non-local* differs only gently and the profiles are almost identical in most plots.

the radiation transport. The radiation flux easily reaches more than one third of the absorbed laser intensity, although the Aluminium can be considered only moderate-Z material and not high-Z material, that are known to be especially strong emitters of thermal radiation [99]. The radiation crosses the conduction zone and it is absorbed there, but re-emission of the radiation follows. Hence, the mechanism smoothly deposits energy in the colder matter, altering the hydrodynamical expansion in the process and deforming the density profiles consequently. This phenomenon is known as *double ablation front* [100, 101]. Its most apparent effect is that slope of the density profile is flattened to some degree in the conduction zone, i.e. approximately between the laser ablation front and head of the rarefaction wave. In contrast, the radiation transport unlike the other transport mechanisms maintains enormous outward pointing energy fluxes in corona leading to strong *radiation cooling* effect. The confined energy in the system is dissipated rapidly. When the laser intensity lowers after the

maximum at 300 ps, the proportion of the radiation flux to the absorbed laser intensity increases leading to alteration of the energy balance in the plasma. Moreover, it can be noticed that the corona is almost totally transparent for the radiation and hence the radiation temperature is close to complete saturation there. Emission of radiation takes place there due to high electron temperatures, but the radiation freely crosses the area, because the opacity drops there for the same reason.

The laser absorption is strongly affected by the chosen transport model and hence the differences between the resulting profiles are even more pronounced. This effect occurs, because the reflectivity of the critical plane is closely connected with the gradients of the thermodynamic quantities in the vicinity of the critical plane as can be seen in the definition of complex permittivity (16).

The comparison with the reference data in Figure 17 reveals that the shape of the density and temperature profiles better suits the simulations performed with the diffusion model. The positions of the shock wave are almost identical for example and the densities in the corona at early times almost coincide. That is in an agreement with the fact that thermal diffusion was also used in the paper [117]. However, application of the diffusion approximation is mostly not physically justified, because the electron Knudsen number is about $\approx 10^2$ in the corona as shown in Figure 19. Also the values in the conduction zone are only moderate and cannot be considered fully sufficient for the diffusion. From this point of view, our non-local transport model is superior, because the restriction on the value of the Knudsen number is not present and the model is supposed to work in the diffusion regime as well as in the non-local transport regime. The discussion of the differences of the non-local transport model and the diffusion model then also holds for the reference profiles almost fully.

More questions arise about the radiation transport model, that is most likely responsible for the rapid decrease of the temperatures in the later phases of the simulation. In the discussion in the paper [117], the authors also claim that other numerical codes reached even higher temperature in the late times of the simulation. That contraindicates the observed behaviour in our results that the electron temperature falls rapidly, even though they were comparable at earlier times. Moreover, the transport forms the double ablation front structure very early in our case. On the other hand, our radiation transport is fully non-local and the radiation diffusion codes may behave worse, because the radiation Knudsen number grows to the values $\gtrsim 1$ near the critical density as shown in Figure 19. However, the details about the used model are not present in the paper. One of the deficiencies of code PETE is usage of only Planck opacities approximated by the scaling laws. Usage of Rosseland opacities is more appropriate for the conduction zone with low Knudsen numbers [62] and also the validity of the scaling laws is limited and must be taken with a grain of salt. A revision of the radiation transport model is a prospect for future work.

The ion Knudsen number shows that ion transport regime does not reach fully free streaming limit even in the corona. Hence, the diffusion transport is well-justified. Nevertheless, the non-local ion transport model is also applicable, but heat flux inhibition is significant also in this case as discussed earlier. The by-product of the evaluation of the Knudsen numbers is that it reveals minor deformations of the temperatures, when the full non-local transport model is employed. The ion transport is

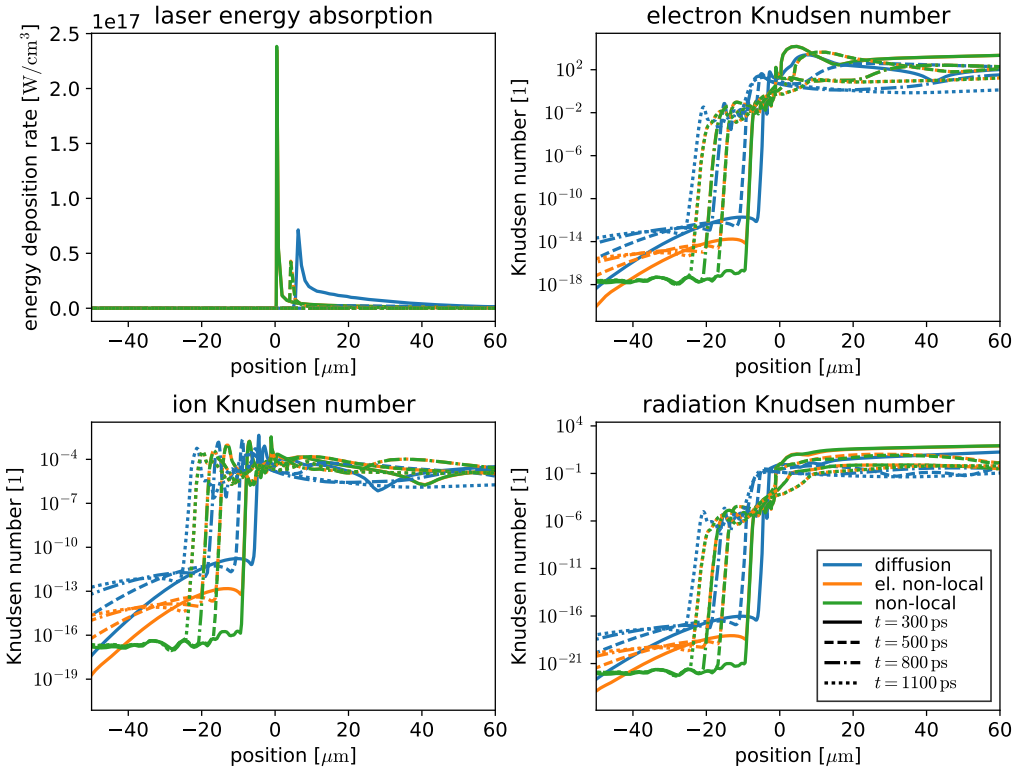

Figure 19: The Knudsen numbers of transported species and laser energy volumetric deposition rate at different times of the simulations with full thermal diffusion (*diffusion*), electron non-local transport and ion diffusion (*el. non-local*) and fully non-local transport (*non-local*). All simulations were performed with active radiation transport. Note that the simulations *el. non-local* and *non-local* differs only gently and the profiles are almost identical in most plots.

negligible with heat fluxes $\sim 10^8$ W/cm^2 and is not able to smooth even small variations in temperature. The origin of the perturbations may not be even physical, but rather numerical and hence the diffusion model is preferred from the point of view of the stability of the simulation. The parabolic nature of the diffusion equations guarantees that local extremes cannot appear and entropy is monotonously increasing. However, overall effect of the ion heat transfer is minimal under given conditions.

The laser energy absorption profiles in Figure 19 explain the absorption by inverse Bremsstrahlung more clearly, where most of the power is absorbed in the vicinity of the critical density. However, it can be observed that the absorption algorithm described in section 2 gives not negligible values of absorbed energy even about 40 wavelengths from the critical density in some cases. One may also notice that the resulting profiles are very smooth, even though the stationary waves are typically forming during the absorption as shown in the section dedicated to the laser absorption (2). The waves are present also in this case, but the spatial scale of the hydrodynamical simulation is

considerably larger than the the laser wavelength λ_0 and therefore point projection is not used for the transition from the refined mesh on the main mesh (see section 2.1.1), but linear regression of the Poynting vector (laser energy flux) is made in the range of a single wavelength instead. This way only a small redistribution of energy takes place, but absorption is still globally conservative. The temporal evolution shows that the critical plane recedes after the peak intensity is reached, because the hydrodynamical balance causes prolongation of the rarefaction wave area as can be noticed from the density profiles in Figure 17. Another interesting phenomenon is that heat diffusion does not only smooths the temperature profile as shown before, but also the refraction profiles and consequently the laser absorption profile. This effect is sufficiently strong to almost totally smear out the absorption profile in the late phases of the simulation.

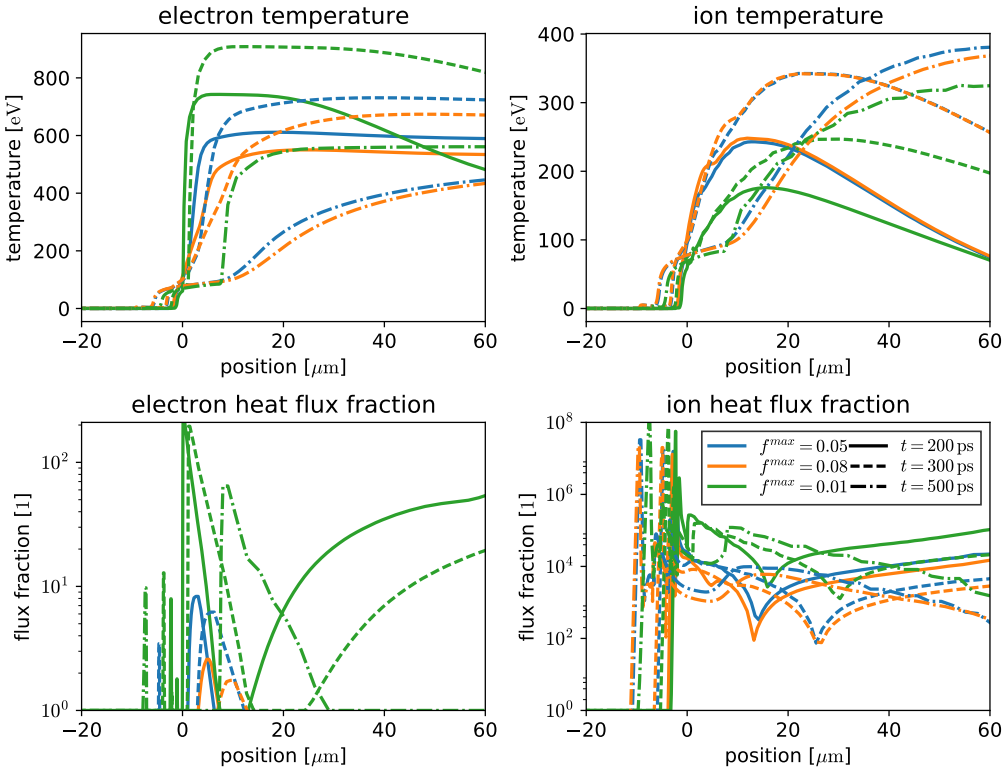

Figure 20: The temperatures and heat flux fractions (defined in section 4.3) at different times of the simulations with full thermal diffusion and radiation transport plotted for different heat limiter coefficients f^{max}.

In the previous discussion, heat flux limiting technique was mentioned in the context of the heat diffusion model, but a quantitative study of their effect on the simulation has not been made. The set of simulations presented in Figure 20 is dedicated to this purpose. The value of the heat flux limiter $f^{max} = 0.05$ has been used for all simulations performed so far and hence the corresponding profiles of other quantities can be found in the figures (17–19). The increased f^{max} allows higher values of heat

fluxes in fact, that lead to stronger diffusion of temperature. The temperature gradient in the vicinity of the critical plane is lower, because the thermal diffusion very effectively transports the energy to from the maximum laser absorption are further into upstream of the laser ablation front. In addition, the electron heat flux fraction shows that the conduction is almost unlimited except narrow area near the critical plane and hence total temperature saturation in the corona is unavoidable. Contrary, the lower value of f^{max} rises the the temperature gradient near the critical plane and leads to strong application of the flux limiter, where the flux fraction reaches even the second order of magnitude. In addition, flux limiter reduces the fluxes also in the corona, because of the density dependence of the W_e^{fs} in the definition (134), and the electron temperature starts falling down consequently. The ion temperatures are also shown, but their profile approximatively follows the behaviour of the electron temperature, because the ion heat transport is only subtle. Moreover, their heat fluxes are strongly limited by the heat flux limiter, because the flux fraction is about the fifth order of the magnitude. This effect is in agreement with the non-local transport model, where the directly computed values of fluxes were naturally extremely small as shown in Figure 18. The reasons for this behaviour can be seen in prohibitively small values of W_i^{fs} defined in (135) and large temperature gradients driven by electron dynamics and not ionic. However, it must be concluded that the chosen value $f^{max} = 0.05$ is in a good agreement with both simulations, the reference one and also the one with non-local transport, likewise the theoretical studies [68, 69].

Besides the value of the heat flux limiter coefficient, the flux limiting method itself plays a major role in the limiting and several different constructions were made in section 4.3. We divide the flux limiters to "direct", that modify the computed heat fluxes, and "indirect", that change the heat conductivities and the heat conduction step must be repeated. This classification is supported by the Figure 21, where both families of the limiters can be clearly distinguished based on their behaviour. It must be noted that the limiter $\kappa^{rescale}$ has been used so far and hence the complementary profiles can be found on the previous pages. The temperature profiles are very close to each other for all limiters, but the direct limiters exhibit peculiar effect near the critical plane. It originates from their basic construction (137), (138), because the strong direct limiting of the fluxes leads to their replacement by the free streaming flux W^{fs} in fact. However, W^{fs} is a function of the local temperature and not the temperature gradient as the original fluxes given by (96). Hence, the governing equation (95) is not parabolic any longer and becomes rather hyperbolic. In other words, the diffusion behaviour is eliminated locally and expected properties of the diffusion transport are not guaranteed. In this case, the local extreme is created even though it normally cannot be produced with diffusion. The flux limiting is strongly one-sided near the critical plane as can be seen from the flux fraction, causing significant imbalance on the laser ablation front. We find this behaviour highly non-physical and the indirect limiters are preferred instead. The difference between the indirect limiters is mostly insignificant. The harmonic mean flux limiter given by (140) reduces the heat conductivity coefficient smoothly unlike the rescale limiter, that sharply attenuates it only in the regions of excessive heat fluxes. Both approaches are feasible, but the harmonic mean limiter essentially performs almost identically as the rescale limiter, but with lower effective value of

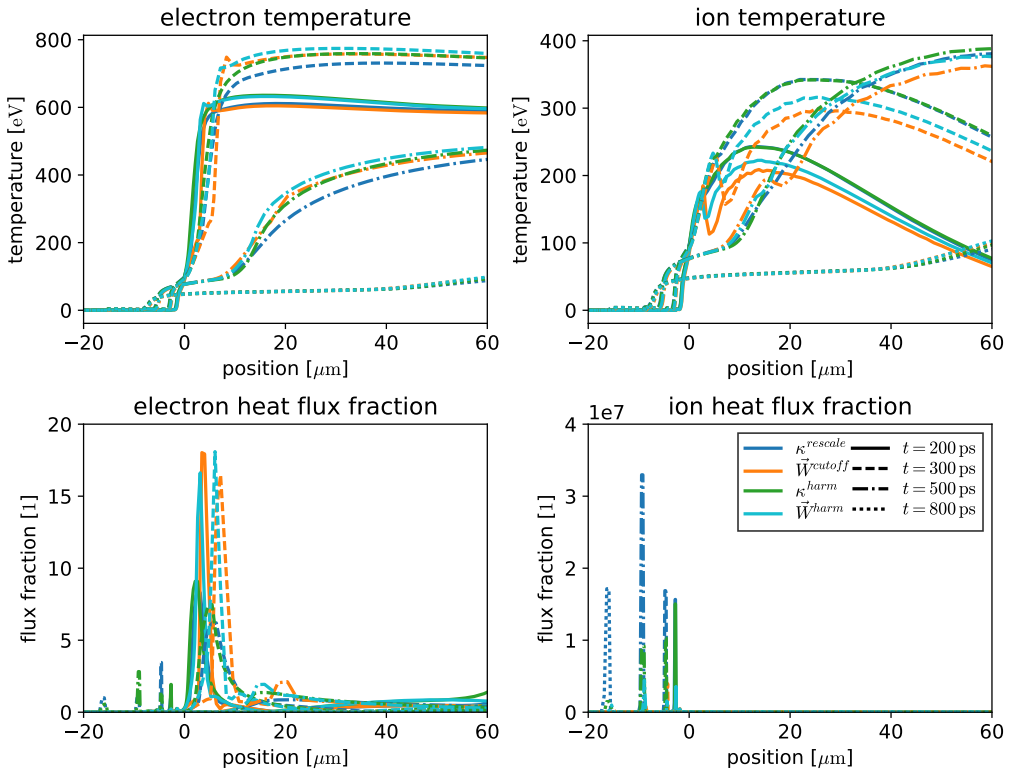

Figure 21: The temperatures and heat flux fractions (defined in section 4.3) at different times of the simulations with full thermal diffusion, radiation transport and different heat limiter methods (denoted by the term which they act on).

the heat flux coefficient. From this point of view, the rescale limiter behaves more predictably and hence it is used primarily.

The simulation results depend also on the employed electron–ion collision frequency model described in section 3.2. The models ν_{KS} and ν_{DS} are compared in Figure 22. It can be concluded that the overall differences are marginal, especially in the later phases of the simulation. The selection of the model of collision frequency affects mainly the initial phase, where the laser is absorbed in cold material, but its significance decreases later, because most of the plasma dynamics occurs in the Spitzer limit, that is satisfied by both models (see section 3.2). However, the temperature decreases in the conduction zone and the discrepancies between the models appear in the plot of the collision frequency at the late times of the simulation, but the system mainly undergoes only spatial expansion there and thus the effect of them is minimal. An interesting observation is that the ion temperature varies most visibly of the presented quantities and the difference of about 50 eV at some points may not be negligible for accurate simulations. The reason of this behaviour is that the ion temperatures are mostly governed by the electron ones and the heat exchange coefficients defined in section 3.3, but both quantities are affected by the collision frequency model.

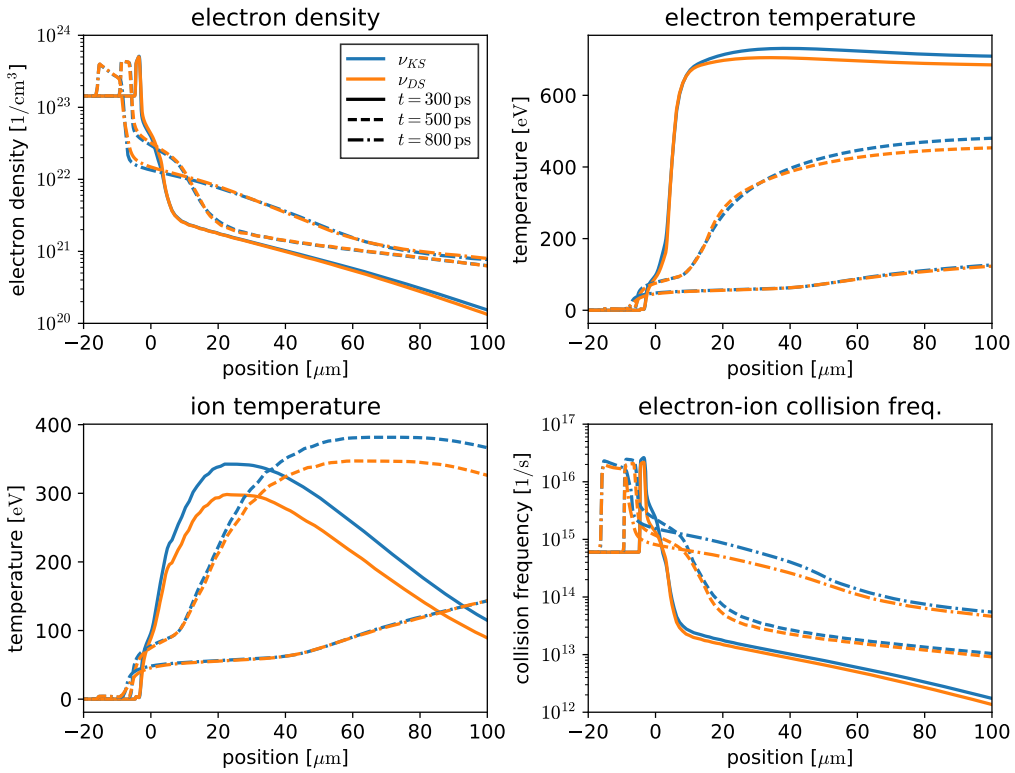

Figure 22: The electron densities, temperatures and the electron–ion momentum loss collision frequency at different times of the simulations with full thermal diffusion, radiation transport and different collision frequency models from the section 3.2.

Non-linearity of the system then causes that even relatively small changes in collision frequencies influence the ion temperatures considerably. However, it must be noted that ions confine less energy than electrons in plasma [22] and hence the effect is still insignificant from the global point of view of evolution of the system.

In the last but not least set of simulations, results with different equations of state are compared. The plots in Figure 23 show major differences between the simulation results. Although the equations of state (EOS) were only briefly overviewed in section 3.1 and full analysis of internal functioning of them is out of scope of this text, the significant effects on the results were observed and hence a practical comparison is made here. At the first sight, mainly the electron and ion temperatures vary remarkably with different EOSes. SESAME gives highest electron temperatures and that partially explains the low ion temperatures in the corona. However, this is not the only reason why the ion temperatures are lowest of the EOSes, because also the ion heat capacities are highest of them, decreasing the ion temperatures even further. In contrast, BADGER is nearly identical with QEOS in the corona most of the time, because BADGER is actually based on QEOS for electrons (see section 3.1). However, it vastly differs in the conduction zone and the shock wave, where peculiar behaviour

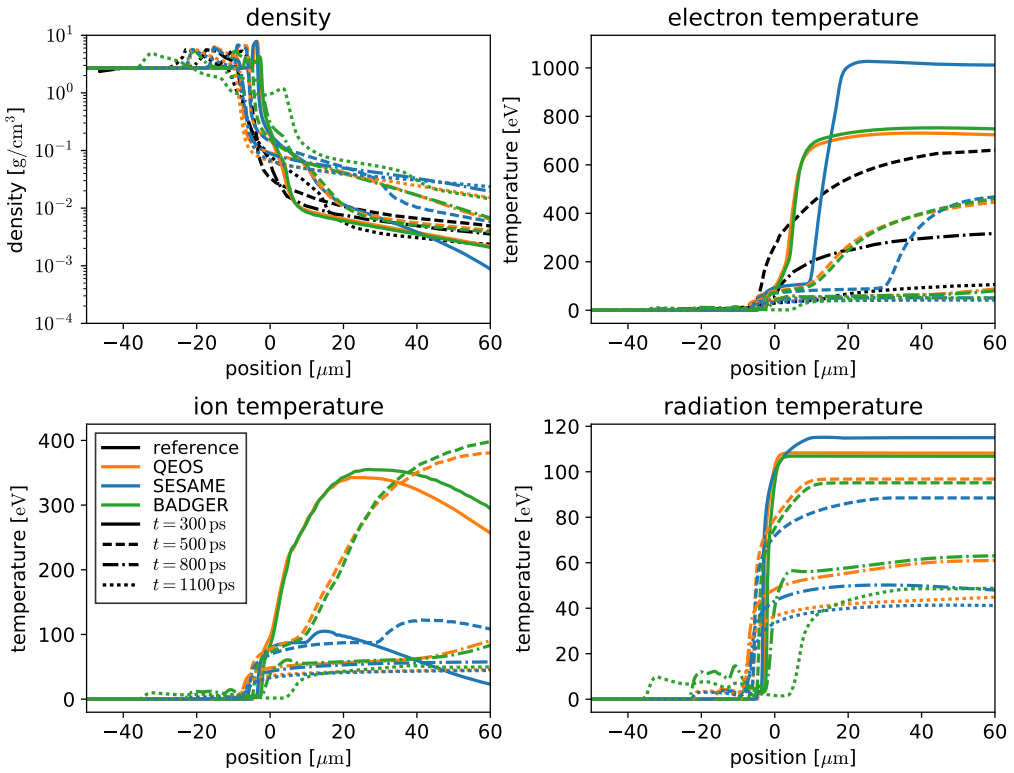

Figure 23: The mass densities and electron, ion and radiation temperatures at different times of the simulations with full thermal diffusion, radiation transport and different equations of state.

is observed. The position of the head of the shock is far from the other EOSes and likewise the reference data. The shock actually breaks down non-physically and one part of the shock counter-propagates in the late phases of the simulation. This makes BADGER practically unusable, despite its rich features. In contrast, SESAME and QEOS are both in a good agreement with the reference data from the point of view of the shock propagation. Nevertheless, the difference between SESAME density profiles and the profiles of other EOSes and the reference data increases toward the vacuum boundary. The radiation temperature confirms the statements above, but it is less sensitive to the shape of the electron temperature profile in the corona due to full saturation. To close this section, it can be concluded that QEOS provides best profiles of all compared equations of state and the results achieved with it are in a reasonable tolerance with the reference data [117].

6.2 2D simulations

In addition to the 1D simulations, two dimensional simulations in cylindrical geometry were performed to determine the effect of higher dimensional treatment on the numerical experiment and also confirm the feasibility of the proposed laser absorption algorithm in section 2.2. Therefore, 2D simulations with code PALE2 were made with the configuration described in the introduction of this section. However, it must be noted that PALE2 does not posses the radiation transport model nor the non-local transport model presented in section 5. Extension of this model to more dimensions and coupling with the hydrodynamical code is one of the possible topics of future research. Nevertheless, the simulations without radiation transport and only classical heat diffusion and also in one-temperature approximation give better insight into the mechanisms of the whole ablation process.

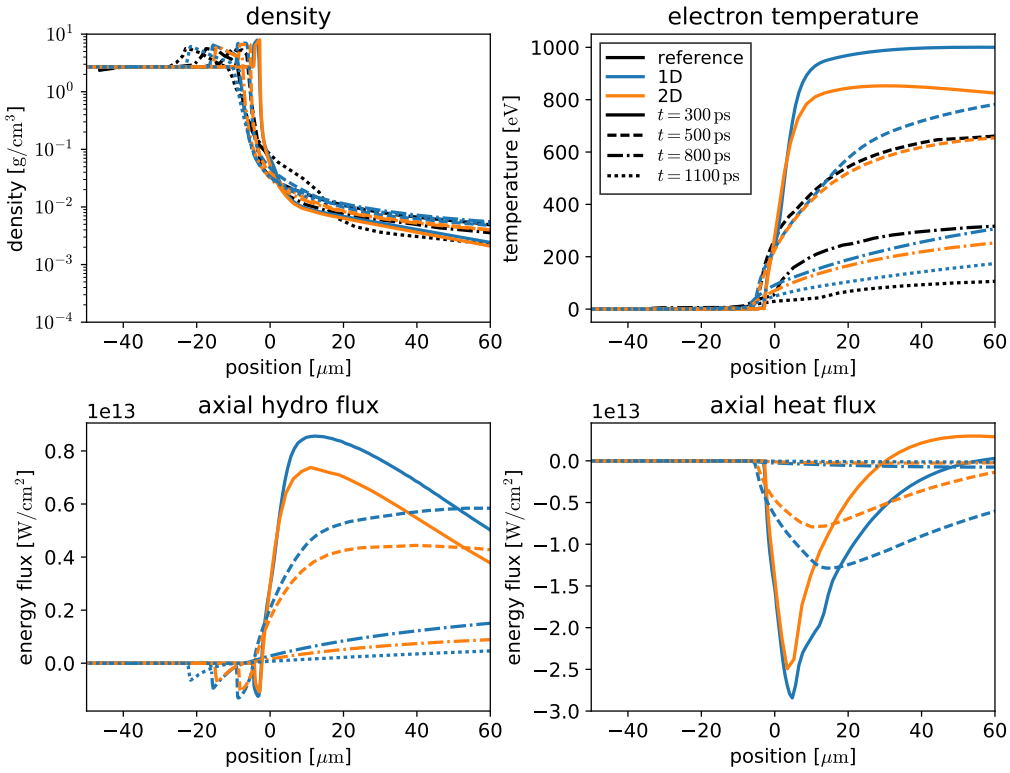

Figure 24: A comparison of density, electron temperatures, axial hydrodynamical fluxes and heat fluxes obtained from the reference data from [117], 1D two-temperature simulation with full thermal diffusion without the radiation transport in the code PETE and 2D one-temperature simulation with heat diffusion in PALE2 plotted at the central axis $r = 0$. (The profiles from 2D simulation at $t = 1100$ ps are not present, because the simulation ended before this time.)

The set of plots in Figure 24 compares the 1D approximation of the problem

with full 2D simulation in cylindrical geometry that actually approximates fully 3D configuration due to the axial symmetry (assuming normal incidence of the laser). Both codes used interpolated QEOS equation of state similarly to the previous section. It must be stressed that the interpolation technique is necessary in this case, because the 2D simulation with $80 \times 140 = 11200$ computational cell and direct evaluation/inversion of EOS takes even weeks of computation.

Overall, it can be observed that the simulations are very close to the reference [117], even though the radiation transport was not present in them. This supports the idea that the numerical experiment in the reference is more driven by the thermal diffusion. However, double ablation front structure appears in the later phases of the simulation, indicating the importance of the radiation transport there.

In addition, it can be read from the simulations that the two-temperature dynamics have negligible effect on the global evolution of the simulation under given conditions. This is a consequence of close temperatures in the conduction zone and energetic dominance of the electrons in the corona during the nanosecond laser pulses.

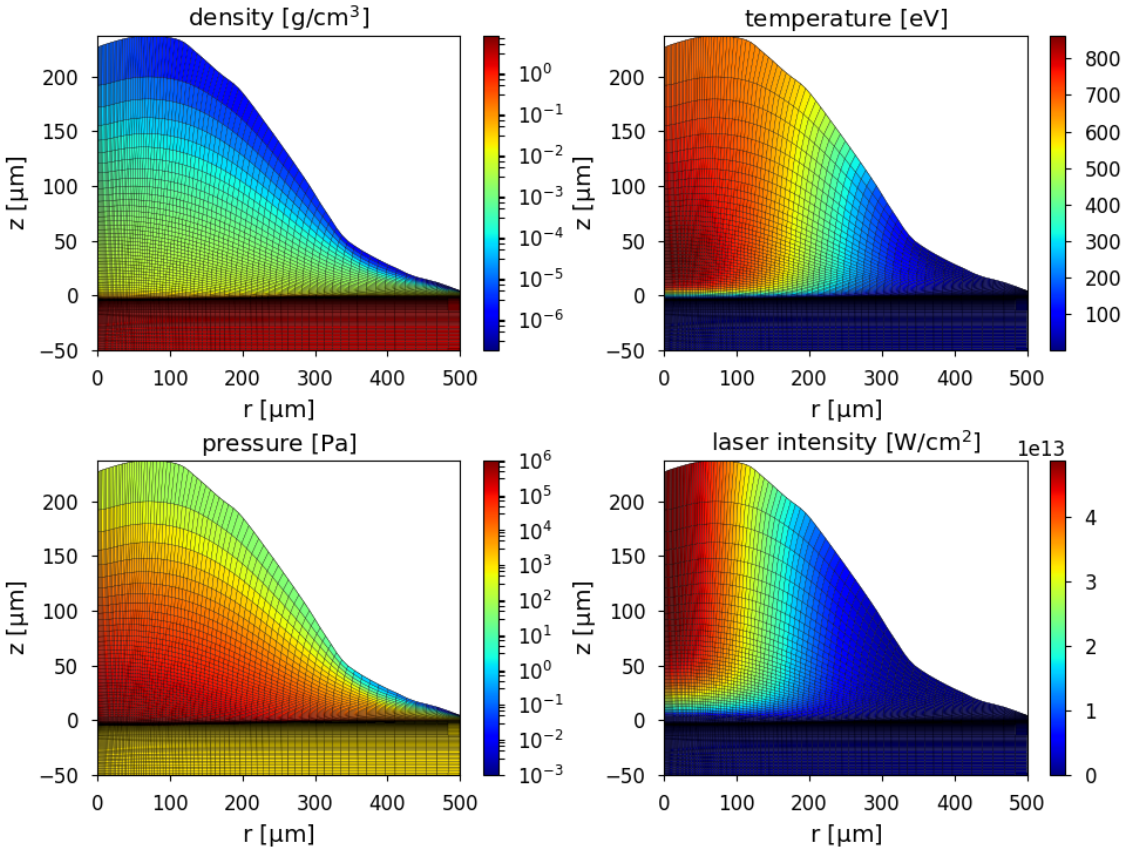

Figure 25: The spatial profiles of mass density, temperature, hydrostatic pressure and laser intensity within the 2D simulation in cylindrical geometry at time $t = 300$ ps.

The results also show that full spatial expansion of the plasma lowers the temperatures and only slightly the density profiles, but position of the shock remains almost unchanged due to large laser spot size and consequent low spatial divergence of the

shock. Its velocity follows the hydrodynamical balance in front of the critical plane that remain preserved, because of the short distance between the critical plane and the target surface. However, the corona dynamics differs more visibly, the electron temperatures are lower as well as the axial energy fluxes.

The lower coronal temperatures compared to the 1D simulation are caused by the radial hydrodynamical flux ($\vec{q}_h = (p_e + p_i)\vec{u}$) during the spatial expansion and also the radial heat fluxes. Both of them are induced by the radial gradients of the quantities and primarily the radial gradient of the laser intensity as shown in Figure 25. The closer analysis of the fluxes in Figure 26 shows that the conduction dominates over the convection in early times of the simulation, but both of them are oriented from the central symmetry axis, contributing on the reduction of the temperatures along it. However, the radial fluxes are predictably largest around the Gaussian RMS width $r_\sigma = d_{FWHM}/(2\sqrt{2\ln 2}) \doteq 118.9$ μm, where the Gaussian beam has highest spatial gradient. The profiles of axial fluxes follow the variation of the quantities in the radial direction and qualitatively resembles the 1D simulation as confirmed along the central axis in Figure 24. This holds as long as the spatial divergence is not dominating the simulation.

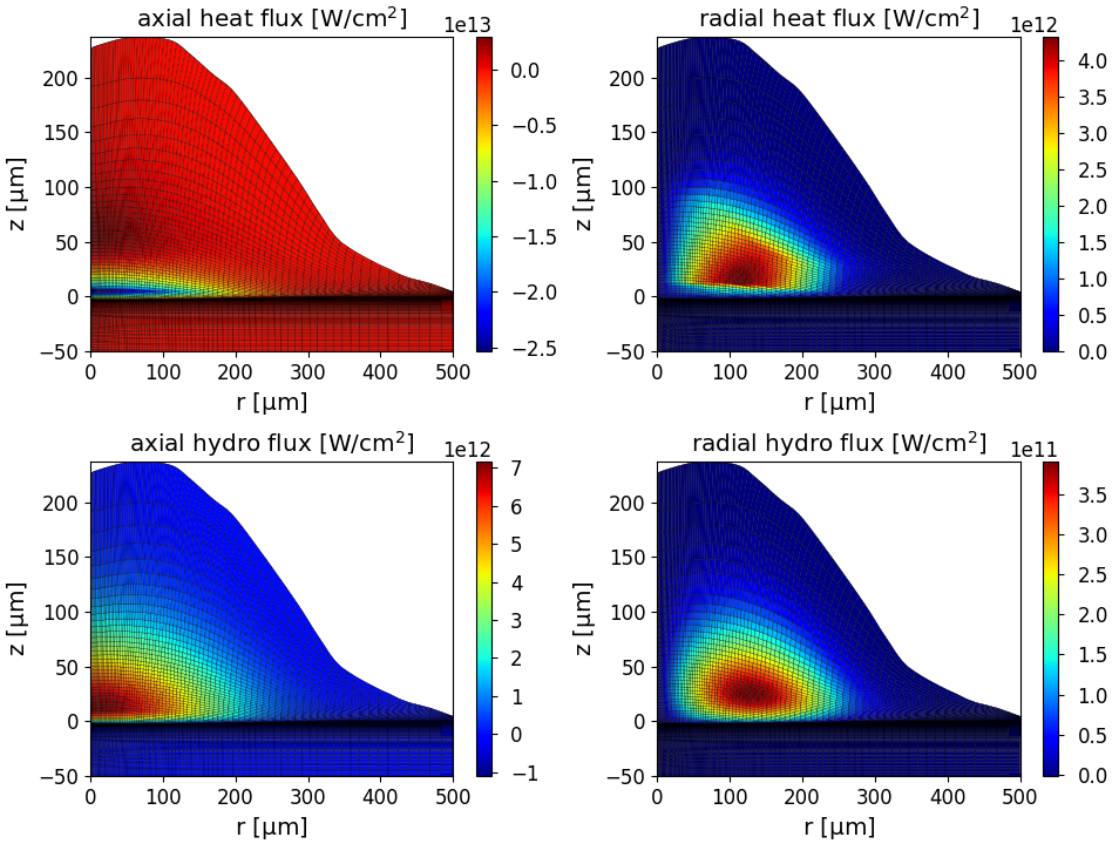

Figure 26: The spatial profiles of heat and hydrodynamical energy fluxes within the 2D simulation in cylindrical geometry at time $t = 300$ ps.

In order to extend the discussion of the higher dimensional treatment on the

simulation results, the plots of quantities at later time are also given in Figure 27. The expansion progressed even further there and it must be remarked that it is not possible to perform the simulation without application of ALE method that makes indispensable part of the code, because it visibly regularizes the mesh in the corona and maintains it sufficiently dense for the laser absorption algorithm described in section 2.2. Artificial anisotropic diffusion is introduced by the method, because each rezoning and remapping step mixes the quantities to some degree [122]. Thus, the evolution of the system may not be fully physically realistic in the outer regions, where temperatures are low, but curvature of the mesh is extreme. However, high accuracy of the simulation is maintained in most of the area and regularity of the mesh supports the numerical precision of the simulation.

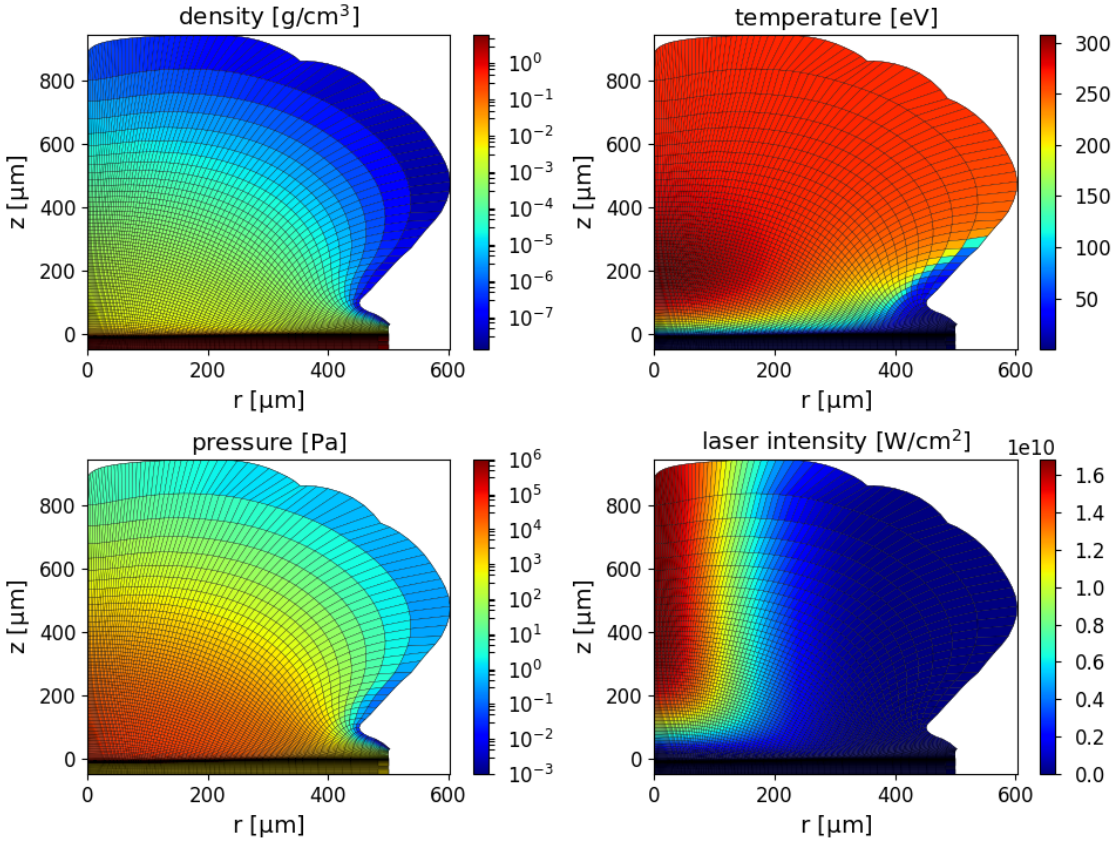

Figure 27: The spatial profiles of mass density, temperature, hydrostatic pressure and laser intensity within the 2D simulation in cylindrical geometry at time $t = 800$ ps.

From the physical point of view, an interesting phenomena occurs. The radial fluxes were dominated by heat conduction in the previous case, but their amplitude switches over in the meantime and the radial hydrodynamical fluxes are higher now as shown in Figure 28. This follows dispersion of the steep gradients of the quantities and releasing of the confined internal energy by hydrodynamical expansion. In addition, the maximal fluxes are driven away from the central axis, because they are not directly imprinted by the energy sources any longer. The magnitude of laser deposition

has decreased considerably, almost 3 orders of magnitude in particular. Instead, the inertia of the system plays the role in this case and the evolution continues the started hydrodynamic expansion.

The axial energy fluxes in Figure 28 further diverge from the 1D profiles, because the expansion of the corona is not negligible. Instead, they approximately follow the quiver of quantity gradients. The axial hydrodynamical flux also dominates over the heat flux, pushing the corona away from the target surface. In contrast, the heat flux mainly disperses the gradient of the temperature near the critical plane and also causes almost complete saturation of the temperature in the corona.

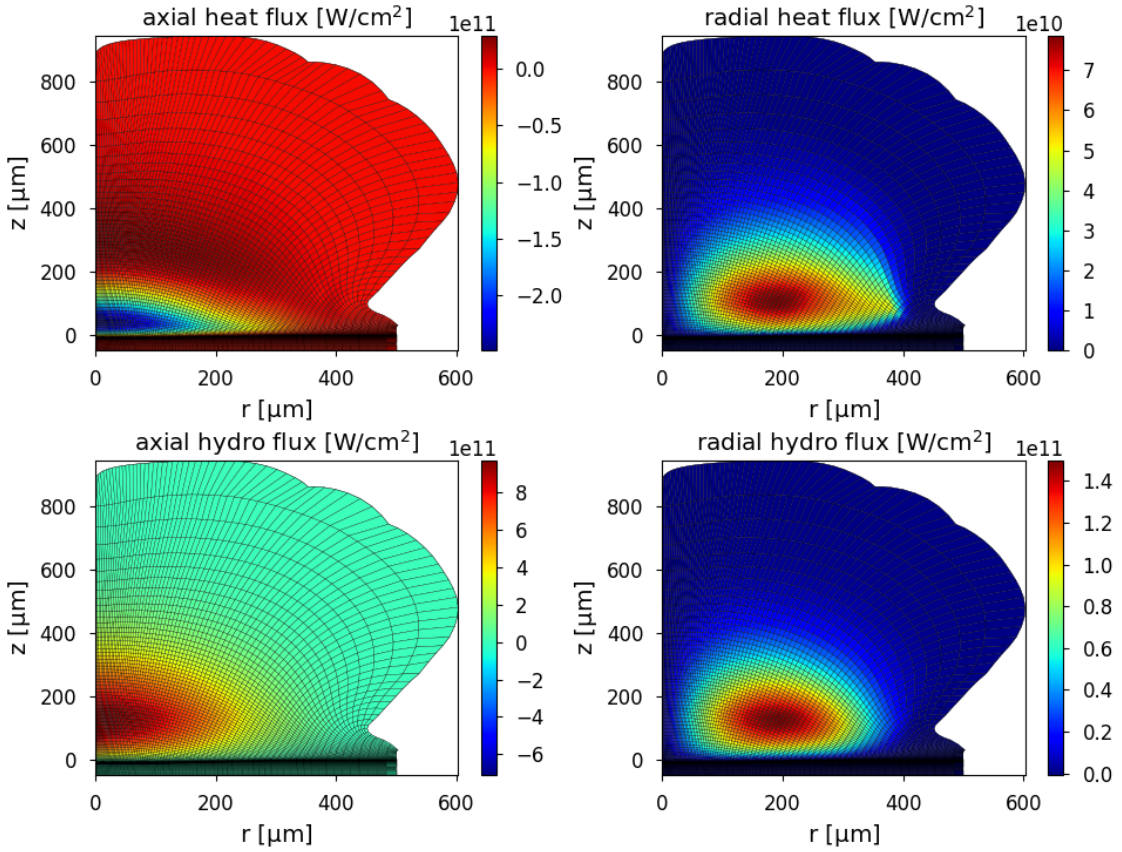

Figure 28: The spatial profiles of heat and hydrodynamical energy fluxes within the 2D simulation in cylindrical geometry at time $t = 800$ ps.

Conclusions

Laser–target interaction is a complex process involving many physical phenomena. Hydrodynamical approach is one of the most popular, describing the plasma as a fluid governed by the laws of hydrodynamics. Other physical processes are then incorporated within the closure model of the resulting system of partial differential equations and various numerical methods are employed to solve it computationally.

The plasma dynamics is primarily driven by laser energy deposition in this case, showing the necessity of a proper laser absorption algorithm. In context of this work, the 1D algorithm based on solution of the stationary Maxwell's equations has been studied and numerically treated to increase robustness and reliability of the method. A technique to utilize the high-order finite element discretization of the thermodynamic quantities (see below) was also proposed and implemented. Moreover, the development of the laser absorption algorithm application in two dimensions continued from the previous work and the bilinear interpolation was added to the mesh refining algorithm, increasing the order of convergence of the method remarkably.

Physical closure relations are also presenting indispensable part of the simulation, whenever physical accuracy is concerned. The equations of state form closure of ideal hydrodynamics, but also provide important thermodynamic quantities to other parts of the model. Hence, the used equations of state were briefly reviewed and practically compared. In addition to them, collision frequency related expressions are constituting the physical closure. The idea of a single central collision frequency was followed, wherever it was possible. Several sophisticated models were integrated and compared, because the classical Spitzer–Härm formula is not sufficient to describe the low temperatures regime.

The diffusion approximation of the heat transfer is traditionally used in the context of hydrodynamical simulation codes. The physical and numerical aspects of this approach were discussed. The semi-implicit diffusion scheme, developed in the previous work, was applied on the two-temperature model and further extended to incorporate the electron–ion temperature relaxation. Nevertheless, certain theoretical considerations led to improvement and implementation of a separate fully conservative electron–ion energy exchange numerical scheme. In addition, several heat flux limiting techniques were implemented and their effect on the simulation results was shown as well as the importance of a proper selection heat flux coefficient values.

The analysis of the physical conditions during the laser ablation reveals that application of the diffusion approximation is not usually properly justified. The electron mean free path is significantly larger then the typical temperature gradient scales and hence non-locality of the transport must be taken into account. The novel approach based on numerical solution of a reduced kinetic equation, that was introduced in [9], has been followed. In particular, the development of the 1D hydrodynamical simulation code PETE containing this model continued. The ion heat transport was added and the discontinuous Galerkin finite elements scheme was also extended by the high resolution laser absorption as mentioned above. However, the ion transport contribution was found to be less important most often for (near) nanosecond laser pulses.

Finally, 2D simulations were performed in the simulation code PALE2 and the

effect of the full spatial expansion was analysed. The 2D laser absorption algorithm viability was verified in the process. Furthermore, the effect of radiation transport was determined comparatively, but deeper revision of the model presents a possible topic of future research. Also the results revealed that the two-temperature model is mostly comparable with the one-temperature model for longer laser pulses.

Overall, good agreement of the simulation results in 1D and 2D and the reference data taken from literature was found. Moreover, the authors of the reference paper verified their results by an experiment and hence our simulations can be also considered well-founded. In order to summarize, all points of the assignment were fulfilled.

Author's publications

- M. Holec, J. Nikl, M. Vranic, S. Weber, and G. Korn. Nonlocal electron and radiation transport hydrodynamic model and its effect in high-power laser pre-pulse physics. *Physics of Plasmas*, first submitted March 2017, corrected April 2017

References

[1] M. Tzoufras, A. R. Bell, P. A. Norreys and F. S. Tsung. A Vlasov-Fokker-Planck code for high energy density physics. *Journal of Computational Physics*, 230(17):6475–6494, 2011. ISSN 00219991. doi:10.1016/j.jcp.2011.04.034.

[2] O. Klimo, J. Pšikal, V. T. Tikhonchuk and S. Weber. Two-dimensional simulations of laser–plasma interaction and hot electron generation in the context of shock-ignition research. *Plasma Physics and Controlled Fusion*, 56(5):055010, 2014. ISSN 0741-3335. doi:10.1088/0741-3335/56/5/055010.

[3] M. Kuchařík. *Arbitrary Lagrangian-Eulerian (ALE) Methods in Plasma Physics*. Doctoral thesis, FJFI ČVUT, 2006.

[4] R. Liska and M. Kuchařík. Arbitrary Lagrangian Eulerian method for compressible plasma simulations. In J. Donea, A. Huerta, J.-P. Ponthot and A. Rodríguez-Ferran, editors, *Proceedings of Equadiff 11*, pages 213–222. 2007.

[5] D. J. Benson. Computational methods in Lagrangian and Eulerian hydrocodes. *Computer Methods in Applied Mechanics and Engineering*, 99(2):235–394, 1992. ISSN 0045-7825. doi:http://dx.doi.org/10.1016/0045-7825(92)90042-I.

[6] C. W. Hirt, A. A. Amsden and J. L. Cook. An arbitrary Lagrangian-Eulerian computing method for all flow speeds. *Journal of Computational Physics*, 14(3):227–253, 1974. ISSN 0021-9991. doi:http://dx.doi.org/10.1016/0021-9991(74)90051-5.

[7] D. S. Clark, M. M. Marinak, C. R. Weber, D. C. Eder, S. W. Haan, B. A. Hammel, D. E. Hinkel, O. S. Jones, J. L. Milovich, P. K. Patel, H. F. Robey, J. D. Salmonson, S. M. Sepke and C. A. Thomas. Radiation hydrodynamics modeling of the highest compression inertial confinement fusion ignition experiment from the National Ignition Campaign. *Physics of Plasmas*, 22(2):1–19, 2015. ISSN 10897674. doi:10.1063/1.4906897.

[8] A. Marocchino, S. Atzeni and A. Schiavi. Effects of non-local electron transport in one-dimensional and two-dimensional simulations of shock-ignited inertial confinement fusion targets. *Physics of Plasmas*, 21(1):1–8, 2014. ISSN 10897674. doi:10.1063/1.4861389.

[9] M. Holec. *Nonlocal Transport Hydrodynamic Modeling of Laser Heated Plasmas*. Doctoral thesis, FJFI ČVUT, 2016.

[10] J. Nikl. *Hydrodynamické simulace ablace a expanze plazmatu při pulzní laserové depozici*. Bachelor thesis, FJFI ČVUT, 2015.

[11] J. Velechovský. *Modelování absorpce laserového záření v plazmatu*. Bachelor thesis, FJFI ČVUT, 2009.

[12] T. Kapin, M. Kuchařík, J. Limpouch and R. Liska. Hydrodynamic simulations of laser interactions with low-density foams. *Czechoslovak Journal of Physics*, 56, 2006. ISSN 00114626. doi:10.1007/s10582-006-0243-y.

[13] J. Nikl. *Numerické simulace jevů v plazmatu při pulzní laserové depozici*. Research project, FJFI ČVUT, 2016.

[14] L. Spitzer and R. Härm. Transport phenomena in a completely ionized gas. *Physical Review*, 89(5):977–981, 1953. ISSN 0031899X. doi:10.1103/PhysRev.89.977.

[15] M. Wheeler and C. Dawson. An operator-splitting method for advection-diffusion-reaction problems. Technical Report 87-9, Rice University, Houston, Texas U.S.A., 1987.

[16] S. K. Godunov. A difference method for numerical calculation of discontinuous solutions of the equations of hydrodynamics. *Matematicheskii Sbornik (N.S.)*, 47(89)(3):271–306, 1959.

[17] E. Caramana, D. Burton, M. Shashkov and P. Whalen. The construction of compatible hydrodynamics algorithms utilizing conservation of total energy. *Journal of Computational Physics*, 146(1):227–262, 1998. ISSN 00219991. doi:10.1006/jcph.1998.6029.

[18] M. Kucharik and M. Shashkov. Conservative multi-material remap for staggered multi-material Arbitrary Lagrangian-Eulerian methods. *Journal of Computational Physics*, 258:268–304, 2014. ISSN 00219991. doi:10.1016/j.jcp.2013.10.050.

[19] M. Berndt, J. Breil, S. Galera, M. Kuchařík, P. H. Maire and M. Shashkov. Two-step hybrid conservative remapping for multimaterial arbitrary Lagrangian-Eulerian methods. *Journal of Computational Physics*, 230(17):6664–6687, 2011. ISSN 00219991. doi:10.1016/j.jcp.2011.05.003.

[20] E. Livne, A. Glasner and O. F. Computational. A Finite Difference Scheme for the Heat Conduction Equation. *Journal of Computational Physics*, 66(1):59–66, 1985. ISSN 00219991. doi:10.1016/0021-9991(85)90156-1.

[21] R. Ramis, J. Meyer-ter-Vehn and J. Ramírez. MULTI2D - a computer code for two-dimensional radiation hydrodynamics. *Computer Physics Communications*, 180(6):977–994, 2009. ISSN 00104655. doi:10.1016/j.cpc.2008.12.033.

[22] K. Eidmann, J. Meyer-ter Vehn, T. Schlegel and S. Hüller. Hydrodynamic simulation of subpicosecond laser interaction with solid-density matter. *Physical Review E - Statistical Physics, Plasmas, Fluids, and Related Interdisciplinary Topics*, 62(1 B):1202–1214, 2000. ISSN 1063651X. doi:10.1103/PhysRevE.62.1202.

[23] M. Born and E. Wolf. *Principles of optics: electromagnetic theory of propagation, interference and diffraction of light*. Cambridge University Press, 1999. ISBN 0521642221. doi:10.1016/S0030-3992(00)00061-X.

[24] M. Holec. *Modeling of diffusive problems in laser plasma.* Master's thesis, FJFI ČVUT, 2012.

[25] Y. V. Afanas, N. N. Demchenko, O. N. Krokhin and V. B. Rosanov. Absorption and reflection of laser radiation by a dispersing high-temperature plasma. *Journal of Experimental and Theoretical Physics*, 72:170–179, 1977.

[26] R. Ramis, K. Eidmann, J. Meyer-Ter-Vehn and S. Hüller. MULTI-fs - A computer code for laser-plasma interaction in the femtosecond regime. *Computer Physics Communications*, 183(3):637–655, 2012. ISSN 00104655. doi:10.1016/j.cpc.2011.10.016.

[27] T. J. Barth. Numerical methods for gasdynamic systems on unstructured meshes. In D. Kröner, M. Ohlberger and C. Rohde, editors, *An Introduction to Recent Developments in Theory and Numerics for Conservation Laws: Proceedings of the International School on Theory and Numerics for Conservation Laws, Freiburg/Littenweiler, October 20–24, 1997*, pages 195–285. Springer, Berlin, 1999. ISBN 978-3-642-58535-7. doi:10.1007/978-3-642-58535-7_5.

[28] J. Velechovský. *Numerické metody modelování laserového plazmatu.* Master's thesis, FJFI ČVUT v Praze, 2011.

[29] C. Hua. An inverse transformation for quadrilateral isoparametric elements: Analysis and application. *Finite Elements in Analysis and Design*, 7(2):159 – 166, 1990. ISSN 0168-874X. doi:10.1016/0168-874X(90)90007-2.

[30] W. H. Press, S. A. Tekolsky, W. T. Vetterling and B. P. Flannery. *Numerical Recipes: The Art of Scientific Computing, Third Edition.* Cambridge University Press, 2007. ISBN 0521880688.

[31] J. Abdallah Jr, G. Kerley, B. Bennett, J. Johnson, R. Albers and W. Huebner. HYDSES: a subroutine package for using Sesame in hydrodynamic codes. Technical Report LA-8209, Los Alamos Scientific Lab., NM (USA), 1980.

[32] G. T. SESAME report on the Los Alamos equation-of-state library. Technical Report LALP-83-4, Los Alamos National Laboratory, Los Alamos, 1983.

[33] S. P. Lyon and J. D. Johnson. Sesame: the Los Alamos National Laboratory equation of state database. Technical Report LA-UR-92-3407, Los Alamos National Laboratory, Los Alamos, NM, 1992.

[34] R. M. More, K. H. Warren, D. A. Young and G. B. Zimmerman. A new quotidian equation of state (QEOS) for hot dense matter. *Physics of Fluids*, 31(10):3059, 1988. ISSN 00319171. doi:10.1063/1.866963.

[35] R. Feynman, N. Metropolis and E. Teller. Equations of State of Elements Based on the Generalized Fermi-Thomas Theory. *Physical Review*, 75(10), 1949.

[36] J. F. Barnes. Statistical atom theory and the equation of state of solids. *Physical Review*, 153(1):269–275, 1967. ISSN 0031899X. doi:10.1103/PhysRev.153.269.

[37] C. Cranfill and R. M. More. IONEOS: A Fast, Analytic Ion Equation-of-State Routine. Technical Report LA–7313–MS, Los ALamos Scientific Laboratory, 1978.

[38] A. J. Kemp and J. Meyer-ter-Vehn. An equation of state code for hot dense matter, based on the QEOS description. *Nuclear Instruments and Methods in Physics Research, Section A: Accelerators, Spectrometers, Detectors and Associated Equipment*, 415(3):674–676, 1998. ISSN 01689002. doi:10.1016/S0168-9002(98)00446-X.

[39] S. Faik, M. M. Basko, A. Tauschwitz, I. Iosilevskiy and J. A. Maruhn. Dynamics of volumetrically heated matter passing through the liquid–vapor metastable states. *High Energy Density Physics*, 8(4):349–359, 2012.

[40] T. A. Heltemes and G. A. Moses. BADGER v1.0: A Fortran equation of state library. *Computer Physics Communications*, 183(12):2629–2646, 2012. ISSN 00104655. doi:10.1016/j.cpc.2012.07.010.

[41] M. Zeman. *Thermodynamically Consistent Interpolation of the Equation of State for Hydrodynamic Calculations*. Bachelor thesis, FJFI ČVUT, 2016.

[42] Y. T. Lee and R. M. More. An electron conductivity model for dense plasmas. *Physics of Fluids*, 27(5):1273, 1984. ISSN 00319171. doi:10.1063/1.864744.

[43] J. D. Huba. NRL: PLASMA FORMULARY. Technical report, Naval Research Laboratory, Washington, DC 20375, 2013.

[44] R. S. Cohen, L. Spitzer and P. M. Routly. The electrical conductivity of an ionized gas. *Physical Review*, 80(2):230–238, 1950. ISSN 0031899X. doi:10.1103/PhysRev.80.230.

[45] B. H. Christensen, K. Vestentoft and P. Balling. Short-pulse ablation rates and the two-temperature model. *Applied Surface Science*, 253(15):6347–6352, 2007. ISSN 01694332. doi:10.1016/j.apsusc.2007.01.045.

[46] A. Abrikosov. *Fundamentals of the Theory of Metals*. Elsevier Science Publishers B. V., Amsterdam, 1988. ISBN 0444870954.

[47] N. W. Ashcroft and N. D. Mermin. *Solid State Physics*. Saunders, 1976.

[48] X. Mao and R. E. Russo. Observation of plasma shielding by measuring transmitted and reflected laser pulse temporal profiles. *Applied Physics A: Materials Science & Processing*, 64(1):1–6, 1996. ISSN 0947-8396. doi:10.1007/s003390050437.

[49] A. Tronnier. *Absorption von VUV-Photonen in Warm Dense Matter*. Ph.D. thesis, Max-Planck-Institut für Quantenoptik, 2007.

[50] V. P. Krainov. Inverse stimulated bremsstrahlung of slow electrons under Coulomb scattering. *Journal of Physics B: Atomic, Molecular and Optical Physics*, 33(8):1585–1595, 2000. ISSN 0953-4075. doi:10.1088/0953-4075/33/8/309.

[51] S. Atzeni and J. Meyer-ter Vehn. *The Physics of Inertial Fusion: Beam Plasma Interaction, Hydrodynamics, Hot Dense Matter*. Oxford University Press, 2004. ISBN 0198562640.

[52] D. Yu, L. Jiang, F. Wang, X. Shi, L. Qu and Y. Lu. Hydrodynamic simulation of ultrashort pulse laser ablation of gold film. *Applied Physics A*, 119(3):1047–1052, 2015. ISSN 0947-8396. doi:10.1007/s00339-015-9065-8.

[53] L. Spitzer Jr. *Physics of fully ionized gases*. Interscience Publishers, inc., New York, 1956.

[54] C. Kittel. *Introduction to Solid State Physics, 7th Ed.*. Wiley, 1996.

[55] W. S. M. Werner. Electron transport in solids for quantitative surface analysis. *Surface and Interface Analysis*, 31(3):141–176, 2001. ISSN 01422421. doi:10.1002/sia.973.

[56] S. Tanuma, C. Powell and D. Penn. Calculations of electron inelastic mean free paths. IX. Data for 41 elemental solids over the 50 eV to 30 keV range. *Surface and Interface Analysis*, 43(3):689–713, 2011.

[57] R. Duclous, B. Dubroca, F. Filbet and V. Tikhonchuk. High order resolution of the Maxwell–Fokker–Planck–Landau model intended for ICF applications. *Journal of Computational Physics*, 228(14):5072–5100, 2009.

[58] H. Bethe. Bremsformel für elektronen relativistischer geschwindigkeit. *Zeitschrift für Physik*, 76(5-6):293–299, 1932.

[59] Y. S. Touloukian, R. W. Powell, C. Y. Ho and P. G. Klemens. *Volume 1 : Thermal conductivity - Metallic elements and alloys*. IFI/PLENUM, New York - Washington, 1970. ISBN 306-67021-6.

[60] R. C. Malone, R. L. McCrory and R. L. Morse. Indications of Strongly Flux-Limited Electron Thermal Conduction in Laser-Target Experiments. *Physical Review Letters*, 34(12):721–724, 1975. ISSN 00319007. doi:10.1103/PhysRevLett.34.721.

[61] A. V. Brantov and V. Y. Bychenkov. Nonlocal transport in hot plasma. Part I. *Plasma Physics Reports*, 39(9):698–744, 2013. ISSN 1063780X. doi:Doi10.1134/S1063780x13090018.

[62] D. Mihalas and B. W. Mihalas. *Foundations of Radiation Hydrodynamics*. Oxford University Press, 1984. ISBN 0195034376.

[63] D. Marla, U. V. Bhandarkar and S. S. Joshi. Critical assessment of the issues in the modeling of ablation and plasma expansion processes in the pulsed laser deposition of metals. *Journal of Applied Physics*, 109(2):021101, 2011. ISSN 00218979. doi:10.1063/1.3537838.

[64] J. Šilar. *Hydrodynamické modelování laserového plazmatu.* Bachelor thesis, FJFI ČVUT, 2008.

[65] M. Shashkov and S. Steinberg. Solving diffusion equations with rough coefficients in rough grids. *Journal of Computational Physics*, 129(2):383–405, 1996. ISSN 00219991. doi:10.1006/jcph.1996.0257.

[66] M. Hestenes and E. Stiefel. Methods of conjugate gradients for solving linear systems. *Journal of Research of the National Bureau of Standards*, 49(6):409, 1952. ISSN 0091-0635. doi:10.6028/jres.049.044.

[67] I. Craig and A. Sneyd. An alternating direction implicit scheme for parabolic systems of partial differential equations. *Computers & Mathematics with Applications*, 20(3):53–62, 1990. ISSN 08981221. doi:10.1016/0898-1221(90)90030-N.

[68] A. Sunahara, J. A. Delettrez, C. Stoeckl, R. W. Short and S. Skupsky. Time-Dependent Electron Thermal Flux Inhibition in Direct-Drive Laser Implosions. *Physical Review Letters*, 91(9):950031–950034, 2003. ISSN 00319007. doi:10.1103/PhysRevLett.91.095003.

[69] D. G. Colombant, W. M. Manheimer and M. Busquet. Test of models for electron transport in laser produced plasmas. *Physics of Plasmas*, 12(7):072702, 2005. ISSN 1070664X. doi:10.1063/1.1929777.

[70] J. F. Luciani, P. Mora and J. Virmont. Nonlocal heat transport due to steep temperature gradients. *Physical Review Letters*, 51(18):1664–1667, 1983. ISSN 00319007. doi:10.1103/PhysRevLett.51.1664.

[71] J. R. Albritton, E. A. Williams, I. B. Bernstein and K. P. Swartz. Nonlocal electron heat transport by not quite Maxwell-Boltzmann distributions. *Physical Review Letters*, 57(15):1887–1890, 1986. ISSN 00319007. doi:10.1103/PhysRevLett.57.1887.

[72] G. P. Schurtz, P. D. Nicolaï and M. Busquet. A nonlocal electron conduction model for multidimensional radiation hydrodynamics codes. *Physics of Plasmas*, 7(10):4238, 2000. ISSN 1070664X. doi:10.1063/1.1289512.

[73] S. I. Anisimov, B. S. Luk'yanchuk and A. Luches. An analytical model for three-dimensional laser plume expansion into vacuum in hydrodynamic regime. *Applied Surface Science*, 96-98:24–32, 1996. ISSN 01694332. doi:10.1016/0169-4332(95)00373-8.

[74] S. Chapman and T. G. Cowling. *The Mathematical Theory of Non-uniform Gases.* Cambridge university press, 1952.

[75] J. F. Luciani, P. Mora and R. Pellat. Quasistatic heat front and delocalized heat flux. *Physics of Fluids (1958-1988)*, 28(3):835–845, 1985. ISSN 00319171. doi:10.1063/1.865052.

[76] A. Bendib, J. F. Luciani and J. P. Matte. An improvement of the nonlocal heat flux formula. *Physics of Fluids*, 31(4):711–713, 1988. ISSN 00319171. doi: 10.1063/1.866806.

[77] S. I. Krasheninnikov. On nonlocal electron heat conduction. *Physics of Fluids B*, 5(1):74–76, 1993.

[78] M. K. Prasad and D. S. Kershaw. Nonviability of some nonlocal electron heat transport modeling. *Physics of Fluids B: Plasma Physics (1989-1993)*, 1(12):2430–2436, 1989. ISSN 08998221. doi:http://dx.doi.org/10.1063/1.859178.

[79] E. M. Epperlein and R. W. Short. A practical nonlocal model for electron heat transport in laser plasma. *Phys. Fluids B*, 3(1991):3092–3098, 1991. ISSN 08998221. doi:10.1063/1.859789.

[80] M. K. Prasad and D. S. Kershaw. Stable solutions of nonlocal electron heat transport equations. *Physics of Fluids B: Plasma Physics (1989-1993)*, 3(11):3087–3091, 1991. ISSN 08998221. doi:10.1063/1.859995.

[81] V. Y. Bychenkov, W. Rozmus, V. T. Tikhonchuk and A. V. Brantov. Nonlocal electron transport in a plasma. *Physical Review Letters*, 75(24):4405–4408, 1995. ISSN 00319007. doi:10.1103/PhysRevLett.75.4405.

[82] A. V. Brantov, V. T. Tikhonchuk and W. Rozmus. Nonlocal plasma electron hydrodynamics. *Journal of Experimental and Theoretical Physics*, 110:1301–1327, 1996.

[83] V. N. Novikov and V. T. Tikhonchuk. Theory of nonlocal transport for small perturbations in a plasma. *Journal of Experimental and Theoretical Physics*, 87(5):13–15, 1998. ISSN 10637761.

[84] S. Weber, G. Riazuelo, P. Michel, R. Loubère, F. Walraet, V. Tikhonchuk, V. Malka, J. Ovadia and G. Bonnaud. Modeling of laser–plasma interaction on hydrodynamic scales: Physics development and comparison with experiments. *Laser and Particle Beams*, 22(02):189–195, 2004. ISSN 0263-0346. doi: 10.1017/S0263034604222157.

[85] S. Weber, P. H. Maire, R. Loubère, G. Riazuelo, P. Michel, V. Tikhonchuk and J. Ovadia. A transport simulation code for inertial confinement fusion relevant laser-plasma interaction. *Computer Physics Communications*, 168(3):141–158, 2005. ISSN 00104655. doi:10.1016/j.cpc.2005.01.017.

[86] P. L. Bhatnagar, E. P. Gross and M. Krook. A model for collision processes in gases. I. Small amplitude processes in charged and neutral one-component

systems. *Physical Review*, 94(3):511–525, 1954. ISSN 0031899X. doi:10.1103/PhysRev.94.511.

[87] P. D. Nicolaï, J. L. A. Feugeas and G. P. Schurtz. A practical nonlocal model for heat transport in magnetized laser plasmas. *Physics of Plasmas*, 13(3):1–14, 2006. ISSN 1070664X. doi:10.1063/1.2179392.

[88] B. Dubroca, J. L. Feugeas and M. Frank. Angular moment model for the Fokker-Planck equation. *European Physical Journal D*, 60(2):301–307, 2010. ISSN 14346060. doi:10.1140/epjd/e2010-00190-8.

[89] M. Touati, J. L. Feugeas, P. Nicolaï, J. J. Santos, L. Gremillet and V. T. Tikhonchuk. A reduced model for relativistic electron beam transport in solids and dense plasmas. *New Journal of Physics*, 16:073014, 2014. ISSN 13672630. doi:10.1088/1367-2630/16/7/073014.

[90] D. Del Sorbo, J. L. Feugeas, P. Nicolaï, M. Olazabal-Loumé, B. Dubroca, S. Guisset, M. Touati and V. Tikhonchuk. Reduced entropic model for studies of multidimensional nonlocal transport in high-energy-density plasmas. *Physics of Plasmas*, 22(8):082706, 2015. ISSN 10897674. doi:10.1063/1.4926824.

[91] D. Del Sorbo, J.-L. Feugeas, P. Nicolaï, M. Olazabal-Loumé, B. Dubroca and V. Tikhonchuk. Extension of a reduced entropic model of electron transport to magnetized nonlocal regimes of high-energy-density plasmas. *Laser and Particle Beams*, 34(03):412–425, 2016. ISSN 0263-0346. doi:10.1017/S0263034616000252.

[92] V. N. Goncharov, O. V. Gotchev, E. Vianello, T. R. Boehly, J. P. Knauer, P. W. McKenty, P. B. Radha, S. P. Regan, T. C. Sangster, S. Skupsky, V. A. Smalyuk, R. Betti, R. L. McCrory, D. D. Meyerhofer and C. Cherfils-Clérouin. Early stage of implosion in inertial confinement fusion: Shock timing and perturbation evolution. *Physics of Plasmas*, 13(1):1–28, 2006. ISSN 1070664X. doi:10.1063/1.2162803.

[93] W. Manheimer, D. Colombant and V. Goncharov. The development of a Krook model for nonlocal transport in laser produced plasmas. I. Basic theory. *Physics of Plasmas*, 15(8):1–10, 2008. ISSN 1070664X. doi:10.1063/1.2963078.

[94] W. Manheimer, D. Colombant and A. J. Schmitt. Calculations of nonlocal electron energy transport in laser produced plasmas in one and two dimensions using the velocity dependent Krook model. *Physics of Plasmas*, 19(5):1–14, 2012. ISSN 1070664X. doi:10.1063/1.4718458.

[95] A. V. Brantov, V. Y. Bychenkov and W. Rozmus. Nonstationary kinetic theory of ion transport in plasma with small perturbations. *Plasma Physics Reports*, 39(5):364–373, 2013. ISSN 1063-780X. doi:10.1134/S1063780X13050012.

[96] Z. Zheng, W. Rozmus, V. Y. Bychenkov, A. V. Brantov and C. E. Capjack. Nonlocal transport model in equilibrium two-component plasmas. *Physics of Plasmas*, 16(10):1–18, 2009. ISSN 1070664X. doi:10.1063/1.3234240.

[97] G. Pomraning. *Equations of Radiation Hydrodynamics*. Pergamon Press, 1973.

[98] J. Castor. *Radiation hydrodynamics*. Cambridge University Press, New York, 2004. ISBN 0511231334.

[99] K. Eidmann, R. F. Schmalz and R. Sigel. Conversion of laser light into soft x rays. Part I: Dimensional analysis. *Physics of Fluids B: Plasma Physics*, 2(1):199, 1990. ISSN 08998221. doi:10.1063/1.859528.

[100] J. Sanz, R. Betti, V. A. Smalyuk, M. Olazabal-Loume, V. Drean, V. Tikhonchuk, X. Ribeyre and J. Feugeas. Radiation hydrodynamic theory of double ablation fronts in direct-drive inertial confinement fusion. *Physics of Plasmas*, 16(8), 2009. ISSN 1070664X. doi:10.1063/1.3202697.

[101] V. Drean, M. Olazabal-Loumé, J. Sanz and V. T. Tikhonchuk. Dynamics and stability of radiation-driven double ablation front structures. *Physics of Plasmas*, 17(12):122701, 2010. ISSN 1070-664X. doi:10.1063/1.3509108.

[102] J. C. Ragusa, J. L. Guermond and G. Kanschat. A robust S N-DG-approximation for radiation transport in optically thick and diffusive regimes. *Journal of Computational Physics*, 231(4):1947–1962, 2012. ISSN 00219991. doi:10.1016/j.jcp.2011.11.017.

[103] G. Tsakiris and K. Eidmann. An approximate method for calculating Planck and Rosseland mean opacities in hot, dense plasmas. *Journal of Quantitative Spectroscopy and Radiative Transfer*, 38(5):353–368, 1987. ISSN 00224073. doi:10.1016/0022-4073(87)90030-6.

[104] H. K. Chung, M. H. Chen, W. L. Morgan, Y. Ralchenko and R. W. Lee. FLYCHK: Generalized population kinetics and spectral model for rapid spectroscopic analysis for all elements. *High Energy Density Physics*, 1(1):3–12, 2005. ISSN 15741818. doi:10.1016/j.hedp.2005.07.001.

[105] P. Hakel, M. E. Sherrill, S. Mazevet, J. Abdallah, J. Colgan, D. P. Kilcrease, N. H. Magee, C. J. Fontes and H. L. Zhang. The new Los Alamos opacity code ATOMIC. *Journal of Quantitative Spectroscopy and Radiative Transfer*, 99(1-3):265–271, 2006. ISSN 00224073. doi:10.1016/j.jqsrt.2005.04.007.

[106] Z. Chen, G. Huan and Y. Ma. *Computational Methods for Multiphase Flows in Porous Media*. Society for Industrial and Applied Mathematics Philadelphia, 2006. ISBN 0898716063.

[107] C. Johnson. *Numerical Solutions of Partial Differential Equations by the Finite Element Method*. Cambridge University Press, Cambridge, 1994.

[108] W. H. Reed and T. R. Hill. Triangular mesh methods for the neutron transport equation. Technical Report LA-UR-73-479, Los Alamos Scientific Laboratory, Los Alamos, 1973.

[109] P. Lesaint and P. A. Raviart. On a finite element method for solving the neutron transport equation. *Mathematical aspects of finite elements in partial differential equations*, 33:89–123, 1974.

[110] Y. Wang and J. C. Ragusa. A high-order discontinuous Galerkin method for the SN transport equations on 2D unstructured triangular meshes. *Annals of Nuclear Energy*, 36(7):931–939, 2009. ISSN 03064549. doi:10.1016/j.anucene.2009.03.002.

[111] MFEM: Modular finite element methods. URL `<http://mfem.org>`, accesed April 2017.

[112] P. G. Dykema, R. I. Klein and J. I. Castor. A New Scheme for Multidimensional Line Transfer. III. A Two-dimensional Lagrangian Variable Tensor Method with Discontinuous Finite-Element SN Transport. *The Astrophysical Journal*, 457:892, 1996. ISSN 0004-637X. doi:10.1086/176784.

[113] M. Holec, M. Cotelo, P. Velarde and R. Liska. Application of Discontinuous Galerkin adaptive mesh and order refinement method to energy transport and conservation equation in radiation-hydrodynamics. In S. Idelsohn, V. Sonzogni, A. Coutinho, M. Cruchaga, A. Lew, M. Cerrolaza, editor, *1st Pan American Congress on Computational Mechanics, Buenos Aires*, pages 919–930. CIMNE, Barcelona, 2015.

[114] M. Holec, J. Limpouch, R. Liska and S. Weber. High-order discontinuous Galerkin nonlocal transport and energy equations scheme for radiation hydrodynamics. *International Journal for Numerical Methods in Fluids*, 83(10):779–797, 2017. doi:10.1002/fld.4288.

[115] R. Yang and G. Yuan. h-Refinement for simple corner balance scheme of SN transport equation on distorted meshes. *Journal of Quantitative Spectroscopy and Radiative Transfer*, 184:241–253, 2016. ISSN 00224073. doi:10.1016/j.jqsrt.2016.07.020.

[116] C. Johnson and J. Saranen. Streamline Diffusion Methods for the Incompressible Euler and Navier-Stokes Equations. *Mathematics of Computation*, 47(175):1, 1986. ISSN 00255718. doi:10.2307/2008079.

[117] M. Fajardo, P. Audebert, P. Renaudin, H. Yashiro, R. Shepherd, J. C. Gauthier and C. Chenais-Popovics. Study of the ion-distribution dynamics of an aluminum laser-produced plasma with picosecond resolution. *Physical Review Letters*, 86(7):1231–1234, 2001. ISSN 00319007. doi:10.1103/PhysRevLett.86.1231.

[118] R. Ramis, R. Schmalz and J. Meyer-ter-Vehn. MULTI - A computer code for one-dimensional multigroup radiation hydrodynamics. *Computer Physics Communications*, 49:475–505, 1988.

[119] D. Shvarts, C. Jablon, I. Bernstein, J. Virmont and P. Mora. A dual treatment of suprathermal electron transport in laser fusion studies. *Nuclear Fusion*, 19(11):1457–1472, 1979. ISSN 0029-5515. doi:10.1088/0029-5515/19/11/006.

[120] P. M. Knupp. Winslow smoothing on two-dimensional unstructured meshes. *Engineering with Computers*, 15(3):263–268, 1999. ISSN 01770667. doi:10.1007/s003660050021.

[121] A. M. Winslow. Numerical Solution of the Quasilinear Poisson Equation in a Nonuniform Triangle Mesh. *Journal of Computational Physics*, 135(2):128–138, 1997. ISSN 00219991. doi:10.1006/jcph.1997.5698.

[122] P. Hoch. An Arbitrary Lagrangian-Eulerian strategy to solve compressible fluid flows, 2009. HAL: hal–00366858.